

Spring 2004

Multiple steady solutions and bifurcations in the symmetric driven cavity

Kahar Bin Osman

University of New Hampshire, Durham

Follow this and additional works at: <https://scholars.unh.edu/dissertation>

Recommended Citation

Osman, Kahar Bin, "Multiple steady solutions and bifurcations in the symmetric driven cavity" (2004). *Doctoral Dissertations*. 213.
<https://scholars.unh.edu/dissertation/213>

This Dissertation is brought to you for free and open access by the Student Scholarship at University of New Hampshire Scholars' Repository. It has been accepted for inclusion in Doctoral Dissertations by an authorized administrator of University of New Hampshire Scholars' Repository. For more information, please contact nicole.hentz@unh.edu.

**MULTIPLE STEADY SOLUTIONS AND
BIFURCATIONS IN THE SYMMETRIC DRIVEN
CAVITY**

BY

Kahar Bin Osman

B.Sc., University of Hartford, CT (1989)
M.Sc., University of Leeds, UK (1995)

DISSERTATION

Submitted to the University of New Hampshire
in partial fulfillment of
the requirements for the degree of

Doctor of Philosophy
in
Engineering, Mechanical

May 2004

UMI Number: 3132794

INFORMATION TO USERS

The quality of this reproduction is dependent upon the quality of the copy submitted. Broken or indistinct print, colored or poor quality illustrations and photographs, print bleed-through, substandard margins, and improper alignment can adversely affect reproduction.

In the unlikely event that the author did not send a complete manuscript and there are missing pages, these will be noted. Also, if unauthorized copyright material had to be removed, a note will indicate the deletion.

UMI[®]

UMI Microform 3132794

Copyright 2004 by ProQuest Information and Learning Company.

All rights reserved. This microform edition is protected against unauthorized copying under Title 17, United States Code.

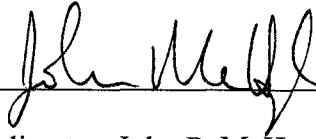
ProQuest Information and Learning Company
300 North Zeeb Road
P.O. Box 1346
Ann Arbor, MI 48106-1346

ALL RIGHTS RESERVED

©2004

Kahar Bin Osman

This dissertation has been examined and approved.



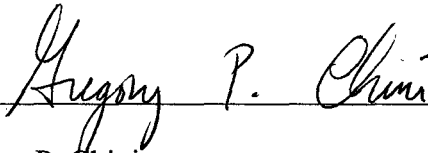
Dissertation director, John P. McHugh

Associate Professor of Mechanical Engineering Department



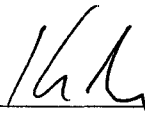
David W. Watt

Professor of Mechanical Engineering Department



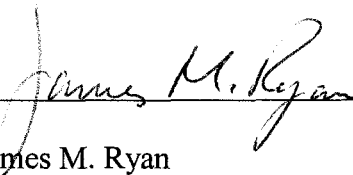
Gregory P. Chini

Assistant Professor of Mechanical Engineering Department



Kelly Black

Associate Professor of Mathematics Department



James M. Ryan

Professor of Physics Department

1/9/04

Date

DEDICATION

Dengan namaNya yang Maha Pengasih dan Penyayang. KepadaMu ku panjatkan kesyukuran di atas segala rahmat yang telah aku terima.

Kepada ibuku yang telah mendidik ku dan mengajar aku untuk menjadi seorang manusia yang sempurna dan membawa aku ke tahap ini.

Kepada isteriku yang telah banyak berkorban masa, tenaga dan memberi aku sokongan moral sepanjang aku melalui saat-saat sukar untuk menyempurnakan pengajian ini.

Kepada anak-anakku yang telah bersabar di sepanjang ketiadaanku semasa aku pengajian ini berjalan.

Kepada adik beradikku, ayah dan ibu mertuaku, ipar duai yang telah banyak memberi sokongan moral kepada ku dan membantu keluarga ku.

Kepada rakan-rakan John, Oliver, Enamur, Mah, Tracey, Abu Hassan, kakitangan UTM amnya, dan semua mereka yang telah membantuku menyempurnakan pengajian ini.

ACKNOWLEDGEMENTS

I would like to thank my supervisor, Professor John McHugh, for his support, assistance, motivation and dedication throughout this study. I could not thank him enough for all his effort.

I would like to thank all the committee members for the defense: Professor David Watt, Professor Kelly Black, Professor Greg Chini and Professor James Ryan. All knowledge that was rendered had made this thesis come to its end.

I would like to thank Chantal Pic for the support in the software VU.

I would like to thank all my colleagues in UTM for their technical and moral support, particularly to Dr. Abu Hassan for teaching me a lot about linux and its peripheral.

TABLE OF CONTENTS

Dedication	iv
Acknowledgments	v
Abstract	xiv
1 Introduction	1
1.1 Motivation	4
2 Mathematical preliminaries	8
2.1 Navier-Stokes equation	8
2.2 Numerical solution techniques	10
2.2.1 Temporal integration and splitting	10
2.2.2 High order pressure boundary conditions	13
2.2.3 Spatial discretization and other details	14
3 Validation	17
3.1 Two dimensional case	17
3.2 Three dimensional case	19
4 Two-Dimensional Results	26
4.1 Parameters	26
4.2 Boundary conditions	27
4.3 Initial conditions	27
4.4 Traditional driven cavity	28
4.5 Results with a square cavity	31
4.5.1 $n = 1$	31

4.5.2	$n = 2$	31
4.5.3	$n = 4$	32
4.5.4	$n = 6$	34
4.5.5	$n = 8$	35
4.6	Results with a rectangular cavity	35
4.6.1	$n = 2$	35
4.6.2	$n = 4$	36
4.6.3	$n = 6$	37
4.6.4	$n = 8$	38
4.7	Higher forcing mode numbers	38
4.8	Discussion	39
5	Three-dimensional results	62
5.1	Preliminaries	62
5.2	Results with symmetric unidirectional forcing	63
5.3	Results with bidirectional forcing	65
6	Conclusions	96
6.1	Discussion	96
6.2	Specific conclusions	97

LIST OF TABLES

3.1	Location of primary vortex	19
4.1	Location of primary vortex	30
4.2	Range of R_e for asymmetric solution at higher forcing functions	39

LIST OF FIGURES

1-1	Schematic of streamlines with symmetric forcing function showing (a) steady symmetric and (b) steady asymmetric flow	2
1-2	Schematic for the case where $m = 2$ and $n = 4$. The aspect ratio is $\frac{1}{2}$	3
1-3	Schematic of non-uniform forcing that could occur at a lake surface.	6
1-4	Schematic of papermaking machinery showing presence of vortices to enhance mixing of the pulp.	6
1-5	Summary of cases for two-dimensional simulations	7
2-1	Comparison between two different boundary conditions for the standard driven cavity problem, $Re = 1.0$	16
2-2	Marching row by row with SOR by lines for the two-dimensional case	16
3-1	2D case: Horizontal and vertical velocity profiles for $Re = 100$	20
3-2	2D case: Horizontal and vertical velocity profiles for $Re = 1000$	21
3-3	Extrema of horizontal and vertical velocities for $Re = 1000$	22
3-4	The three dimensional driven cavity	23
3-5	3D case: Horizontal and vertical velocity profiles along vertical and horizontal centerlines, respectively, for $Re = 100$	24
3-6	3D case: Horizontal and vertical velocity profiles along vertical and horizontal centerlines, respectively, for $Re = 400$	25
4-1	Schematic of the various combinations of forcing and initial flow	41
4-2	Streamlines for the traditional driven cavity with $\gamma = 1$	42
4-3	Streamlines for the traditional driven cavity with $\gamma = \frac{1}{2}$	43

4-4	Results with $\gamma = 1$ and $n = 2$: (a) locus of values for \underline{u} for steady flow, (b) time histories of \underline{u} for different R_e for unsteady flow, (c) streamlines for the unsteady flow, $R_e = 3700$, and (d) streamlines for the unsteady flow, $R_e = 4500$	44
4-5	Results with $\gamma = 1$ and $n = 4$: (a) streamlines for the steady symmetric solution, $R_e = 600$, (b) streamlines for the steady asymmetric solution, $R_e = 700$, and (c) streamlines for the unsteady flow, $R_e = 3000$	45
4-6	Results with $\gamma = 1$ and $n = 4$. (a) locus of values \underline{u} for steady flow, (b) time histories of \underline{u} , (c) time histories of \underline{u} for $R_e = 1000$ starting with different vortex magnitudes, $m = 1$, and (d) time histories of \underline{u} for $R_e = 1500$ with different initial mode number	46
4-7	Results with $\gamma = 1$ and $n = 6$: (a) streamlines for the symmetric solution, $R_e = 400$, (b) streamlines for the asymmetric solution, $R_e = 500$, (c) streamlines for the asymmetric solution, $R_e = 900$, and (d) streamlines for the unsteady flow, $R_e = 1000$	47
4-8	Results with $\gamma = 1$ and $n = 6$: (a) loci of values of \underline{u} for steady flow (b) time histories of \underline{u} for different R_e and $m = 1$	48
4-9	Results with $\gamma = 1$ and $n = 8$ (a) streamlines for the symmetric solution, $R_e = 400$, (b) streamlines for the asymmetric solution, $R_e = 600$, (c) streamlines for the asymmetric solution, $R_e = 1150$, and (d) streamlines for the unsteady flow, $R_e = 1500$	49
4-10	Results with $\gamma = 1$ and $n = 8$: (a) loci of values for \underline{u} for steady solution, (b) time histories of \underline{u} for different R_e , $m = 1$, and (c) time histories of \underline{u} for various initial conditions, $R_e = 1000$	50
4-11	Results with $\gamma = \frac{1}{2}$ and $n = 2$: (a) loci of values of \underline{u} for steady flow, (b) time histories of \underline{u} for several R_e showing a symmetric, an asymmetric and an unsteady case, and (c) time histories of \underline{u} starting from rest near critical R_e	51

unsteady flow, $Re = 9900$	52
4-13 Results with $\gamma = \frac{1}{2}$ and $n = 4$: (a) loci of values of \underline{u} for steady flow, (b) time histories of \underline{u} for different Re , $m = 1$, and (c)-(d) time histories of \underline{u} near critical Re	53
4-14 Results with $\gamma = \frac{1}{2}$ and $n = 4$: (a) streamlines for the symmetric solution, $Re = 2400$, (b) streamlines for the asymmetric solution, $Re = 2750$, (c) streamlines for the asymmetric solution, $Re = 4200$, (d) streamlines for the unsteady flow, $Re = 2800$, and (e) streamlines for the unsteady flow, $Re = 4300$	54
4-15 Results with $\gamma = \frac{1}{2}$ and $n = 6$: (a) loci of values of \underline{u} for steady solutions, (b) time histories of \underline{u} for different Re , $m = 1$, and (c) time histories of \underline{u} with different initial mode number, $Re = 3000$	55
4-16 Results with $\gamma = \frac{1}{2}$ and $n = 6$: (a) streamlines for the symmetric solution, $Re = 1800$, (b) streamlines for the asymmetric solution, $Re = 3000$, (c) streamlines for the asymmetric solution, $Re = 7000$, and (d) streamlines for the unsteady flow, $Re = 8500$	56
4-17 Results with $\gamma = \frac{1}{2}$ and $n = 8$: (a) time histories of \underline{u} near critical Re , $m = 1$, (b) streamlines for the symmetric solution, $Re = 700$, and (c) streamlines for the unsteady flow, $Re = 750$	57
4-18 Loci of values of \underline{u} for steady solutions for higher forcing modes: line a - $n = 16$, line b - $n = 32$ and line c - $n = 64$	58
4-19 Results with $\gamma = 1$ and $n = 16$: (a) streamlines for the symmetric solution, $Re = 700$, and (b) streamlines for the asymmetric solution, $Re = 1000$	59
4-20 Results with $\gamma = 1$ and $n = 32$: (a) streamlines for the symmetric solution, $Re = 2700$, and (b) streamlines for the asymmetric solution, $Re = 2800$	59

4-21	Results with $\gamma = 1$ and $n = 64$: (a) streamlines for the symmetric solution, $Re = 6700$, and (b) streamlines for the asymmetric solution, $Re = 8000$. . .	60
4-22	Results with $\gamma = \frac{1}{2}$ and $n = 16$: (a) streamlines for the symmetric solution, $Re = 575$, and (b) streamlines for the asymmetric solution, $Re = 800$	60
4-23	Results with $\gamma = \frac{1}{2}$ and $n = 32$: (a) streamlines for the symmetric solution, $Re = 1400$, and (b) streamlines for the asymmetric solution, $Re = 1500$. . .	61
4-24	Results with $\gamma = \frac{1}{2}$ and $n = 64$: (a) streamlines for the symmetric solution, $Re = 4000$, and (b) streamlines for the asymmetric solution, $Re = 6000$. . .	61
5-1	(a) Symmetric forcing function (b) Bidirectional forcing function	66
5-2	(a) and (b) Initial conditions for 3D case	67
5-3	Horizontal velocity contour u for symmetric forcing, $Re = 2$	68
5-4	Horizontal velocity contour u for symmetric forcing, $Re = 2$	69
5-5	Vertical velocity contour v for symmetric forcing, $Re = 2$	70
5-6	Vertical velocity contour v for symmetric forcing, $Re = 2$	71
5-7	Transverse velocity contour w for symmetric forcing, $Re = 2$	72
5-8	Transverse velocity contour w for symmetric forcing, $Re = 2$	73
5-9	Horizontal velocity contour u for symmetric forcing, $Re = 100$	74
5-10	Horizontal velocity contour u for symmetric forcing, $Re = 100$	75
5-11	Vertical velocity contour v for symmetric forcing, $Re = 100$	76
5-12	Vertical velocity contour v for symmetric forcing, $Re = 100$	77
5-13	Transverse velocity contour w for symmetric forcing, $Re = 100$	78
5-14	Transverse velocity contour w for symmetric forcing, $Re = 100$	79
5-15	Horizontal velocity contour u for symmetric forcing, $Re = 1000$	80
5-16	Horizontal velocity contour u for symmetric forcing, $Re = 1000$	81
5-17	Vertical velocity contour v for symmetric forcing, $Re = 1000$	82
5-18	Vertical velocity contour v for symmetric forcing, $Re = 1000$	83
5-19	Transverse velocity contour w for symmetric forcing, $Re = 1000$	84
5-20	Transverse velocity contour w for symmetric forcing, $Re = 1000$	85

5-21	3D symmetric forcing function (a) Steady state solution (b) Time history of \underline{u} for various initial conditions, $Re = 100$	86
5-22	Horizontal velocity contour u for bi-directional forcing function, $Re = 10$. . .	87
5-23	Vertical velocity contour v for bi-directional forcing function, $Re = 10$. . .	88
5-24	Transverse velocity contour w for bi-directional forcing function, $Re = 10$. . .	89
5-25	Horizontal velocity contour u for bi-directional forcing function, $Re = 100$. . .	90
5-26	Vertical velocity contour v for bi-directional forcing function, $Re = 100$. . .	91
5-27	Transverse velocity contour w for bi-directional forcing function, $Re = 100$. . .	92
5-28	Horizontal velocity contour u for bi-directional forcing function, $Re = 1000$. . .	93
5-29	Vertical velocity contour v for bi-directional forcing function, $Re = 1000$. . .	94
5-30	Transverse velocity contour w for bi-directional forcing function, $Re = 1000$. . .	95

ABSTRACT
MULTIPLE STEADY SOLUTIONS AND BIFURCATIONS IN THE
SYMMETRIC DRIVEN CAVITY

by

Kahar Bin Osman
University of New Hampshire, May, 2004

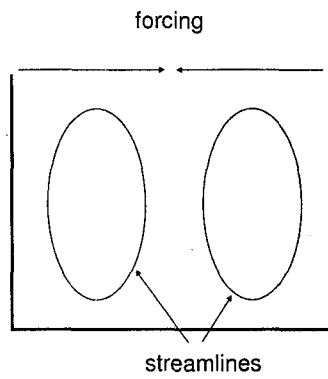
The symmetric driven cavity with sinusoidal forcing for two- and three-dimensions is considered. Results are obtained via numerical computations of the Navier Stokes equations with constant density. The numerical integration is a splitting method, using the Crank-Nicholson method for linear terms and the second-order Adams-Bashforth method for the non-linear terms. Spatial derivatives are evaluated with finite differences, and matrix equations are treated with SOR by lines. The results show symmetric solutions for low Reynolds numbers and asymmetric solutions for higher Reynolds numbers. Subcritical bifurcations are observed for two-dimensional flow. Unsteady flow behavior occurs at higher Reynolds number. Three-dimensional simulations for a cube show only one steady solution.

Chapter 1

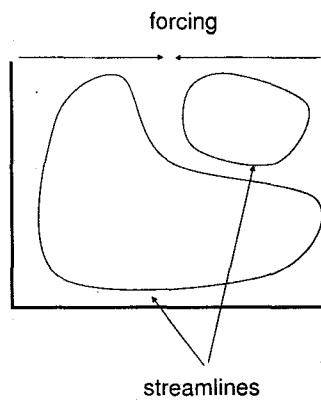
Introduction

The standard driven cavity problem is two dimensional flow in a rectangular geometry with a constant tangential velocity at the top of the cavity. This standard driven cavity problem has been treated many times [3] [7], and is often used as a benchmark for computer programs. The symmetric driven cavity is a recent variant of the driven cavity, see Farias and McHugh [4]. The symmetric driven cavity problem is also a flow in a rectangular geometry with an imposed velocity at the top, but the forcing is symmetric, resulting in zero average velocity across the top. Farias and McHugh [4] treated perhaps the simplest version of the symmetric driven cavity: sinusoidal forcing with only one period across the top, a two-dimensional square cavity, and a single vortex of variable magnitude for initial conditions.

The results of Farias and McHugh [4] show that a symmetric steady flow, shown schematically in figure 1.1(a), is the result for low Reynolds numbers and weak disturbances. However, they also found a second steady solution that had not been previously recognized. This second solution is asymmetric with respect to the vertical centerline of the cavity, despite the symmetry of the boundary conditions, and is shown schematically in figure 1.1(b). The second solution is achieved by initiating the flow with a single vortex of chosen magnitude.



(a)



(b)

Figure 1-1: Schematic of streamlines with symmetric forcing function showing (a) steady symmetric and (b) steady asymmetric flow

The symmetric driven cavity is extended here to include sinusoidal forcing with more than one oscillation across the top boundary, and initial conditions with more complexity. The forcing is chosen to be zero at the corners of the cavity, and is given by $u(x) = \sin(n\pi x)$, where $0 \leq x \leq 1$, and the integer n is the forcing mode number. The initial conditions consist of a number of vortices across the chamber (Farias and McHugh used only one), which will be indicated by the integer, m , the initial condition mode number. Each case is then characterized by the mode number pair, (m, n) . For example, the $(2,4)$ case would have two initial vortices and four complete oscillations in the forcing across the top. This example is shown schematically in 1.2. Note that the aspect ratio of the chamber, which is a free parameter, is $\frac{1}{2}$ for the case shown in figure 1.2.

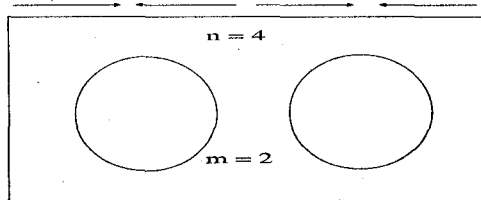


Figure 1-2: Schematic for the case where $m = 2$ and $n = 4$. The aspect ratio is $\frac{1}{2}$.

Two and three dimensional problems are considered. For the two-dimensional problem, the cases that are considered in detail are shown graphically in figure 1-5. The three dimensional results, which are of course much more demanding of computer resources, are limited to a few cases.

The results are obtained by direct numerical simulation of the incompressible Navier-Stokes equations. The numerical method is a finite difference method. Temporal integration is achieved with a time-splitting method, similar to the method of Karniadakis et al. [1].

Validation of the computer program is achieved primarily via comparison with existing numerical results on the standard driven cavity and the symmetric driven cavity.

The two-dimensional simulations show that the overlap region where two steady solutions could exist disappears for some cases, and no cases have been found when there are three or more steady solutions for the same Reynolds number.

The three-dimensional simulations show weakly asymmetric behavior for very low Reynolds number with increasing symmetry as R_e increases. There are no three-dimensional cases showing more than one steady solution for the same R_e .

1.1 Motivation

The symmetric driven cavity considered here is motivated by a variety of geophysical and industrial flows. Two examples will be given: 1) flow in a confined body such as a lake, and 2) flow in a papermaking machine.

The first example is water in a confined body, such as a lake or pond. Wind blowing over the surface of the water results in motion of the water throughout the lake. The motion of the water is responsible for a variety of patterns in the lake, as well as concentrations of biological nutrients and associated biological activities. These patterns are important to all environmental aspects of the lake.

The wind at a lake surface is not uniform. A two-dimensional example is shown schematically in figure 1.3. Local topographical features and nearby trees can have a significant effect on the average wind speed, even resulting in air flow in direction opposite the prevailing wind, as shown in figure 1.3. This flow reversal of the air would force a flow reversal at the surface of the lake, thereby perhaps influencing the flow throughout the lake. Flow patterns in lakes do show local concentrations of biological constituents, which could be related to the flow pattern on the surface, and thereby surrounding topography. However, this relationship between surface forcing and flow pattern is not completely understood, and in fact can be misleading, as will be shown here. Attempts to control the lake flow with drastic changes in the surrounding features appear to be unnecessary.

The second example is an industrial flow concerning the manufacturing of papermaking. Paper is made in large quantities using high speed machinery. The process begins by forming pulp, which is generally 95 percent water and 5 percent wood fiber. The pulp flows through a slot and onto a screen where the water is drained. The remaining wood fibers are then pressed and dried. A schematic is shown in figure 1.4. The most important feature for making quality paper is to retain adequate mixing in the pulp as the water drains so that the fibers will be randomly oriented in the final paper. The mixing is commonly achieved inside the slot with troublesome and expensive turbulence generators.

A recent attempt to improve mixing during the draining process used coherent stream-wise vortices induced at the slot. The vortices were expected to reach further from the slot than turbulence, and therefore enhance mixing during the later stages of draining. This initial attempt showed that the coherent vortices can lead to streaks in the final paper, ruining the process. However, the choice of the pattern of the vortices was not based on practical aspect of the vortex generation. It is shown here that the pattern of vortices is critical to achieve vortices that will enhance mixing, rather than supressing it.

Beyond these two specific examples, the results of Farias and Mchugh [4] suggest a more general feature of flow in a confined region. Confined flow can be forced in variety of ways, including translation, rotation, or oscillation. Perhaps there is a universal feature, whatever the forcing. This generalization has not yet been achieved, but is supported by the work considered here.

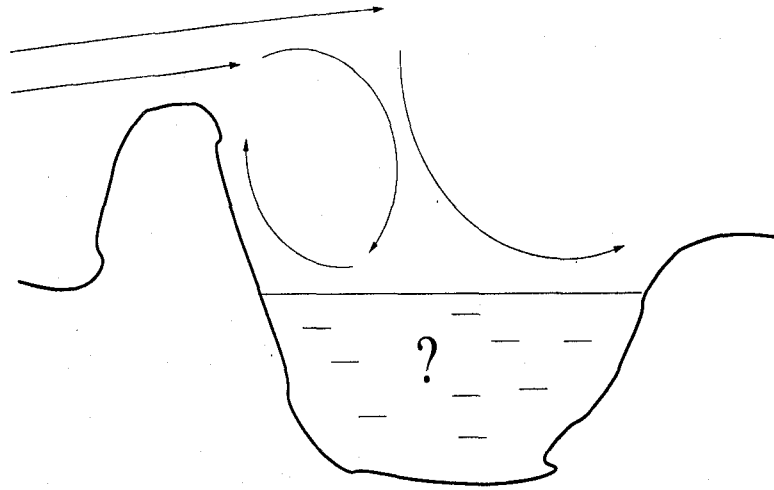


Figure 1-3: Schematic of non-uniform forcing that could occur at a lake surface.

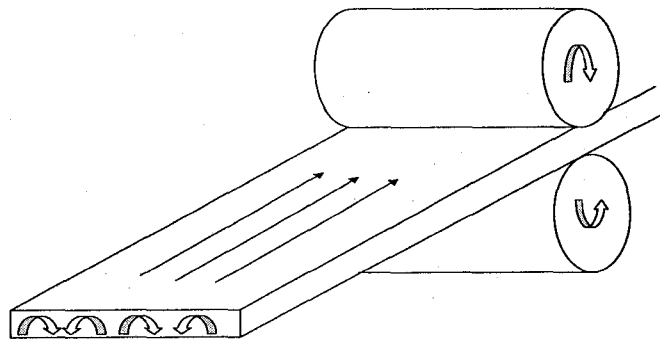
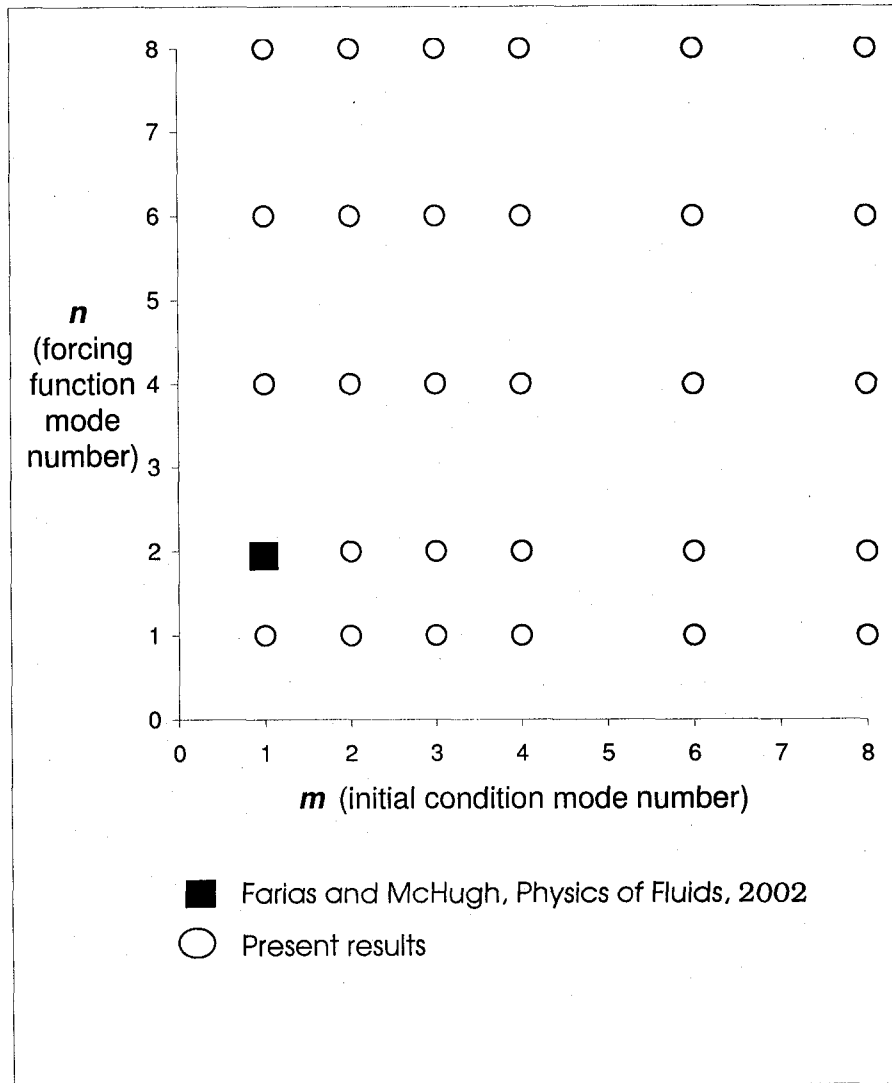


Figure 1-4: Schematic of papermaking machinery showing presence of vortices to enhance mixing of the pulp.



(a)

Figure 1-5: Summary of cases for two-dimensional simulations

Chapter 2

Mathematical preliminaries

2.1 Navier-Stokes equation

Consider a Newtonian flow with constant material properties, including constant density, governed by the Navier-Stokes and continuity equations. The Navier-Stokes equations for constant density flow, in vector form, are

$$\rho \left(\frac{\partial \vec{v}}{\partial t} + \vec{v} \cdot \nabla \vec{v} \right) = -\nabla p + \mu \nabla^2 \vec{v}, \quad (2.1)$$

where

$$\vec{v} = u\vec{i} + v\vec{j} + w\vec{k} \quad (2.2)$$

is the velocity vector, p is the pressure, μ is dynamic viscosity, ρ is fluid density, and t is time. The continuity equation for constant density is

$$\nabla \cdot \vec{v} = 0. \quad (2.3)$$

Consider three-dimensional flow in a rectangle of height, H , length, L , and depth, D . Dimensionless variables are defined as

$$\begin{aligned} \tilde{u} &= \frac{u}{U}, \\ \tilde{v} &= \frac{v}{U}, \\ \tilde{w} &= \frac{w}{U}, \\ \tilde{p} &= \frac{p}{\rho U^2}, \\ \tilde{x} &= \frac{x}{L}, \end{aligned}$$

$$\begin{aligned}\tilde{y} &= \frac{y}{H}, \\ \tilde{z} &= \frac{z}{D},\end{aligned}\tag{2.4}$$

where U is a reference velocity. For the present results, U is the amplitude of the sinusoidal velocity on the top boundary, eg. the amplitude of the forcing. Dropping the circumflex, the resulting dimensionless equations are

$$\frac{\partial \vec{v}}{\partial t} + \vec{v} \cdot \nabla \vec{v} = -\nabla p + \frac{1}{R_e} \nabla^2 \vec{v},\tag{2.5}$$

where R_e is the Reynolds Number, defined as

$$R_e = \frac{UL}{\nu},\tag{2.6}$$

and ν is the kinematic viscosity.

In component form for Cartesian coordinates, these equations are

$$\begin{aligned}\frac{\partial u}{\partial t} + u \frac{\partial u}{\partial x} + \frac{1}{\gamma} v \frac{\partial u}{\partial y} + \frac{1}{\lambda} w \frac{\partial u}{\partial z} &= -\frac{\partial p}{\partial x} + \frac{1}{R_e} \left(\frac{\partial^2 u}{\partial x^2} + \frac{1}{\gamma^2} \frac{\partial^2 u}{\partial y^2} + \frac{1}{\lambda^2} \frac{\partial^2 u}{\partial z^2} \right) \\ \frac{\partial v}{\partial t} + u \frac{\partial v}{\partial x} + \frac{1}{\gamma} v \frac{\partial v}{\partial y} + \frac{1}{\lambda} w \frac{\partial v}{\partial z} &= -\frac{\partial p}{\partial y} + \frac{1}{R_e} \left(\frac{\partial^2 v}{\partial x^2} + \frac{1}{\gamma^2} \frac{\partial^2 v}{\partial y^2} + \frac{1}{\lambda^2} \frac{\partial^2 v}{\partial z^2} \right) \\ \frac{\partial w}{\partial t} + u \frac{\partial w}{\partial x} + \frac{1}{\gamma} v \frac{\partial w}{\partial y} + \frac{1}{\lambda} w \frac{\partial w}{\partial z} &= -\frac{\partial p}{\partial z} + \frac{1}{R_e} \left(\frac{\partial^2 w}{\partial x^2} + \frac{1}{\gamma^2} \frac{\partial^2 w}{\partial y^2} + \frac{1}{\lambda^2} \frac{\partial^2 w}{\partial z^2} \right)\end{aligned}\tag{2.7}$$

with

$$\frac{\partial u}{\partial x} + \frac{1}{\gamma} \frac{\partial v}{\partial y} + \frac{1}{\lambda} \frac{\partial w}{\partial z} = 0\tag{2.8}$$

where $\gamma = \frac{H}{L}$ and $\lambda = \frac{D}{L}$.

The boundary conditions are the no-penetration condition, $\vec{v} \cdot \vec{n} = 0$, where \vec{n} is a unit vector normal to the boundary, and the no-slip condition, $\vec{v} \cdot \vec{\tau} = 0$, where $\vec{\tau}$ is a unit vector tangent to the boundary. On the sides and bottom of the cavity, this results in a zero velocity vector, $\vec{v} = \vec{0}$. On the top, the normal velocity is zero, $w = 0$. For two dimensional cases, the tangential velocity is the imposed sinusoidal velocity:

$$u(x) = \sin(n\pi x)\tag{2.9}$$

at $z = 1$, where $0 \leq x \leq 1$. In three dimensions, two components are imposed on the top of the cavity.

2.2 Numerical solution techniques

2.2.1 Temporal integration and splitting

The temporal integration of the Navier-Stokes system is achieved using a semi-implicit splitting method, similar to the method of Karniadakis et. al [1] and others. The Navier-Stokes equations can be expressed as

$$\frac{\partial \vec{v}}{\partial t} + \vec{N}(\vec{v}) = -\nabla p + \frac{1}{Re} \vec{L}(\vec{v}), \quad (2.10)$$

where \vec{L} is the linear viscous term and \vec{N} is the non-linear advective term:

$$\vec{L}(\vec{v}) = \nabla^2 \vec{v}, \quad (2.11)$$

$$\vec{N}(\vec{v}) = \vec{v} \cdot \nabla \vec{v}. \quad (2.12)$$

Now integrate over one time step, Δt :

$$\int_{t_k}^{t_{k+1}} \frac{\partial \vec{v}}{\partial t} dt + \int_{t_k}^{t_{k+1}} \vec{N}(\vec{v}) dt = - \int_{t_k}^{t_{k+1}} \nabla p dt + \int_{t_k}^{t_{k+1}} \frac{1}{Re} \vec{L}(\vec{v}) dt, \quad (2.13)$$

where k is the time step. The first term is easily evaluated without approximation,

$$\int_{t_k}^{t_{k+1}} \frac{\partial \vec{v}}{\partial t} dt = \vec{v}^{k+1} - \vec{v}^k. \quad (2.14)$$

The semi-implicit method treats linear terms implicitly for stability, and nonlinear terms explicitly for efficiency. Explicit evaluation of the nonlinear terms is achieved with the second-order Adams-Bashforth method:

$$\int_{t_k}^{t_{k+1}} \vec{N}(\vec{v}) dt = \left[\frac{3}{2} \vec{N}(\vec{v}^k) - \frac{1}{2} \vec{N}(\vec{v}^{k-1}) \right] \Delta t. \quad (2.15)$$

This explicit treatment of the nonlinear terms avoids sampling \vec{N} at the leading time step, which would result in nonlinear algebraic equations, requiring further iteration. The pressure term is treated by reversing the order of integration and differentiation, then introducing time-averaged pressure:

$$\int_{t_k}^{t_{k+1}} \nabla p dt = \nabla \left[\int_{t_k}^{t_{k+1}} p dt \right] = \nabla \bar{p}^{k+1} \Delta t. \quad (2.16)$$

Implicit treatment of the the linear viscous terms is achieved with the second-order Crank-Nicholson method:

$$\int_{t_k}^{t_{k+1}} \vec{L}(\vec{v}) dt = \frac{1}{2} \left[\nabla^2 \vec{v}^{k+1} + \nabla^2 \vec{v}^k \right] \Delta t. \quad (2.17)$$

The combined difference equation is now

$$\vec{v}^{k+1} - \vec{v}^k + \left[\frac{3}{2} \vec{N}(\vec{v}^k) - \frac{1}{2} \vec{N}(\vec{v}^{k-1}) \right] \Delta t = -\nabla \bar{p}^{k+1} \Delta t + \frac{1}{2R_e} \left[\nabla^2 \vec{v}^{k+1} + \nabla^2 \vec{v}^k \right] \Delta t. \quad (2.18)$$

In addition to (2.18), the continuity equation is imposed at the leading time step:

$$\nabla \cdot \vec{v}^{k+1} = 0. \quad (2.19)$$

Equations (2.18) could be treated directly, after a spatial approximation, except for the presence of pressure. Another equation is needed for pressure, and the only remaining equation is the continuity equation, which does not contain pressure. The approach to this difficulty is to use splitting.

Splitting means that (2.18) is integrated numerically in three stages for each time step, each stage addressing the nonlinear term, the pressure term, and the viscous term independently. Two intermediate velocity fields, $\hat{\vec{v}}$ and $\hat{\hat{\vec{v}}}$, are introduced in order to achieve this. The three stages are

$$\hat{\vec{v}} - \vec{v}^k = \left[\frac{3}{2} \vec{N}(\vec{v}^k) - \frac{1}{2} \vec{N}(\vec{v}^{k-1}) \right] \Delta t, \quad (2.20)$$

$$\hat{\hat{\vec{v}}} - \hat{\vec{v}} = -\nabla \bar{p}^{k+1} \Delta t, \quad (2.21)$$

$$\vec{v}^{k+1} - \hat{\hat{\vec{v}}} = \frac{1}{2R_e} \left[\nabla^2 \vec{v}^{k+1} + \nabla^2 \vec{v}^k \right] \Delta t. \quad (2.22)$$

Note that summing these three equations eliminates $\hat{\vec{v}}$ and $\hat{\hat{\vec{v}}}$, producing exactly the original discrete equation in (2.18), hence there is no further approximation with this aspect of splitting.

In order to process the second step, the average pressure, \bar{p} , must be determined. The pressure is not needed for the first step, and therefore \bar{p} can be determined after $\hat{\vec{v}}$. A Poisson equation for pressure is used to obtain pressure, keeping in mind that the continuity equation must still be enforced.

To obtain the Poisson's equation for pressure, take the divergence of (2.18) and use the continuity equation to obtain

$$\nabla^2 \bar{p}^{k+1} = \nabla \cdot \left(\frac{\hat{v}}{\Delta t} \right), \quad (2.23)$$

where the nonlinear terms are neglected. Karniadakis [1] has shown that the nonlinear terms do not contribute significantly to the pressure with this splitting method. The nonlinear terms can be included without affecting other stages of the method, but have not for the results given below. Note that for this splitting method, the divergence of the intermediate stages is not zero, and the divergence of the velocity field at the end of a time step is only approximately zero. Retaining the $\nabla \cdot \hat{v}$ term in (2.23) is important for correcting the error in the continuity equation at the next time step arising from the previous time step.

All variables require boundary conditions, including \bar{v}^{k+1} , \hat{v} , $\hat{\hat{v}}$, and \bar{p} . The boundary conditions on \bar{v}^{k+1} are the natural boundary conditions, which must be enforced at the final stage of the splitting method. Boundary conditions on \hat{v} and $\hat{\hat{v}}$ can be chosen to enhance the numerical aspects of the method. Past experience has shown that the first two stages of splitting are primarily inviscid components of motion, and therefore, only the normal boundary condition is enforced. Hence,

$$\hat{v} \cdot \bar{n} = \hat{\hat{v}} \cdot \bar{n} = 0 \quad (2.24)$$

on all boundaries. The final stage of splitting must meet the final boundary conditions, therefore,

$$\bar{v}^{k+1} = 0 \quad (2.25)$$

on all boundaries, except the top, where the chosen driving velocity is imposed as the tangential velocity.

The remaining boundary conditions are the pressure boundary conditions. There are no natural boundary conditions on the pressure; the value of pressure at the boundary depends on the velocity field in the neighborhood of the boundary. Pressure boundary conditions must be approximated from the governing equations. Take the normal component of (2.18)

to get

$$\begin{aligned}
\vec{n} \cdot \nabla \bar{p}^{k+1} &= \vec{n} \cdot \bar{v}^n - \vec{n} \cdot \bar{v}^{k+1} \\
&\quad - \vec{n} \cdot \left[\frac{3}{2} \vec{N}(\bar{v}^k) - \frac{1}{2} \vec{N}(\bar{v}^{k-1}) \right] \Delta t \\
&\quad + \frac{1}{2R_e} \vec{k} \cdot \left[\nabla^2 \bar{v}^{k+1} + \nabla^2 \bar{v}^k \right] \Delta t.
\end{aligned} \tag{2.26}$$

For an impermeable box, (2.26) becomes

$$\vec{n} \cdot \nabla \bar{p}^{k+1} = \vec{n} \cdot \frac{1}{2R_e} \left[\nabla^2 \bar{v}^{k+1} + \nabla^2 \bar{v}^k \right] \Delta t. \tag{2.27}$$

The viscous terms on the right-hand-side of (2.27) are generally not zero, and their evaluation is problematic, since they contain a term at the leading order. However, for large Reynolds number, they are also small, and could be neglected, leaving

$$\vec{n} \cdot \nabla \bar{p}^{k+1} = 0. \tag{2.28}$$

Karniadakis [1] recommends higher order boundary conditions for a better approximation of the viscous terms, especially for low Reynolds Number flow. One approach is to evaluate the viscous terms in the pressure boundary conditions with an explicit method, keeping everything else the same. This technique results in an instability. In general, the system is sensitive to the treatment of the viscous terms in the pressure boundary conditions.

2.2.2 High order pressure boundary conditions

A successful method for higher order pressure boundary conditions is obtained by rearranging the viscous linear terms in the pressure boundary condition, as in Karniadakis [1]. Note that the governing equation for pressure remains unchanged; only the boundary condition is affected. Also note that the nonlinear terms in the pressure boundary condition are still neglected.

Using a vector identity, the viscous terms can be expressed as

$$\nabla^2 \vec{v} = \nabla(\nabla \cdot \vec{v}) - \nabla \times (\nabla \times \vec{v}). \tag{2.29}$$

Again, take the normal component of (2.18) for the pressure boundary conditions. Evaluate the first term on the right-hand-side of the (2.29) implicitly using Crank-Nicolson, and evaluate the second term explicitly using Adams-Bashforth:

$$\begin{aligned}\vec{n} \cdot \nabla \bar{p}^{k+1} &= \vec{n} \cdot \frac{1}{2R_e} \left[\nabla(\nabla \cdot \vec{v}^{k+1}) + \nabla(\nabla \cdot \vec{v}^k) \right] \\ &\quad - \vec{n} \cdot \frac{1}{2R_e} \left[3\nabla \times (\nabla \times \vec{v}^k) - \nabla \times (\nabla \times \vec{v}^{k-1}) \right].\end{aligned}\quad (2.30)$$

The term $\nabla(\nabla \cdot \vec{v}^{k+1})$ is zero due to the continuity equation. The final form of the boundary condition is

$$\begin{aligned}\vec{n} \cdot \nabla \bar{p}^{k+1} &= \vec{n} \cdot \frac{1}{2R_e} \nabla(\nabla \cdot \vec{v}^k) \\ &\quad - \vec{n} \cdot \frac{1}{2R_e} \left[3\nabla \times (\nabla \times \vec{v}^k) - \nabla \times (\nabla \times \vec{v}^{k-1}) \right].\end{aligned}\quad (2.31)$$

As previously mentioned, the divergence of \vec{v} is only approximately zero at the end of a time step, hence $\vec{\nabla} \cdot \vec{v}^k$ is not zero and is retained. Note that the viscous terms in the governing equations are still treated as in (2.22).

Numerical experiments for Reynolds numbers as low as unity show no significant improvement with the higher order method. Figure 2-1 compares results obtained using (2.28) to those obtained using (2.31) for the traditional driven cavity. The higher-order method has little effect, therefore, for efficiency, the boundary conditions in (2.28) are used.

2.2.3 Spatial discretization and other details

The spatial operators are evaluated with second-order finite differences. For example, the two-dimensional Lapacian operator with $\gamma = 1$ is

$$\nabla^2 \vec{v}^{k+1} = \frac{1}{h^2} (\vec{v}_{i+1,j} + \vec{v}_{i-1,j} + \vec{v}_{i,j+1} + \vec{v}_{i,j-1} - 4\vec{v}_{i,j})^{k+1} \quad (2.32)$$

where h is the gridsize, assumed uniform in all directions. Boundary conditions are evaluated with second-order one-sided difference expressions.

The resulting systems of equations are solved using the successive over relaxation (SOR) method by lines [2]. SOR by lines is more efficient for the splitting method, compared to

a direct method. This is mostly due to the fact that SOR by lines eliminates the need to control the average pressure, which accounts for much of the computing time for a direct method. This feature is related to the fact that members of the null space of the discret pressure operator are automatically subtracted by the end of an iteration.

SOR by lines is performed here in the row-by-row manner, but can be performed column-by-column just as easily. The row-by-row method means that each row of gridpoints in the physical domain is treated successively. Solution values at neighboring rows are taken from a previous iteration, which reduces the matrix to a tri-diagonal form. The tridiagonal matrix is then solved efficiently using the Thomas algorithm. For example, consider SOR by lines applied to (2.22). Rearranging (2.22) yields

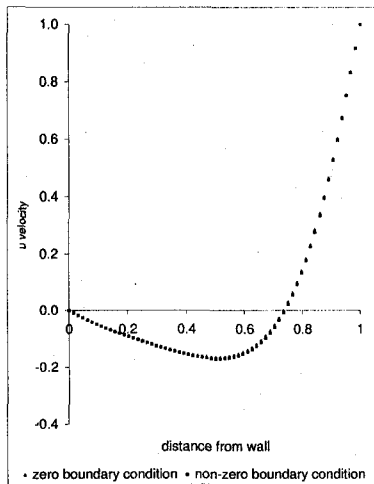
$$\bar{v}^{k+1} - \frac{\Delta t}{2R_e} \nabla^2 \bar{v}^{k+1} = \frac{\Delta t}{2R_e} \nabla^2 \bar{v}^k + \hat{\bar{v}}. \quad (2.33)$$

Employing the second order central difference discretization scheme for the second term on the left hand side of (2.33) will yield an equation for each gridpoint that has five unknowns for the two-dimensional case, or seven unknowns for the three-dimensional case. However, once values of \bar{v} from gridpoints on a different row are determined from previous iterations, there are only three unknowns. This procedure is depicted for the two-dimensional case in figure 2-2.

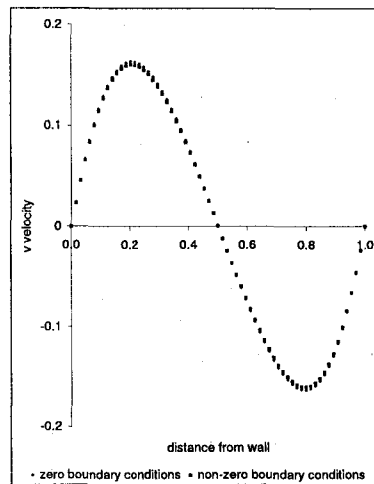
Once all the unknowns in a particular row or column are determined, the values must be 'relaxed.' Relaxation is achieved by introducing a weighting factor to improve convergence. The general form of the relaxation method used here is

$$\bar{v}^{q+1} = \bar{v}^q + \omega(\bar{v}^{q+1} - \bar{v}^q). \quad (2.34)$$

where q is the iteration index. The constant ω is the weighting factor. For this method, the weighting factor that converged the fastest was found to be 1.2. Once the values are relaxed, the next row or column can be treated successively until all the rows or columns are completed. This will end the first iteration for the entire grid. The procedure is repeated until residuals are within a specified tolerance. It is found that the required number of iterations is less than seven for all cases.



(a) u velocity



(b) v velocity

Figure 2-1: Comparison between two different boundary conditions for the standard driven cavity problem, $Re = 1.0$

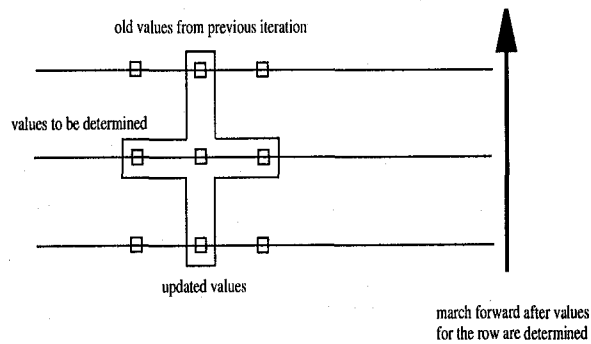


Figure 2-2: Marching row by row with SOR by lines for the two-dimensional case

Chapter 3

Validation

3.1 Two dimensional case

Validation of the algorithm and software is achieved primarily by comparison with previously published results for the traditional driven cavity. The traditional driven cavity is two-dimensional flow in a square cavity. The flow is driven at the top with a constant tangential velocity. This flow has been considered many times using many different methods. It is often a standard benchmark for computational fluid dynamics programs, as here. The results of Ghia [3] are most often used for this purpose.

The flow in the traditional driven cavity is initially at rest, and the forcing is imposed at the first time step. The flow is then allowed to reach steady state. Two methods were considered to determine the point in the simulation when the steady state is reached. One method is to track a measure of the total kinetic energy of the flow, defined as

$$Q = \sum_{i=1}^N (u^2 + v^2 + w^2), \quad (3.1)$$

where N is the total number of grid points. Computations are terminated when the change in Q falls below a chosen tolerance, usually 10^{-6} .

The other method to identify the steady state is to track the maximum velocity difference through the domain. The largest difference between u (or v and w) for the current time step is compared to the previous time step. Again, computations are terminated when the largest value falls below a chosen criterion. Tolerances between 1×10^{-6} and 1×10^{-8} are typically used, depending on the time step increment or the value of Re . In general, higher

R_e requires a smaller tolerance. This latter method is generally used for the results of this analysis. The tolerance is set to 1×10^{-7} for all velocities and pressure.

Steady results for the current simulations are directly compared to the results of Ghia [3] in figure 3-1 for a Reynolds number of 100. Figure 3-1(a) shows a profile of the horizontal velocity along the vertical center of the square, and figure 3-1(b) shows a profile of the vertical velocity along the horizontal center, for both Ghia and the current results. The resolution for the current results is 65×65 . Note that at this modest resolution, the two profiles are virtually identical. Figure 3-2 shows the same comparison for the higher Reynolds number of 1000, for the still modest resolution of 129×129 . At this Reynolds number, slight differences between the two computations can be seen at the points of maximum velocity. This difference can be made arbitrarily small by increasing resolution, by decreasing the time step, by increasing the order of the manner in which the nonlinear terms are treated, or all of the above.

Further comparison between the results of Ghia [3] and the present results are given in figure 3-3. Also included in figure 3-3 are the results of Bruneau and Jouron [7]. The figure is a comparison of the computed position of the extrema of velocities, both horizontal and vertical components. Figure 3-3 shows that the present results agree well with these previous results. Note that the position of minimum velocity is often taken to be the location of the center of the vortex that is created in the driven cavity, which is considered an important test of any numerical technique.

A final comparison is given in table 3.1, which compares the computed position of the primary vortex to Ghia's result for Reynolds numbers of 100 and 1000.

The resolution for the $R_e = 100$ case is 65×65 , while the resolution for $R_e = 1000$ case is 129×129 . In fact, for $R_e = 100$, a resolution of 33×33 is sufficient to produce accurate results. However, a resolution of 65×65 is generally used as the minimum for all calculations.

Table 3.1: Location of primary vortex

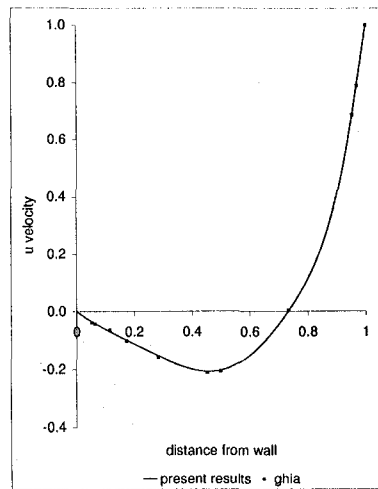
Method	Re	x	y
Ghia	100	0.6172	0.7344
	1000	0.5438	0.5625
present results	100	0.6122	0.7331
	1000	0.5411	0.5613

3.2 Three dimensional case

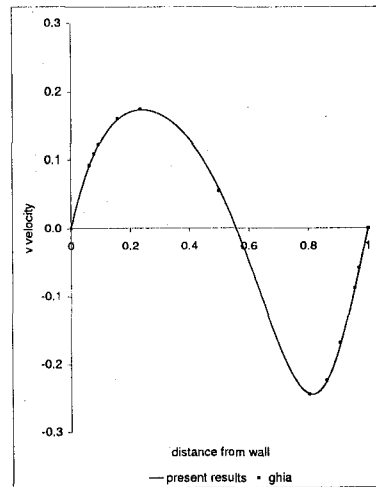
A three dimensional version of the driven cavity has been previously considered by Iwatsu, et al [6], Bravo [5], and others. The forcing was uniform at the lid, and the flow was initiated from rest. A schematic of this case is shown in figure 3.4.

The three-dimensional traditional driven cavity shown in figure 3.1 has been treated here for the purpose of validation of the three-dimensional computer program. Both aspect ratios are chosen to be unity (thus the geometry is a cube), and the Reynolds number is 100 or 400. The resolution for this simulation varies from $33 \times 33 \times 33$ to $65 \times 65 \times 65$. It is found that for low Re , $33 \times 33 \times 33$ is sufficient to obtain accurate results.

Figures 3-5 and 3-6 show several velocity profiles for the present results, and corresponding data for the previous results. Again, the agreement is excellent, demonstrating the accuracy of the computational techniques and programs.

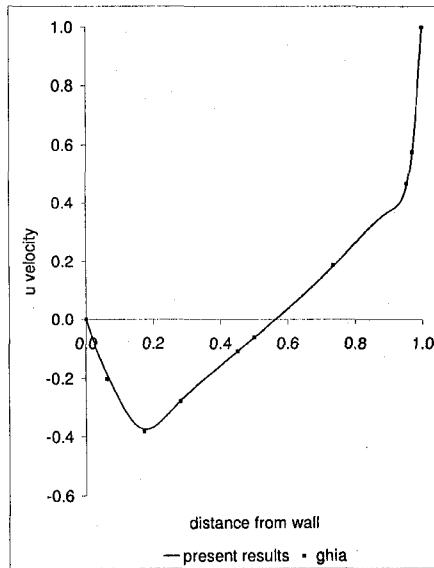


(a) u velocity

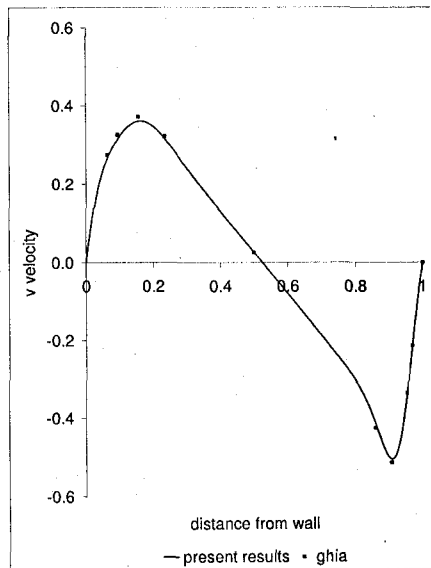


(b) v velocity

Figure 3-1: 2D case: Horizontal and vertical velocity profiles for $Re = 100$



(a) u velocity



(b) v velocity

Figure 3-2: 2D case: Horizontal and vertical velocity profiles for $Re = 1000$

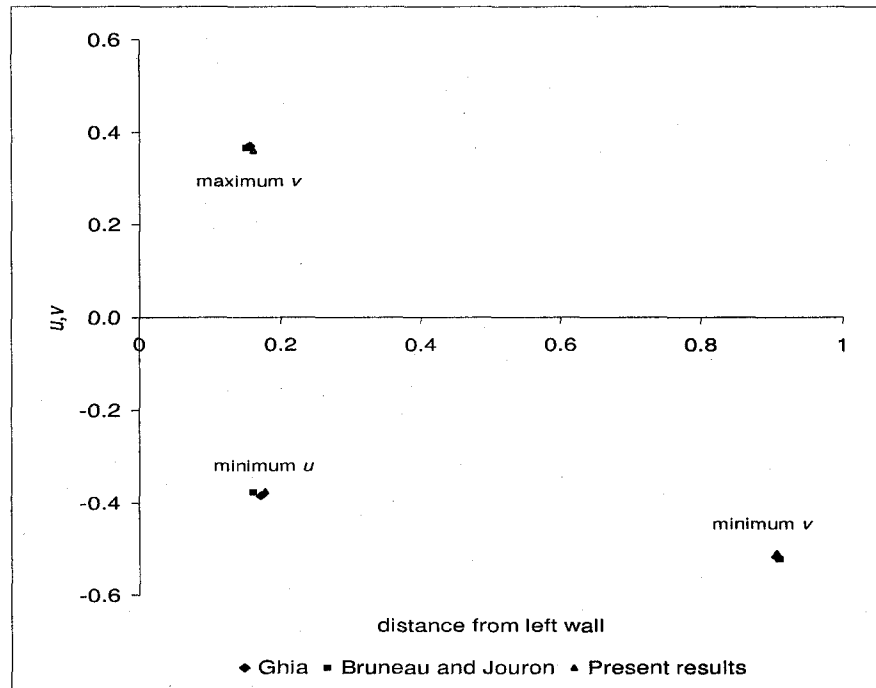


Figure 3-3: Extrema of horizontal and vertical velocities for $Re = 1000$

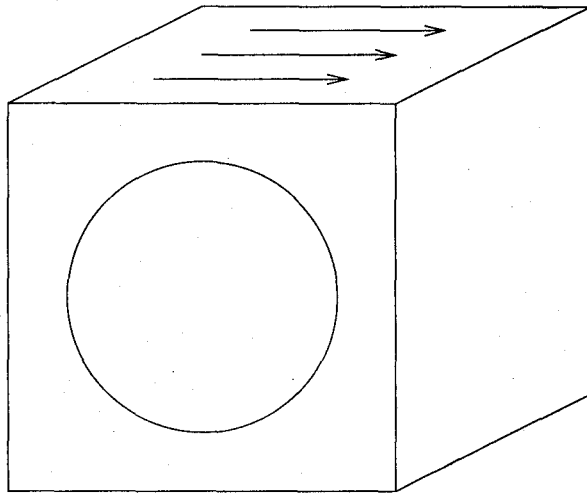
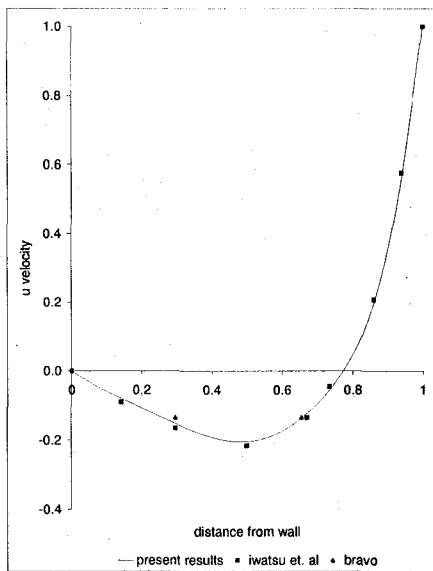
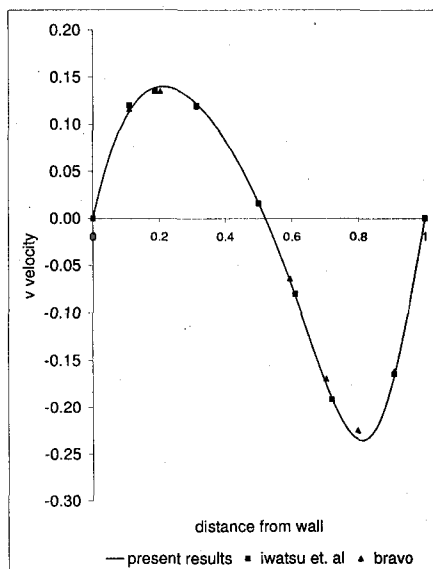


Figure 3-4: The three dimensional driven cavity

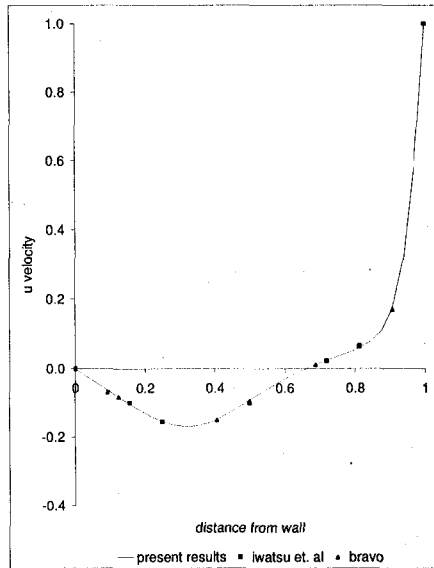


(a) u velocity

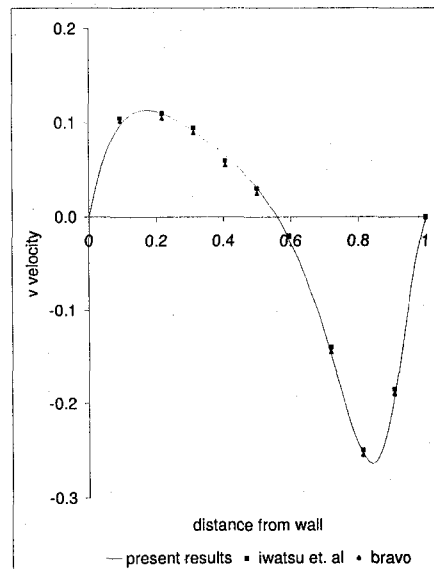


(b) v velocity

Figure 3-5: 3D case: Horizontal and vertical velocity profiles along vertical and horizontal centerlines, respectively, for $Re = 100$



(a) u velocity



(b) v velocity

Figure 3-6: 3D case: Horizontal and vertical velocity profiles along vertical and horizontal centerlines, respectively, for $Re = 400$

Chapter 4

Two-Dimensional Results

4.1 Parameters

Non-dimensionalization of the governing equations shows that there are two basic parameters for the two-dimensional case; the Reynolds number, $R_e = \frac{UL}{\nu}$, and the aspect ratio, $\gamma = \frac{H}{L}$. Only two values of the aspect ratio are treated here, 1 and $\frac{1}{2}$. The Reynolds number is the bifurcation parameter, and many values of R_e will be treated for each configuration, depending on the circumstance.

The initial conditions for the simulations play an important role in the present results. The magnitude of the initial conditions must be characterized in some manner. Symmetry of the initial conditions was found previously to be an important factor in the final state (Farias and McHugh [4]), and a symmetry parameter was used to characterize both the magnitude of the initial conditions and the final steady state. The symmetry parameter is useful here as well, and is defined to be

$$\underline{u}(t) = \int_0^1 |u| dy, \quad (4.1)$$

taken along the vertical centerline of the chamber. The integral will vanish if the flow is perfectly symmetric about the vertical centerline.

Note that \underline{u} is not an ideal indicator of symmetry and must be used with caution. For example, a symmetric initial condition of any magnitude will have a zero value of \underline{u} , hence, \underline{u} is not a useful measure for symmetric flows. Also, it is possible to have asymmetric motion that is increasing in magnitude, but has a decreasing value of \underline{u} . This was true for

the results of Farias and McHugh [4]. Despite these shortcomings, \underline{u} is the most convenient measure for this study.

4.2 Boundary conditions

The flow is forced by imposing a tangential velocity at the top of the domain. The traditional driven cavity [3] has a constant velocity across the top of the cavity, $U = 1$. The symmetric driven cavity of Farias and McHugh [4] has a sinusoidal variation across the top of the cavity with a single period of oscillation, given by $u(x) = \sin 2\pi x$ and $0 \leq x \leq 1$. The forcing profile of Farias and McHugh [4] is generalized here to include more cycles, and is now given by

$$u(x) = \sin(n\pi x), \quad (4.2)$$

where the wavenumber, n , is chosen to be a positive integer. This choice for n allows more cycles in the forcing, yet still has the feature of zero velocity at the top corners of the domain. This feature is appealing in that the no-slip condition at the sidewall results in a continuous velocity field. If the forcing is not zero at the endpoints of the top, the velocity field at the corners would be discontinuous.

Note that the average velocity due to the above forcing is

$$\int_0^1 \sin(n\pi x) dx. \quad (4.3)$$

The integral is zero when n is even. In addition to a zero average velocity, the forcing velocity is antisymmetric about the vertical centerline of the domain when n is even. These two features make even values of n important and interesting.

4.3 Initial conditions

The flow is initiated from rest for some cases, and initiated with a prescribed flow for other cases, the goal being to determine all possible steady flow patterns. The prescribed flow could be chosen from an unlimited selection, and practical considerations force a choice from a small set.

The initial conditions that are employed in the present results are a spanwise pattern of vortices. The number of spanwise vortices is indicated by m . A schematic of the various cases is shown in figure 4-1. Note that the $(m, n) = (1, 2)$ case is the symmetric driven cavity of Farias and McHugh [4]. Many other possibilities exist for initial conditions, and it remains to be seen whether other choices will induce new and different steady flows.

The initial conditions vary from $m = 0$ to $m = 64$. Note that $m = 0$ indicates that the flow starts from rest. The spanwise pattern of vortices that are used as initial conditions for $m \neq 0$ are created using the same driven cavity simulation, performed with different parameter values. The value of n (the forcing mode) is set equal to the desired value for m (the initial condition mode), the simulation starts from rest and is allowed to reach steady state. The Reynolds number for all initial conditions was chosen to be 100. The magnitude of the initial condition is adjusted by direct multiplication of all variables by a fixed constant. The resulting velocity field is used to initiate a simulation with a different value of n . Consider for example the $(m, n) = (1, 2)$ case with a Reynolds number of 1000 that was considered by Farias and McHugh [4]. The initial conditions for this case are created by starting a simulation from rest with $n = 1$ and $R_e = 100$. The steady results are then used to initiate a simulation with $n = 2$, now setting $R_e = 1000$, and the flow is allowed to evolve naturally.

4.4 Traditional driven cavity

Before treating the case of sinusoidal forcing, consider again the constant forcing, as in the traditional driven cavity of Ghia [3]. The traditional driven cavity has the constant forcing ($U = 1$ at the top), a square cavity ($\gamma = 1$), and is started from rest. The results of Farias and McHugh [4] suggest that perhaps there are other steady solutions, besides the one determined by Ghia [3], and that these may be found with a strategic choice of initial conditions. This possibility is investigated here for the square cavity, and for a rectangular cavity with $\gamma = \frac{1}{2}$.

The traditional driven cavity, with $\gamma = 1$ and starting from rest, is treated in the previous

chapter, and the results were shown to match previous results. Figure 4-2 (a) to (c) show the streamlines for this case for Re of 100, 400, and 1000. Note that the streamlines are determined from the velocity field by first calculating vorticity, defined to be the curl of the velocity, which in two-dimensions is

$$\eta = \frac{\partial v}{\partial x} - \frac{\partial u}{\partial y}, \quad (4.4)$$

where η is the vorticity. The vorticity is then used to determine the stream function using the equation

$$\nabla^2 \psi = \eta, \quad (4.5)$$

where ψ is the streamfunction. Streamlines are then determined by finding contours of the streamfunction. All streamlines shown in this chapter are determined in this manner. Note that ∇^2 and the other derivatives in (4.4) and (4.5) are approximated with the same finite difference methods discussed in chapter 3.

The traditional driven cavity flow is treated again, now starting with a disturbance of chosen magnitude to determine the existence of other steady flows. The initial conditions were a row of vortices as described before. The initial condition mode numbers of 2, 3, 4, 6, and 8 were considered. The Reynolds numbers were again chosen to be 100, 400, and 1000. The magnitude of the initial condition for $m = 3$ ranges over $0 < \underline{u} < 0.18$. The magnitude of the initial conditions for even values of m was changed with the same multiplicative constants as the $m = 3$ case, even though initial values of \underline{u} are zero. The results of the simulations show that the flow for all m with any initial magnitude are the same; the initial disturbance experiences a period of adjustment, finally converging on same steady flow pattern as the traditional driven cavity. No other steady solution has been found for this case. Note that there may still be another steady nonlinear solution, but can only be reached with an as yet undetermined disturbance.

In a further attempt to induce a possible second solution, the traditional driven cavity was allowed to reach steady state, and then the sense of the forcing was suddenly changed, such that the direction of forcing was in the opposite direction. The flow was then allowed

to evolve to steady state again. The results still show only one steady solution; the same flow as found by Ghia [3] and others. It seems unlikely that there is a second solution for this case.

Further simulations considered the traditional driven cavity problem with a different aspect ratio, $\gamma = \frac{1}{2}$, using the same range of m and \underline{u} as above. Figure 4-3 shows the resulting streamlines for the steady flow case when started from rest. Once again, a second steady solution has not appeared. All the simulations with different m and \underline{u} evolve to the same final steady flow as the flow that is started from rest.

Some comments will now be made concerning the $\gamma = \frac{1}{2}$ case, for future discussion. Note in figure 4-3 that the center of the primary vortex is no longer near the center of the cavity, but is shifted to the right, in the same direction of forcing. The forcing seems to ‘drive’ the vortex toward the right wall, almost to the point where the vortex will fit in the right half of the domain, and approximately mimic the behavior of the cavity with $\gamma = 1$. Note that the vortex center is shifted upward from the $\gamma = 1$ case.

The value of ψ_{max} has also increased for the $\gamma = \frac{1}{2}$ case. The parameter, ψ_{max} , is another variable typically used to validate numerical methods. Table 4.1 gives a quantitative comparison between the $\gamma = 1$ and $\gamma = \frac{1}{2}$ cases.

Table 4.1: Location of primary vortex

Method	Re	ψ_{max}	x	y
$\gamma = 1$	100	0.1010	0.6122	0.7331
	400	0.1129	0.5528	0.5995
	1000	0.1129	0.5411	0.5613
$\gamma = \frac{1}{2}$	100	0.1218	0.6977	0.6592
	400	0.1271	0.6899	0.5891
	1000	0.1365	0.6591	0.5736

4.5 Results with a square cavity

The symmetric driven cavity is now considered in a square cavity, $\gamma = \frac{H}{L} = 1$. Forcing mode numbers, n , of 2, 3, 4, 6, and 8 are considered in detail in this section. Several higher mode numbers are considered in the next section. The results show that the bifurcation sequence for each forcing mode number is significantly different. Each forcing mode number will be discussed sequentially, followed by some general remarks.

4.5.1 $n = 1$

The $n = 1$ case in a square cavity is very similar to the traditional driven cavity, the only difference being that the forcing here is sinusoidal with a half period across the top, while the traditional driven cavity is constant across the top. The simulations for this case show that there is only one steady flow pattern for all initial conditions considered, and this resulting steady flow is very similar to the traditional driven cavity discussed above. No second solution has been found for this case.

4.5.2 $n = 2$

The $n = 2$ case is the same case considered by Farias and McHugh [4]. Note that they only used initial conditions with $m = 0$ or $m = 1$; they did not consider higher m , and they took Re to be less than 3000. As discussed above, Farias and McHugh found two steady solutions for the $n = 2$ case; a symmetric and an asymmetric solution. The same case is considered here for several reasons; 1) further validation of the computational methods, 2) to extend the highest Reynolds number considered Farias and McHugh, thereby finding the largest Reynolds number where an asymmetric steady solution may exist, and 3) to determine any other steady solutions that may exist but were not previously found.

The results are shown in figure 4-4. Figure 4-4(a) shows the locus of values of \underline{u} for the asymmetric steady solutions. Also shown in figure 4-4(a) are the results of Farias and McHugh, which clearly agree with the present results. Furthermore, although not shown in the figure, all the features of the bifurcation diagram of Farias and McHugh are reproduced

with the present methods.

Note in 4-4(a) that the asymmetric steady solution exists for Reynolds number up to approximately 3700. Simulations for a Reynolds number of 3800 shows oscillating flow; steady flow no longer exists. Reynolds numbers as high as 4500 were considered, always resulting in unsteady flow. The flow pattern, however, does not show any remarkable changes as the Reynolds number is increased in subsequent cases up to 4500. Figure 4-4(c) and 4-4(d) show the resulting flow patterns for the unsteady flow for two different Reynolds numbers at the same time in the simulation.

Figure 4-4(b) shows a time history of \underline{u} for the unsteady case with two Reynolds numbers. Time histories of \underline{u} are widely used throughout this study to indicate the behavior of the flow. Figure 4-4(b) shows that the flow for $R_e = 3800$ evolves into a periodic pattern. However, the flow for $R_e = 4500$ is not periodic. It appears therefore that at least one more bifurcation has occurred in this interval. The current focus is on steady flows with different forcing; unsteady bifurcations are beyond the present scope, and are not pursued in depth here.

The simulations with higher values of m do not result in any new steady or unsteady solutions. All simulations converge to either the symmetric or asymmetric solution. In fact, as will be shown, no case has been found when there are more than two steady solutions for the same parameter values and forcing pattern.

4.5.3 $n = 4$

The $n = 4$ case has two complete periods of forcing across the top of the cavity, and would be expected to drive a steady symmetric flow with four vortices across the cavity, at least for low Reynolds number. This symmetric steady flow is found to exist, and the flow pattern is shown in 4-5(a) for a Reynolds number of 600. Note that the simulation for the flow in 4-5(a) is started from rest ($m = 0$). Also note that the flow pattern is symmetric about the cavity centerline, however, the four vortices are not all equal. The flow is dominated by two vortices, and the streamlines pattern appears to mimic the $n = 2$ case, except near the top

of the cavity.

As the Reynolds number is increased beyond 670, an asymmetric steady flow also exists, analogous to the $n = 2$ case. The second steady flow can only be achieved if the flow is initiated with a sufficiently strong asymmetric motion. The flow pattern for this asymmetric flow is shown in figure 4-5(b). The locus of values of \underline{u} for the asymmetric steady flows is shown in 4-6(a). The dashed line in figure 4-6(a) distinguishes the two possibilities; initial conditions with \underline{u} above the dashed line will evolve to the asymmetric solution, while those below the dashed line will evolve to the symmetric solution. Note that a value of \underline{u} on the dashed line corresponds to an initial value, rather than a final steady value. Time histories of \underline{u} shown in 4-6(c) show two examples at the same Reynolds number; one converges to a symmetric solution, and the other to an asymmetric solution, the only difference being the magnitude of the initial condition. Note that the dashed line in 4-6(a) applies to asymmetric disturbances only. Symmetric disturbances, $m = 2, 4, 8$, only result in symmetric steady flows.

Simulations starting from rest with Reynolds number greater than 1350 evolve into a steady flow, but it is the asymmetric steady flow. The symmetric steady flow no longer exists beyond $R_e > 1350$. The time histories in 4-6(d) demonstrate this fact by comparing three different initial conditions; they all converge on the same asymmetric steady solution. These results indicate a different scenario than the $n = 2$ case of Farias and McHugh [4]. There is no Reynolds number for the $n = 2$ case where the flow initiated from rest will evolve into an asymmetric steady motion; instead, simulations for higher R_e started from rest evolve into an unsteady solution.

Note that for the present $n = 4$ case, simulations starting from rest also evolve into an unsteady solution, but only for Reynolds number larger than 3800, where no steady solutions exist.

The streamline patterns for the asymmetric solution in 4-5(b) has a much different character than for the symmetric solution, shown in 4-5(a). The lower region of the cavity for the asymmetric flow is dominated by a single large vortex, occupying the entire width of

the cavity. The spatial oscillation of the forcing is not reflected in the 'bottom flow'. This is an example of a system where complicated surface forcing can result in much simpler motion in most of the domain.

Flow in the unsteady case is shown for one time value in figure 4-5(c). This flow can be characterized as an oscillating pendulum-like motion of the vortices.

4.5.4 $n = 6$

For low Reynolds number, all m result in the same final steady solution, shown in figure 4-7(a). The streamline pattern in figure 4-7(a) is symmetric, and shows six distinct vortices, as expected. Note however that the vortices are not identical.

The behavior as Reynold number is increased is somewhat different than the $n = 4$ case. There is a value of R_e of approximately 440 which separates the symmetric steady solution from asymmetric behavior. Beyond this critical R_e , a steady asymmetric flow exists, but the steady symmetric flow does not exist. No overlap region was found where both symmetric and asymmetric solutions can exist, as shown in figure 4-8(a). Now, whatever the initial condition, if R_e is larger than 440, all initial conditions, including symmetric ones, and starting from rest, converge to the same asymmetric solution.

The $n = 2$ and $n = 4$ case clearly show a symmetry breaking subcritical bifurcation pattern. The present $n = 6$ case is symmetry breaking, but apparently not subcritical. This subcritical feature depends on the overlap interval of Reynolds number, where the symmetric and asymmetric steady solutions can both exist. Although no overlap region was found, it may exist for a very small interval of Reynolds number, but could not be determined given available computer resources.

The flow pattern for this asymmetric flow is shown in figure 4-7(b) and 4-7(c). There are still six distinct vortices, but it is no longer true that the vortices are isolated; there are clearly streamlines shared by vortices, and larger scale vortex motion in the lower part of the domain.

As Reynold number is increased beyond a value of approximately 900, the only solution

is unsteady flow; steady motion is no longer possible. Figure 4-8(b) shows a time history of \underline{u} with Re of 1000. The motion is clearly unsteady, and appears to be settling to a periodic behavior with very complicated structure. Also shown in figure 4-8(b) are time histories of \underline{u} for a steady symmetric and steady asymmetric case. An example of the streamline pattern for the unsteady flow is given in figure 4-7(d).

4.5.5 $n = 8$

The results for the $n = 8$ case are qualitatively the same as the $n = 6$ case. There is a low Reynolds number range, $0 < Re < 500$, where the only steady solution is symmetric, an intermediate range, $500 < Re < 1150$, where the only steady solution is asymmetric and finally a higher Reynolds number range where the solution is always unsteady. There is no overlap region that could be found between the steady symmetric and asymmetric intervals, hence this bifurcation does not appear to be subcritical. Time histories of \underline{u} shown in figure 4-10 illuminate this behavior.

Figure 4-9 shows the streamlines for this case. Again, there are clearly eight distinct vortices for the steady symmetric case, each of which consist of closed streamlines. The asymmetric steady case does not have closed streamlines, and has the large scale vortex motion in the center of the cavity.

4.6 Results with a rectangular cavity

Now consider the symmetric driven cavity with a rectangular shape using $\gamma = \frac{1}{2}$. Again, the results depend on the forcing pattern, and will be discussed sequentially. The $n = 1$ case was found to match the traditional driven cavity with $\gamma = \frac{1}{2}$, discussed previously, and will not be discussed further.

4.6.1 $n = 2$

This case is the same as the case of Farias and McHugh [4] except for the aspect ratio. The bifurcation diagram for this case is shown in figure 4-11(a). For low Reynolds numbers,

the only solution is a steady symmetric flow. An asymmetric flow appears at a Reynolds number of approximately 2885, and two steady solutions are possible for $2885 < R_e < 3900$. Above R_e of 3900, the asymmetric steady solution no longer exists. Simulations initiated with a strong initial condition will exhibit an unsteady behavior.

The symmetric steady solution exists up to a Reynolds number of 8900. Simulations initiated from rest, or initiated with very weak initial flow, will evolve into the symmetric steady motion. Simulations started from rest with Reynolds numbers above 8900 will evolve into an unsteady solution. This is the same behavior as the case of Farias and McHugh [4] except that the asymmetric steady flow terminates at a lower R_e than the symmetric flow.

The symmetric flow pattern is shown in figure 4-12(a). The asymmetric pattern is shown in 4-12(b). Note that the asymmetric pattern has the right-hand vortex intact, while the left-hand vortex is segmented into what appears to be several smaller vortices. This pattern persists until the Reynolds number reaches approximately 3900. Beyond this value, the steady asymmetric solution is no longer obtained. The flow becomes unsteady, although the same basic pattern of flow is observed. A much higher Reynolds number, R_e of 9900, also results in an unsteady flow, with the streamline pattern, at times, closer to the symmetric solution, as shown in 4-12(d).

4.6.2 $n = 4$

The $n = 4$ case with $\gamma = \frac{1}{2}$ is of particular interest. One half of the domain is nearly the same as the previous work of Farias and McHugh [4], the only difference being the free boundary that the half domain would feel at the centerline. One might speculate that this case would allow the same two solutions found by Farias and McHugh in each half of the cavity, and an additional steady flow involving the entire domain. Hence this case seems like the best possibility for a third steady solution. However, the simulations show only two solutions, as before. Furthermore, the bifurcation pattern has a very unexpected behavior.

The bifurcation diagram is shown in figure 4-13(a). There is again a symmetric steady solution for low Reynolds numbers. As the Reynolds number is increased, two intervals of

asymmetric flows appear. One interval is approximately $2450 < R_e < 2750$, and the other is approximately $3900 < R_e < 4200$. Within both of these intervals, a symmetric and an asymmetric solution can exist, depending on initial conditions. The dashed lines in 4-15(a) indicate the basin of attraction for these two possible solutions.

Between these two intervals, all simulations, including those started from rest, do not converge on a steady solution, but instead appear to oscillate in a nonperiodic manner. A time history of \underline{u} for this case is shown in 4-15(c). A variety of simulations were performed in this intermediate region between the steady solutions, trying to achieve a steady flow of any type. In all cases, the flow did not converge to a steady result. The simulations are limited to a finite duration, and it is possible that very long simulations would finally become steady, although this seems unlikely.

The streamline pattern for the symmetric steady flow is shown in figure 4-14(a). The streamline pattern for the asymmetric steady flow is shown in figure 4-14(b) for the first interval and figure 4-13(c) for the second interval. Note that there is no dramatic change in the flow pattern between the two intervals. The vortices for the symmetric solution fill the height of the cavity, while the vortices for the asymmetric solutions do not. The streamline pattern for the two intervals of unsteady flow are shown in figure 4-13(d) and (e) and show a similar transition.

4.6.3 $n = 6$

The bifurcation behavior for the $n = 6$ case mimics the behavior of the $n = 6$ case for a square cavity. A symmetric steady flow exists for low Reynolds numbers, up to approximately 1800. Beyond this value, the symmetric steady solution does not exist. Instead, an asymmetric steady solution exists. The asymmetric steady solution results even when the flow is initiated from rest, or with a symmetric disturbance. There is no overlap region where two steady solutions are possible, as before. The asymmetric steady flow region terminates at a Reynolds number around 8400, beyond which all cases are unsteady.

The bifurcation diagram is shown in figure 4-15, along with time histories of \underline{u} . Stream-

line patterns are shown in figure 4-16. The streamline patterns show a fundamental change from the symmetric solution to the asymmetric solution, as in the $n = 4$ case, only more dramatic. The vortices for the symmetric solution extend the entire depth of the cavity. The vortices for the asymmetric solution are clearly a pattern of vortices where each vortex has approximately round streamlines, and individual vortices do not have a length scale that is related to the size of the cavity.

4.6.4 $n = 8$

The $n = 8$ case shows the symmetric steady pattern for Reynolds numbers up to approximately 700. However, no second steady pattern appears. All simulations for Reynolds numbers greater than 700 are unsteady.

Time histories of \underline{u} shown in figure 4-17 indicate that the unsteady solution for moderate Reynolds numbers, $Re = 750$ for example, result in a periodic solution, implying that the system has undergone a Hopf bifurcation. Streamline patterns for both the steady symmetric flow and the unsteady periodic flow are shown in figure 4-17.

4.7 Higher forcing mode numbers

Forcing with higher mode numbers is now considered for a few cases. This part of the study is motivated by geophysical flows, such as flow in lakes and other confined bodies. The air motion on the lake surface may be quite complicated, even turbulent. It seems possible, based on the work already discussed, for a complicated flow with a very small length scale to drive a large scale motion in the lake. This may happen even if the net velocity on the surface is zero.

The simulations are considered with n of 16, 32, and 64, with both the square cavity, $\gamma = 1$, and the rectangular cavity, $\gamma = \frac{1}{2}$. All cases show the same basic bifurcation behavior. There is a region of low Reynolds number where only a steady symmetric solution exists. Then an intermediate region where only a steady asymmetric solution exists. There is no overlap between these two intervals of Reynolds number. Finally, unsteady flow results

for all initial conditions. The critical Reynolds numbers that denote the endpoints of the intervals depend strongly on n . For example, the square cavity with $n = 64$ did not experience unsteady motion until a Reynolds number of 15000, approximately, which is considerably larger than any case with smaller n . Table 4.2 lists the critical Reynolds numbers for all cases considered in this section. Figure 4-18 is the graphical representation of the results.

An example of the streamline patterns for the symmetric and the asymmetric flow for each case are shown in figures 4-19 to 4-24. Note that for the high mode number cases considered here, with a short length scale for the forcing oscillation, that the strong forcing effect does not penetrate the domain very far. The flow throughout the rest of the domain in all cases is quite simple, compared to the forcing region, and is composed of one or two vortical regions. Note in particular figure 4-22 for $n = 16$. The large scale flow for this case has a remarkable similarity to the traditional driven cavity flow in the rectangular geometry, discussed earlier; a single vortex displaced to one side. It seems that it is indeed possible for a complicated forcing to cause a large scale current.

Table 4.2: Range of R_e for asymmetric solution at higher forcing functions

Forcing function	Range of R_e ($\gamma = 1$)	Range of R_e ($\gamma = \frac{1}{2}$)
$16\pi x$	750 - 3050	600 - 1125
$32\pi x$	2350 - 7300	1575 - 3900
$64\pi x$	6800 - 15000	5000 - 9200

4.8 Discussion

The existence of two steady solutions begs for an explanation. It is difficult to provide a complete explanation at this stage. However, the combined results do offer one possibility. In particular, consider the $n = 6$ case with $\gamma = \frac{1}{2}$. The symmetric steady flow shows six

vortices whose streamlines are distorted so that all six vortices fit into the cavity and occupy approximately the same territory. The asymmetric flow shows that the vortices no longer fit the boundary, and they have approximately round streamlines.

This result suggests that the vortices tend to form patterns where each vortex has round streamlines. The vortices conform to the boundary only at low Reynolds numbers, where there is not sufficient momentum for the flow to shake the constraint imposed by the boundary. Hence, the steady solutions may be composed of 1) boundary fitted vortices, and 2) free vortices. The more complicated unsteady flows may result when these two cases are in direct competition.

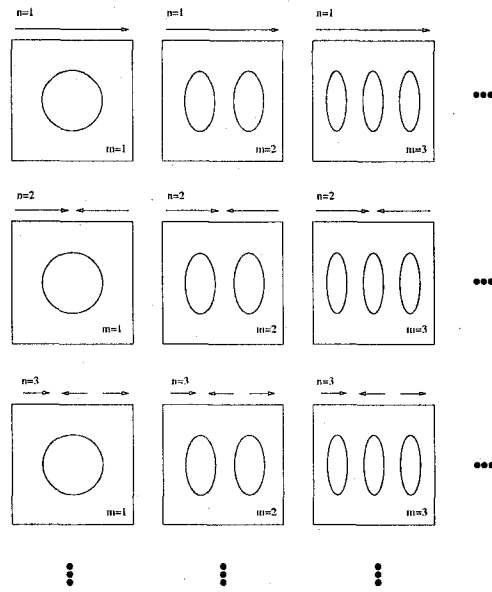
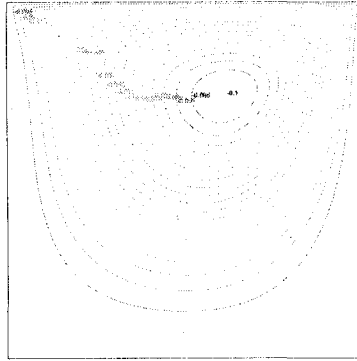
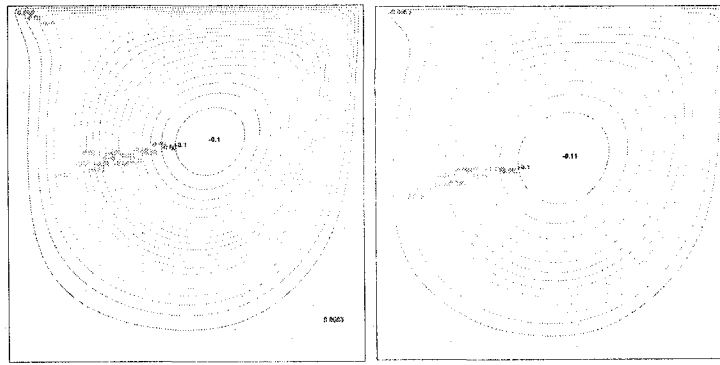


Figure 4-1: Schematic of the various combinations of forcing and initial flow



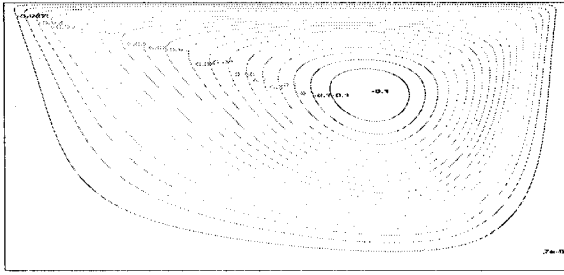
(a) $Re = 100$



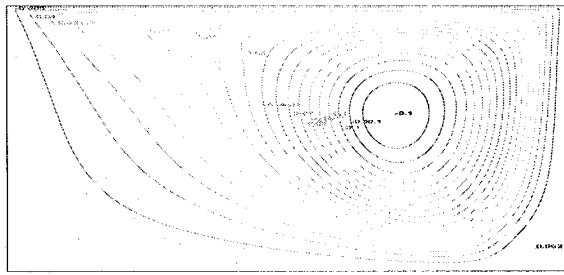
(b) $Re = 400$

(c) $Re = 1000$

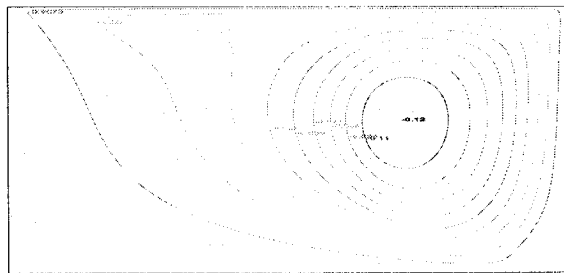
Figure 4-2: Streamlines for the traditional driven cavity with $\gamma = 1$



(a) $Re = 100$

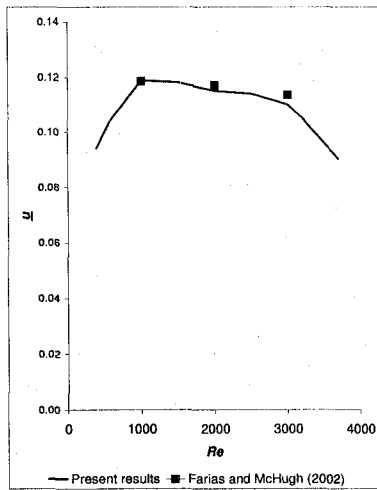


(b) $Re = 400$

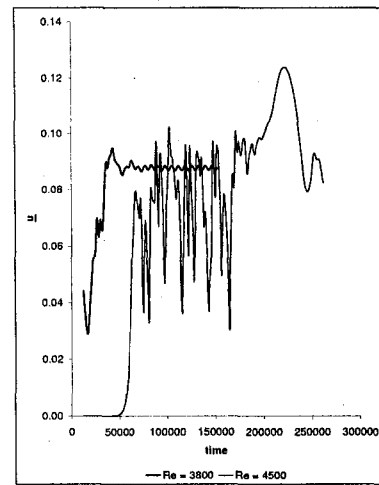


(c) $Re = 1000$

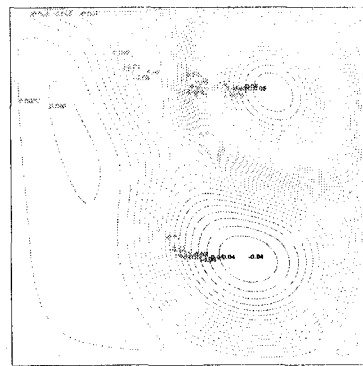
Figure 4-3: Streamlines for the traditional driven cavity with $\gamma = \frac{1}{2}$



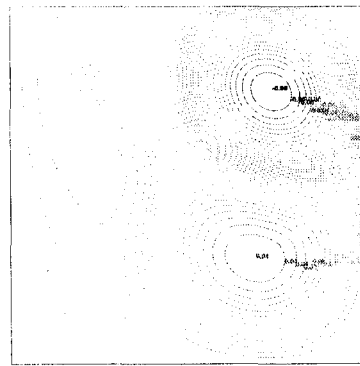
(a)



(b)

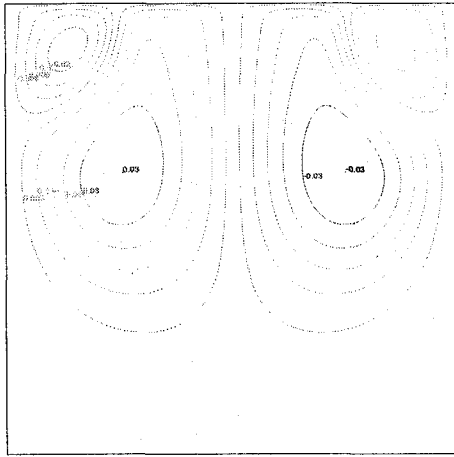


(c)

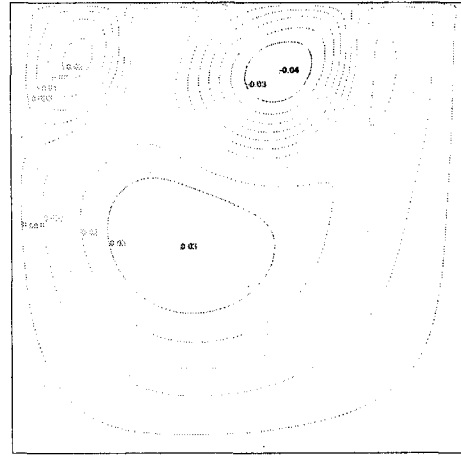


(d)

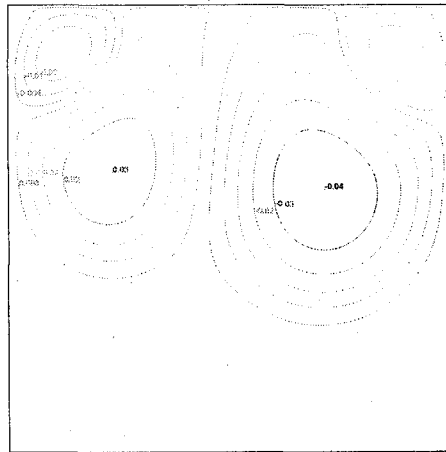
Figure 4-4: Results with $\gamma = 1$ and $n = 2$: (a) locus of values for \underline{u} for steady flow, (b) time histories of \underline{u} for different R_e for unsteady flow, (c) streamlines for the unsteady flow, $R_e = 3700$, and (d) streamlines for the unsteady flow, $R_e = 4500$



(a)

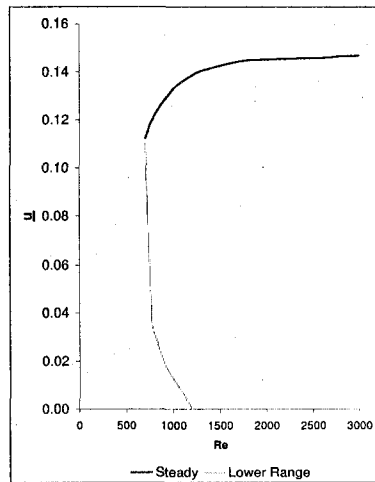


(b)

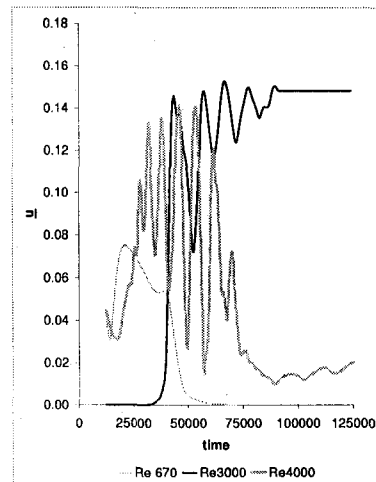


(c)

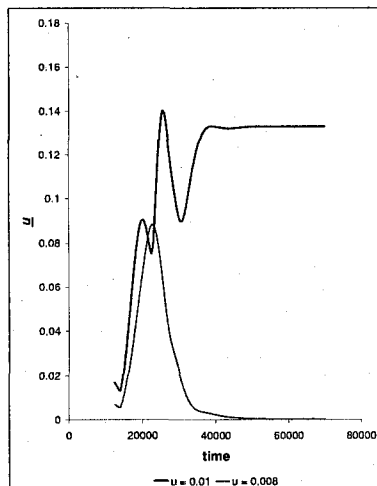
Figure 4-5: Results with $\gamma = 1$ and $n = 4$: (a) streamlines for the steady symmetric solution, $R_e = 600$, (b) streamlines for the steady asymmetric solution, $R_e = 700$, and (c) streamlines for the unsteady flow, $R_e = 3000$



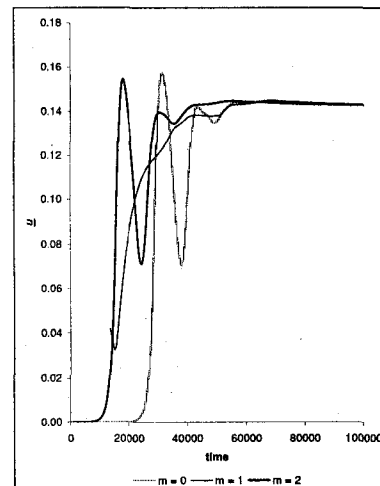
(a)



(b)

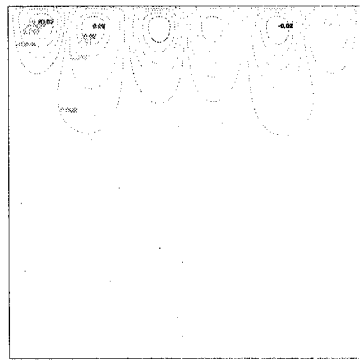


(c)

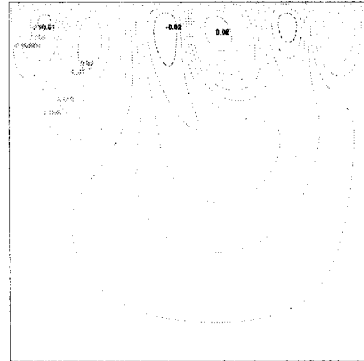


(d)

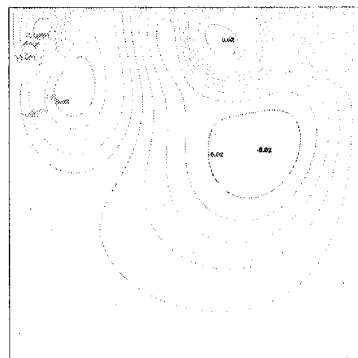
Figure 4-6: Results with $\gamma = 1$ and $n = 4$. (a) locus of values \underline{u} for steady flow, (b) time histories of \underline{u} , (c) time histories of \underline{u} for $Re = 1000$ starting with different vortex magnitudes, $m = 1$, and (d) time histories of \underline{u} for $Re = 1500$ with different initial mode number



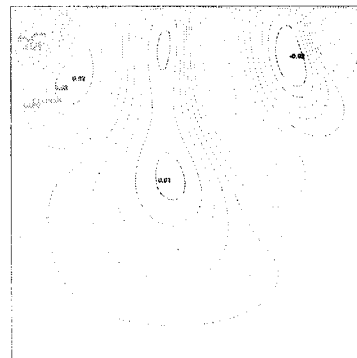
(a)



(b)

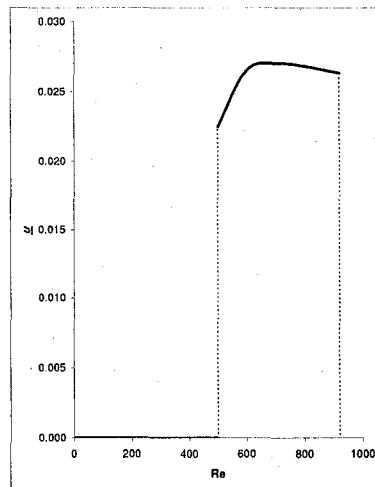


(c)

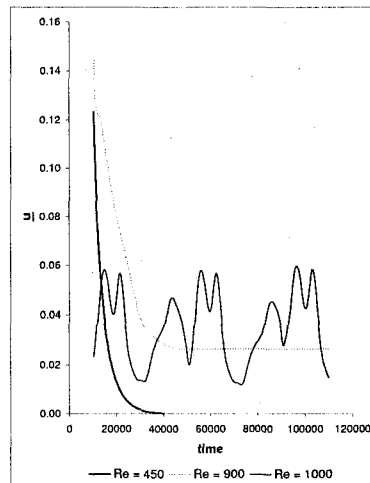


(d)

Figure 4-7: Results with $\gamma = 1$ and $n = 6$: (a) streamlines for the symmetric solution, $R_e = 400$, (b) streamlines for the asymmetric solution, $R_e = 500$, (c) streamlines for the asymmetric solution, $R_e = 900$, and (d) streamlines for the unsteady flow, $R_e = 1000$

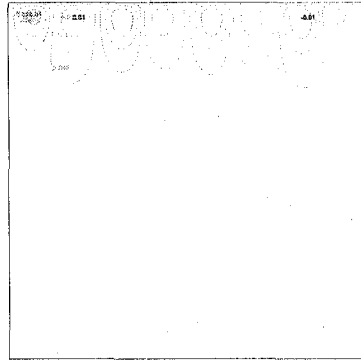


(a)

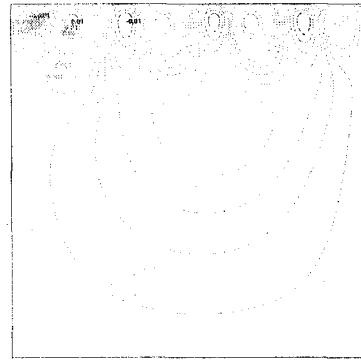


(b)

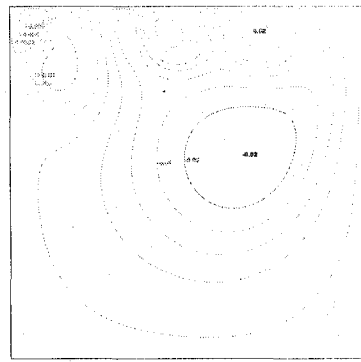
Figure 4-8: Results with $\gamma = 1$ and $n = 6$: (a) loci of values of \underline{u} for steady flow (b) time histories of \underline{u} for different Re and $m = 1$



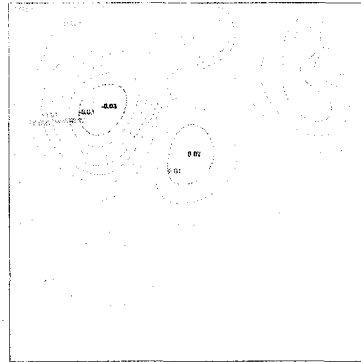
(a)



(b)

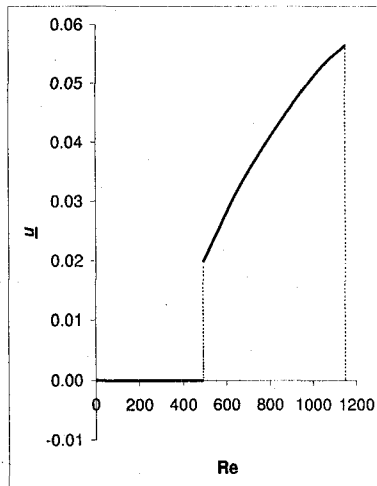


(c)

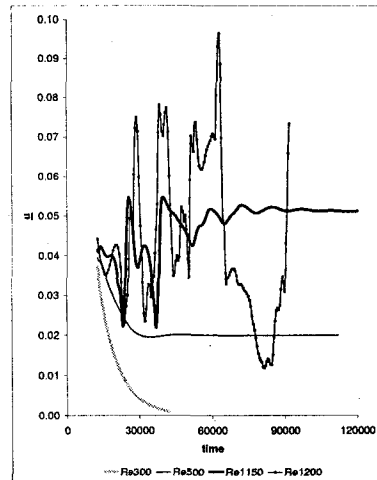


(d)

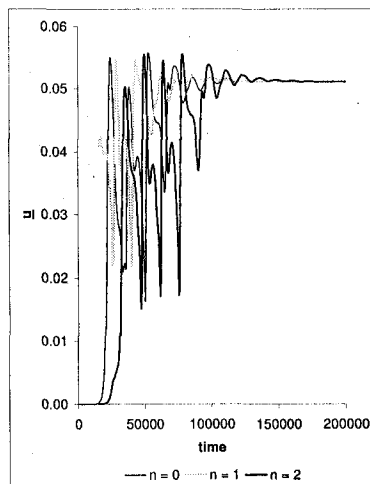
Figure 4-9: Results with $\gamma = 1$ and $n = 8$ (a) streamlines for the symmetric solution, $Re = 400$, (b) streamlines for the asymmetric solution, $Re = 600$, (c) streamlines for the asymmetric solution, $Re = 1150$, and (d) streamlines for the unsteady flow, $Re = 1500$



(a)

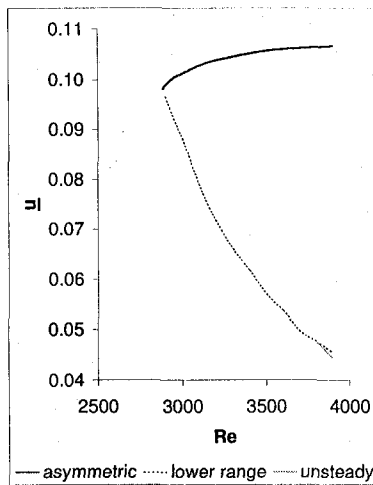


(b)

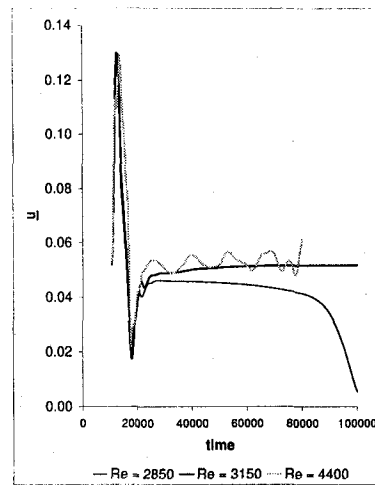


(c)

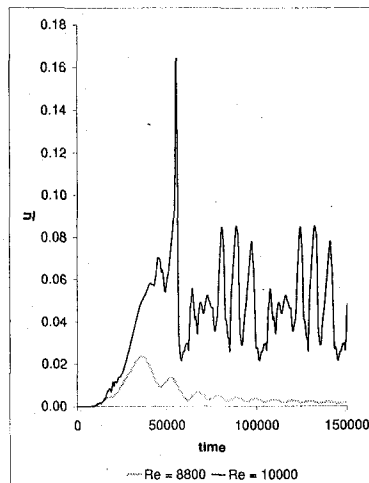
Figure 4-10: Results with $\gamma = 1$ and $n = 8$: (a) loci of values for \underline{u} for steady solution, (b) time histories of \underline{u} for different Re , $m = 1$, and (c) time histories of \underline{u} for various initial conditions, $Re = 1000$



(a)

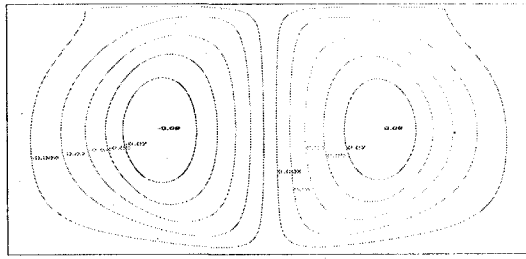


(b)

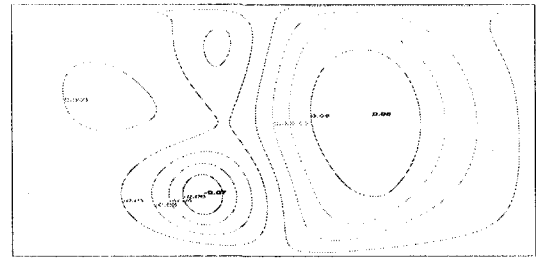


(c)

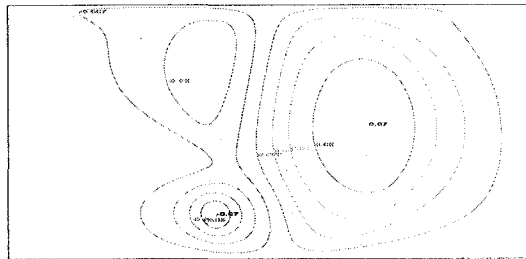
Figure 4-11: Results with $\gamma = \frac{1}{2}$ and $n = 2$: (a) loci of values of u for steady flow, (b) time histories of u for several Re showing a symmetric, an asymmetric and an unsteady case, and (c) time histories of u starting from rest near critical Re .



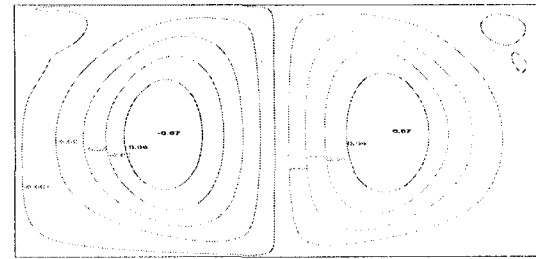
(a)



(b)

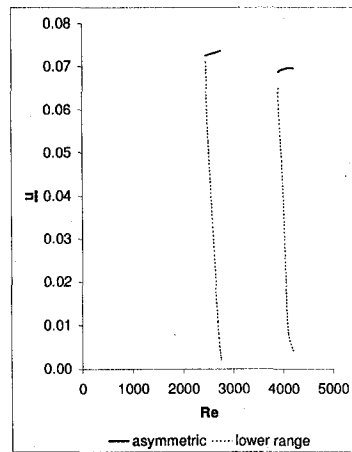


(c)

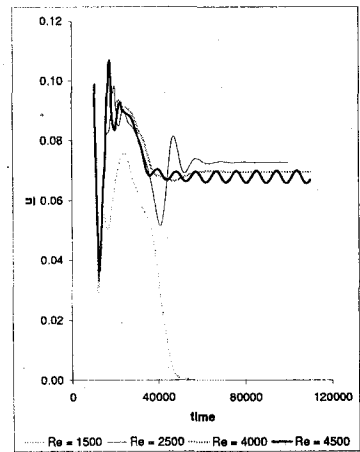


(d)

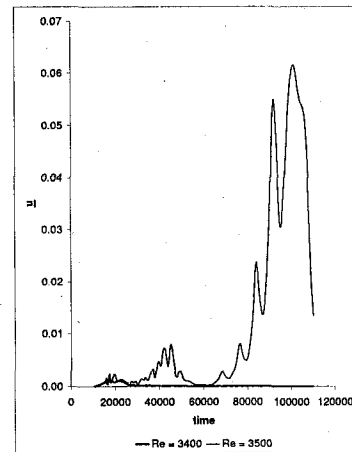
Figure 4-12: Results with $\gamma = \frac{1}{2}$ and $n = 2$: (a) streamlines for the symmetric solution, $R_e = 2850$, (b) streamlines for the asymmetric solution, $R_e = 2885$, (c) streamlines for the unsteady flow, $R_e = 4100$, and (d) streamlines for the unsteady flow, $R_e = 9900$



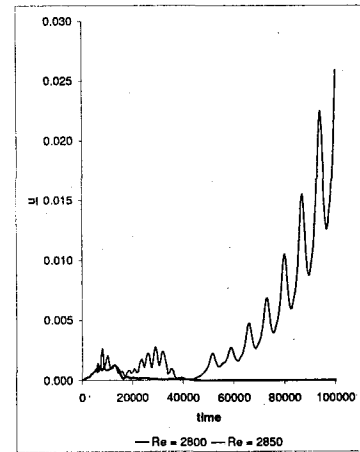
(a)



(b)

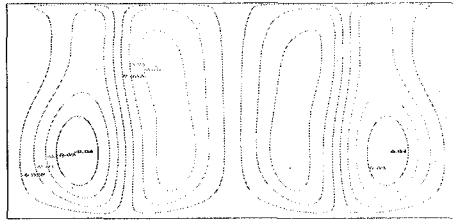


(c)

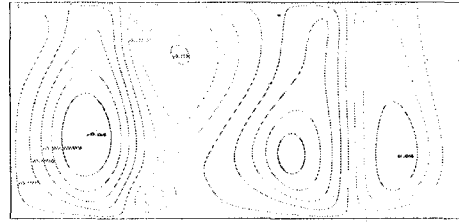


(d)

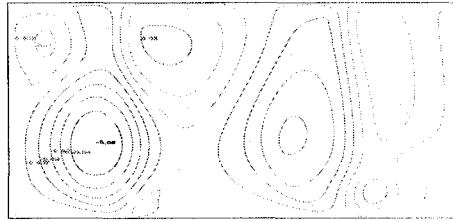
Figure 4-13: Results with $\gamma = \frac{1}{2}$ and $n = 4$: (a) loci of values of \underline{u} for steady flow, (b) time histories of \underline{u} for different Re , $m = 1$, and (c)-(d) time histories of \underline{u} near critical Re



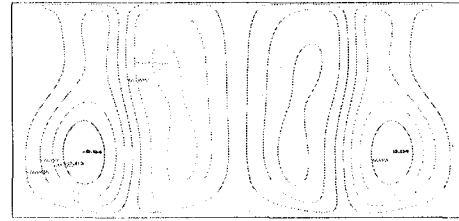
(a)



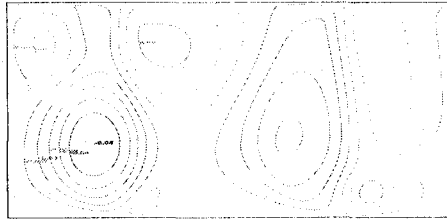
(b)



(c)

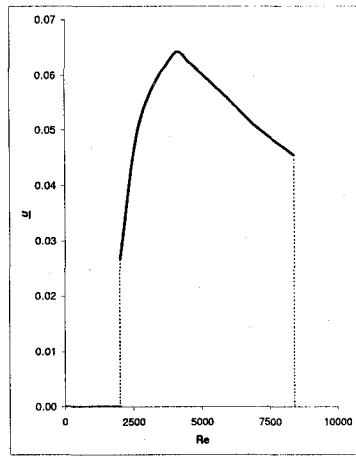


(d)

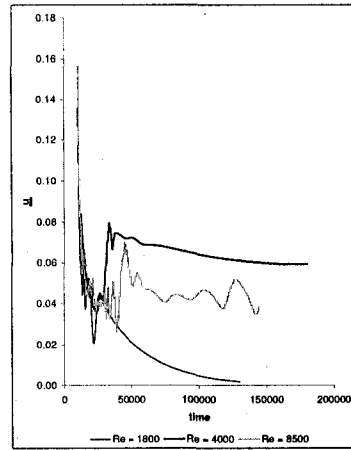


(e)

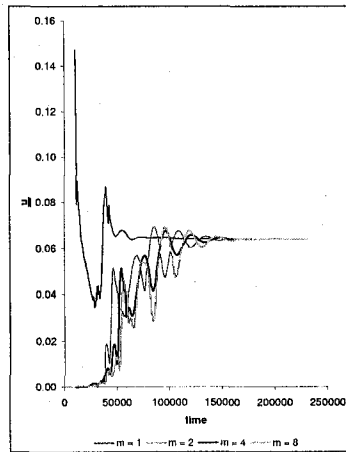
Figure 4-14: Results with $\gamma = \frac{1}{2}$ and $n = 4$: (a) streamlines for the symmetric solution, $R_e = 2400$, (b) streamlines for the asymmetric solution, $R_e = 2750$, (c) streamlines for the asymmetric solution, $R_e = 4200$, (d) streamlines for the unsteady flow, $R_e = 2800$, and (e) streamlines for the unsteady flow, $R_e = 4300$



(a)

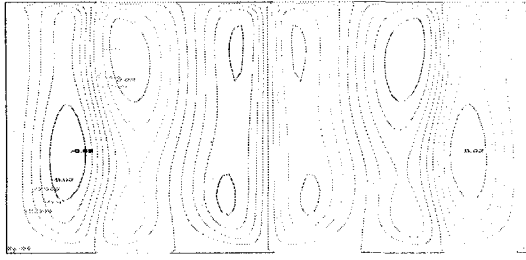


(b)

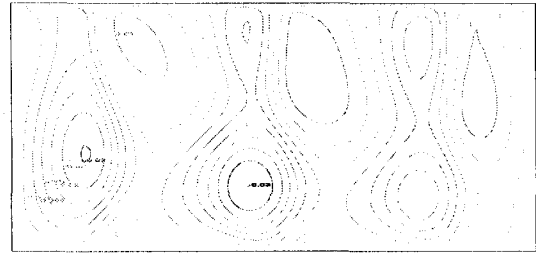


(c)

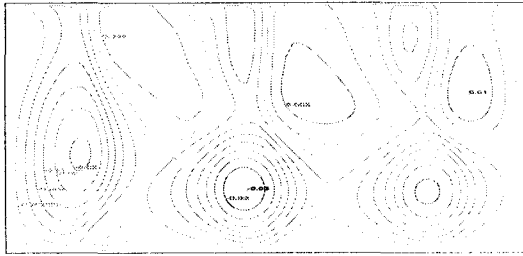
Figure 4-15: Results with $\gamma = \frac{1}{2}$ and $n = 6$: (a) loci of values of \underline{u} for steady solutions, (b) time histories of \underline{u} for different Re , $m = 1$, and (c) time histories of \underline{u} with different initial mode number, $Re = 3000$



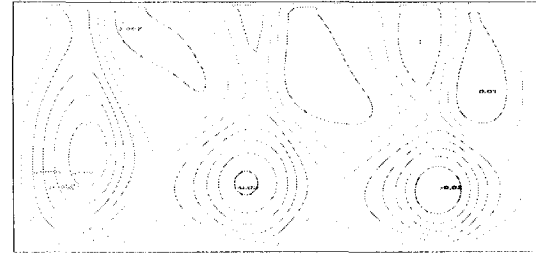
(a)



(b)

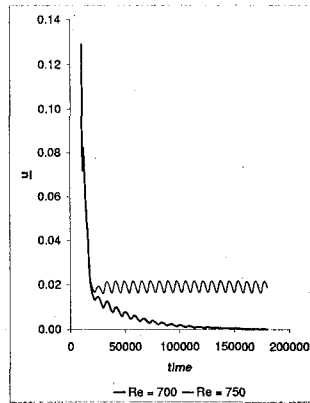


(c)

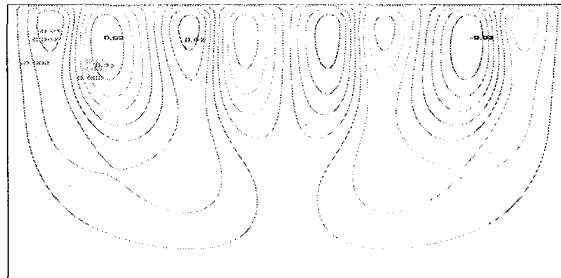


(d)

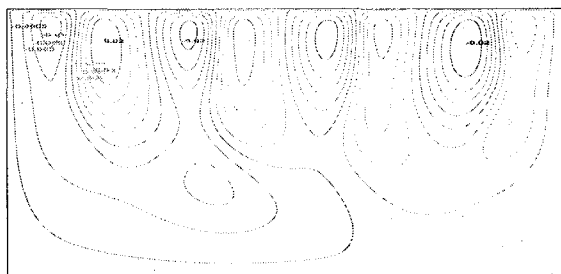
Figure 4-16: Results with $\gamma = \frac{1}{2}$ and $n = 6$: (a) streamlines for the symmetric solution, $Re = 1800$, (b) streamlines for the asymmetric solution, $Re = 3000$, (c) streamlines for the asymmetric solution, $Re = 7000$, and (d) streamlines for the unsteady flow, $Re = 8500$



(a)

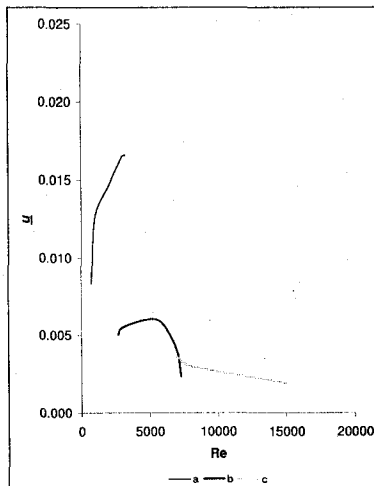


(b)

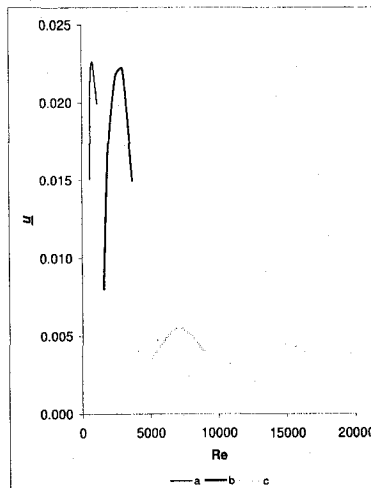


(c)

Figure 4-17: Results with $\gamma = \frac{1}{2}$ and $n = 8$: (a) time histories of u near critical R_e , $m = 1$, (b) streamlines for the symmetric solution, $R_e = 700$, and (c) streamlines for the unsteady flow, $R_e = 750$



(a) $\gamma = 1$



(b) $\gamma = \frac{1}{2}$

Figure 4-18: Loci of values of \underline{u} for steady solutions for higher forcing modes: line a - $n = 16$, line b - $n = 32$ and line c - $n = 64$

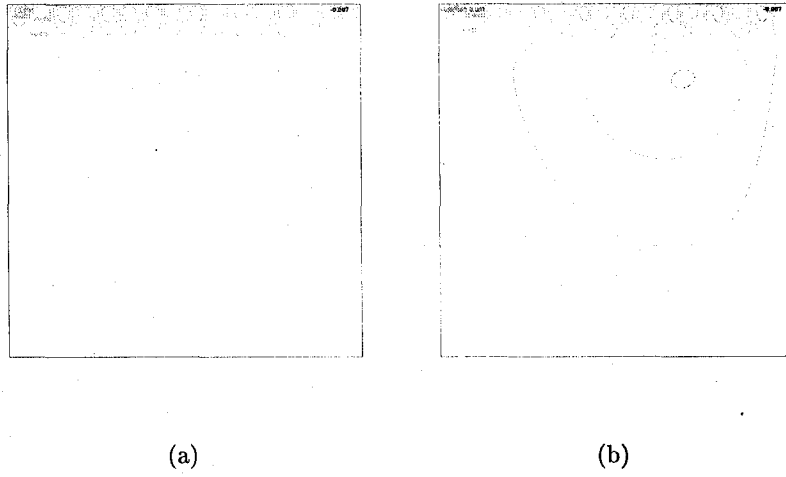


Figure 4-19: Results with $\gamma = 1$ and $n = 16$: (a) streamlines for the symmetric solution, $Re = 700$, and (b) streamlines for the asymmetric solution, $Re = 1000$

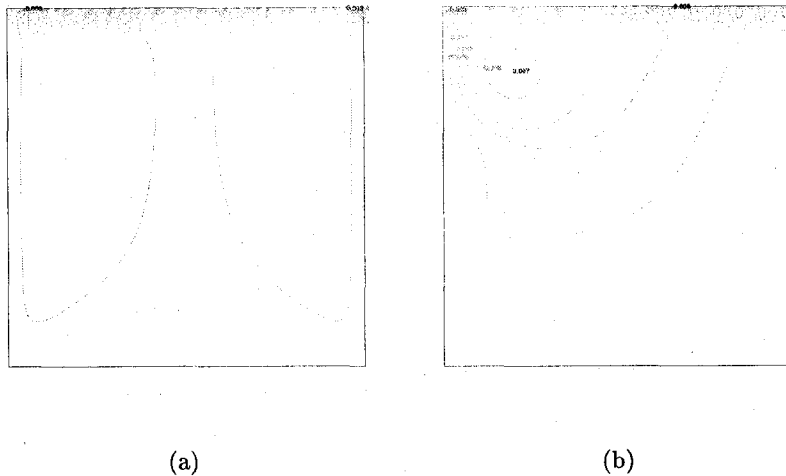
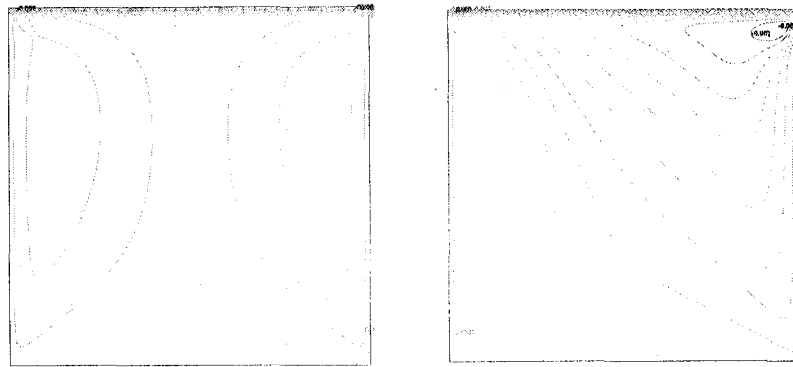


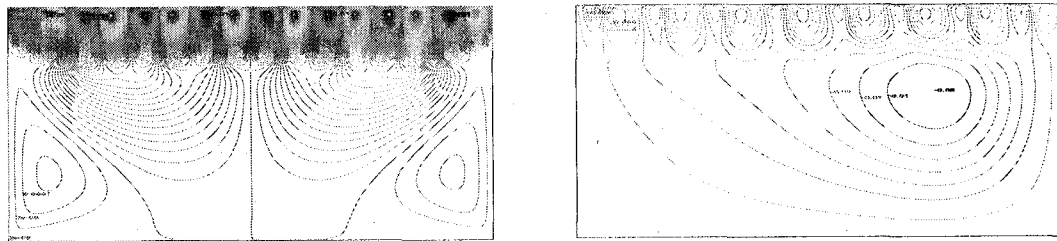
Figure 4-20: Results with $\gamma = 1$ and $n = 32$: (a) streamlines for the symmetric solution, $Re = 2700$, and (b) streamlines for the asymmetric solution, $Re = 2800$



(a)

(b)

Figure 4-21: Results with $\gamma = 1$ and $n = 64$: (a) streamlines for the symmetric solution, $R_e = 6700$, and (b) streamlines for the asymmetric solution, $R_e = 8000$



(a)

(b)

Figure 4-22: Results with $\gamma = \frac{1}{2}$ and $n = 16$: (a) streamlines for the symmetric solution, $R_e = 575$, and (b) streamlines for the asymmetric solution, $R_e = 800$

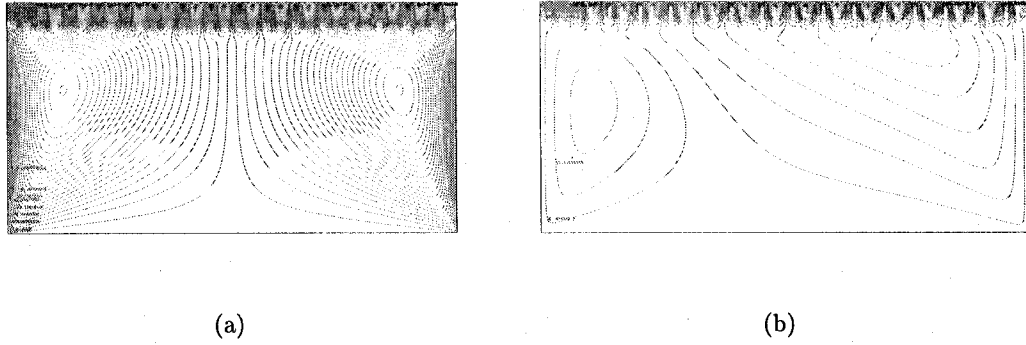


Figure 4-23: Results with $\gamma = \frac{1}{2}$ and $n = 32$: (a) streamlines for the symmetric solution, $Re = 1400$, and (b) streamlines for the asymmetric solution, $Re = 1500$

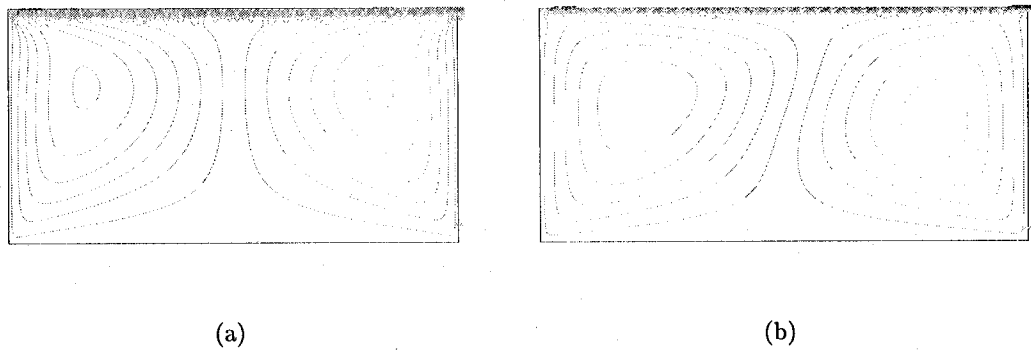


Figure 4-24: Results with $\gamma = \frac{1}{2}$ and $n = 64$: (a) streamlines for the symmetric solution, $Re = 4000$, and (b) streamlines for the asymmetric solution, $Re = 6000$

Chapter 5

Three-dimensional results

5.1 Preliminaries

Now consider the driven cavity in a three-dimensional rectangular prism. The forcing is again on the top of the cavity ($z = 1$), and has the added complexity that the direction may vary with position across the top. The initial conditions also may be significantly more complicated. Two types of forcing are considered; symmetric unidirectional forcing shown schematically in figure 5-1(a), and bidirectional forcing shown in figure 5-1(b).

The purpose of the symmetric unidirectional forcing is for comparison with the previously discussed two-dimensional simulations. The three-dimensional case shown in figure 5-1(a) would be expected to mimic the two-dimensional case with $n = 2$. Note that attention is restricted to the $n = 2$ case for the three-dimensional simulations.

Bidirectional forcing does not have a two-dimensional analog. The particular choice for bidirectional forcing shown in figure 5-1(b) has the interesting feature that the average velocity in any direction is zero, and the average first moment of the velocity about the center of the lid is zero. The zero average velocity implies that the forcing should not result in a single vortex, where the axis of the vortex is in the $x - z$ plane. The zero first moment implies that the forcing is not expected to drive a vortex whose axis is parallel to the y direction. Of particular interest with the bidirectional forcing is the ability of the system to maintain a circulation whose primary motion is parallel to the $x - z$ plane, despite the fact that the forcing is chosen to avoid this motion.

The basic parameters are the Reynolds number, $R_e = \frac{UL}{\nu}$, and two aspect ratios, $\gamma = \frac{H}{L}$ and $\lambda = \frac{D}{L}$. Both aspect ratios are chosen to be unity. In addition to these basic parameters,

the initial conditions must again be characterized in some manner. Two types of initial conditions are treated; The steady flow generated by unidirectional forcing on the top of the cavity (top forcing), shown in figure 5-2(a), and the steady flow generated by the unidirectional forcing of the side of the cavity (side forcing), shown in figure 5-2(b). The simulations that developed the initial conditions used a Reynolds number of 100, and a forcing mode number of unity. The magnitude of the initial conditions and asymmetrical behavior of the steady solutions are measured again with \underline{u} , now defined as a line integral along the centerline of the cavity, perpendicular to the forcing plane.

5.2 Results with symmetric unidirectional forcing

The symmetric unidirectional forcing is treated in the simulations starting from rest, and starting with both types of initial conditions in subsequent trials. The Reynolds number and the strength of the initial conditions was incremented in subsequent runs to attempt to induce a mode of motion analogous to the asymmetric steady flow in the two-dimensional case. Both aspect ratios were fixed at unity. However, for all cases considered, only one steady motion appeared. A three-dimensional analog of the asymmetric solution could not be found.

This result is surprising. The three dimensional case with symmetric unidirectional forcing is similar to the two dimensional case with $n = 2$. The only significant difference is the presence of endwalls. The two-dimensional cavity may be considered to be a three dimensional cavity whose third direction is infinite. The present three-dimensional cavity with aspect ratio of unity has the endwalls quite close. The close endwalls may suppress the second steady solution.

A promising direction for further study is to consider larger values of λ , effectively moving the endwalls further apart. Incrementing λ will eventually produce three-dimensional results that match the two-dimensional results. Unfortunately, this process also requires a linear increase in resolution. The three-dimensional results in the cube are already near the limit of the available computational resources, and hence this procedure could not be

pursued at this time.

Contour plots of u , v and w for a low Reynolds number case ($Re = 2$) are shown in figures 5-3 through 5-8. It can be seen in figures 5-3 through 5-8 that the flow is not symmetric about the centerline of the cavity for any slice along the z axis, despite the fact that the forcing is symmetric for such a slice. A perpendicular slice shown in 5-3(d), taken at $x = 0.5$ and as shown in figure 5-3 shows the presence of a weak but distinct primary vortex. It seems that the close proximity of the endwalls allows a weak tertiary flow to exist, balancing a pressure gradient that develops along the endwall. Note that the asymmetry is weak, and this steady flow is considered analogous to the symmetric flow of the two-dimensional simulations, not the asymmetric flow.

Note that figures 5-3 through 5-8 also show that the forcing develops primary vortices that only penetrate approximately one-third of the depth at the cavity center. These primary vortices then drive two secondary vortices, rotating in the opposite direction, in the bottom two-thirds of the cavity. A view from the top, figure 5-4(c) shows that this vortex motion is confined to a quadrant pattern.

Figures 5-9 through 5-14 show contour plots of u , v and w for a higher Reynolds number ($Re = 100$). It is apparent in figure 5-9(c) that the flow pattern looks closer to a symmetric pattern than the lower Reynolds number case, shown in figure 5-3(c). A tertiary flow still exists, as shown in the slice at $x = 0.5$ in figure 5-9(d), but this tertiary flow is now comprised of a nearly symmetric but much more complex motion than the low Reynolds number case in figure 5-3(d).

The view from the top, figure 5-10(c) shows that this motion has a much different pattern than the lower Reynolds number case, shown in figure 5-4(c). The motion now has a diagonal pattern. It is difficult to say whether this change in pattern is a sudden bifurcation to a new mode of steady motion, or a gradual change in the flow pattern. The value of \underline{u} for the final steady states over a range of Reynolds numbers is shown in figure 5-21(a), along with history of \underline{u} for various initial conditions, 5-21(b). This figure does not show a sudden transition to a new state, implying that the change in pattern is merely a

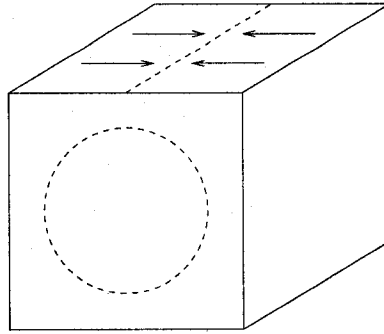
gradual change in flow pattern.

Figures 5-15 through 5-20 show contour plots of u , v and w for a Reynolds number of 1000. Note in figure 5-15(c) that the primary vortices are confined to a region very near the top, and larger counterrotating secondary vortices form near the bottom. However, the contour pattern in figure 5-15(c) is clearly symmetric, and this flow is still considered analogous to the symmetric two-dimensional mode. Also appearing in the flow is smaller scale motion, evident in figure 5-15(a) and (b) near the upper corners. Figure 5-16(c) shows that the diagonal aspect of the motion is still present, but has become more complicated. Figures 5-19 and 5-20 show that the flow is only marginally resolved, and wiggles in the solution have appeared.

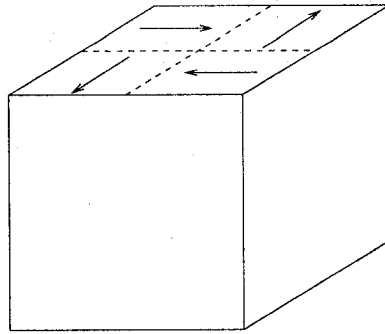
5.3 Results with bidirectional forcing

Reynolds numbers of 10, 100, and 1000 are considered. The results are shown in figures 5-22 through 5-24 for R_e of 10, figures 5-25 through 5-27 for R_e of 100, and figures 5-28 through 5-30 for R_e of 1000. Note again that wiggles appear in the solution for R_e of 1000, implying a need for increased resolution.

The steady flows shown in the figures is the only steady flow that appeared in the simulations for all initial conditions. At no time did a second steady flow appear. The figures show the same type of motion as the previous case, including a primary set of vortices near the top, with weaker secondary counterrotating vortices beneath. A strong asymmetric flow occupying the entire domain does not appear.

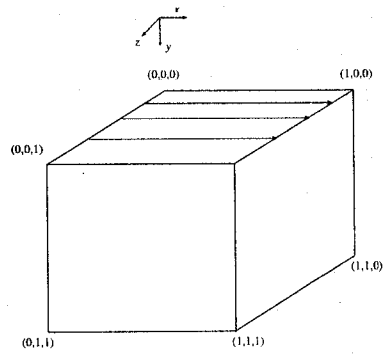


(a)

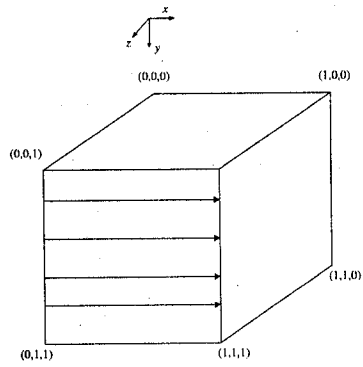


(b)

Figure 5-1: (a) Symmetric forcing function (b) Bidirectional forcing function

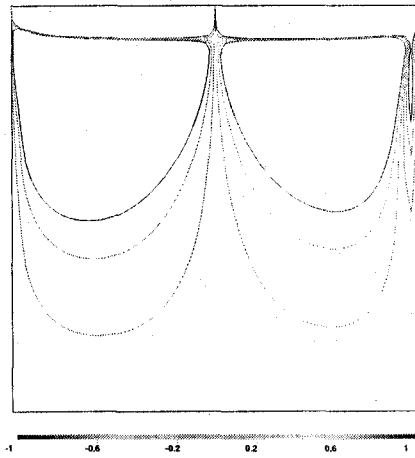


(a)

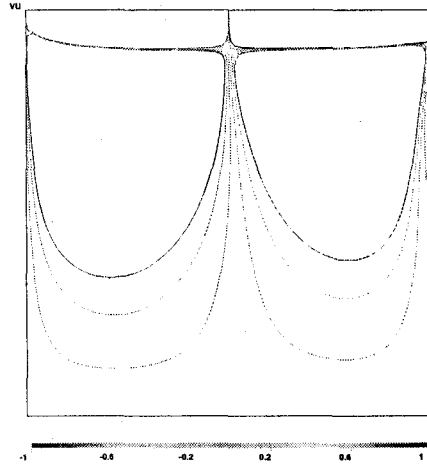


(b)

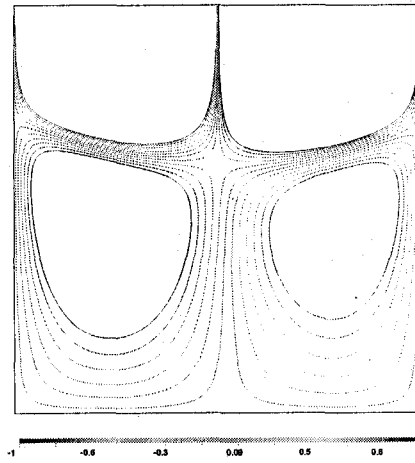
Figure 5-2: (a) and (b) Initial conditions for 3D case



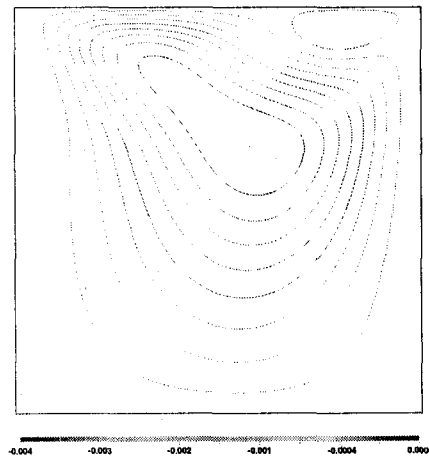
(a) $z = 0.1$



(b) $z = 0.9$

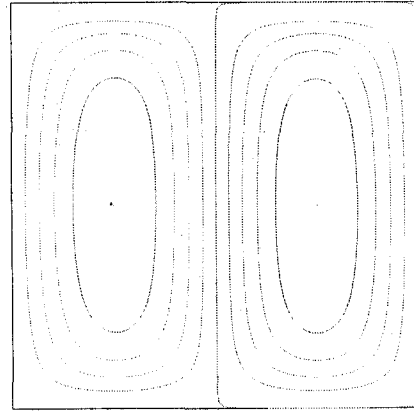


(c) $z = 0.5$

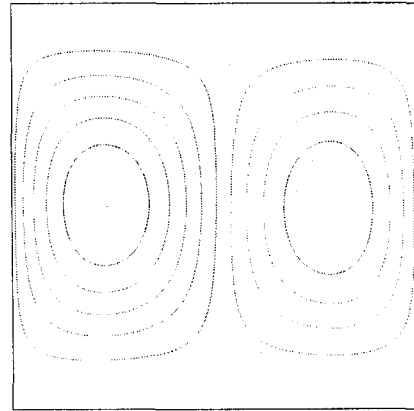


(d) $x = 0.5$

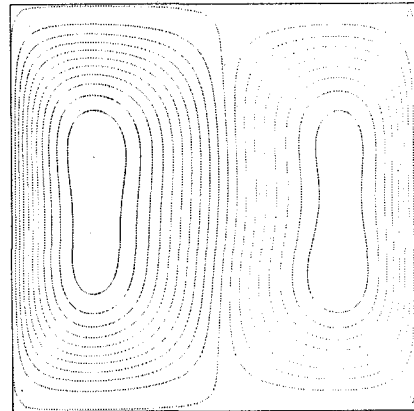
Figure 5-3: Horizontal velocity contour u for symmetric forcing, $Re = 2$.



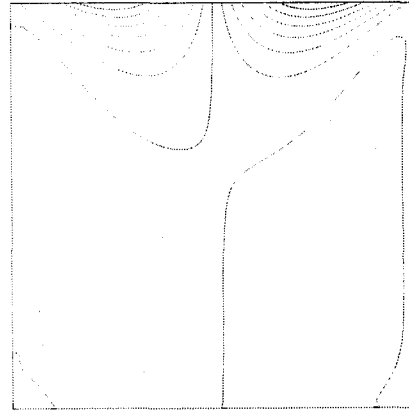
(a) $y = 0.1$



(b) $y = 0.9$

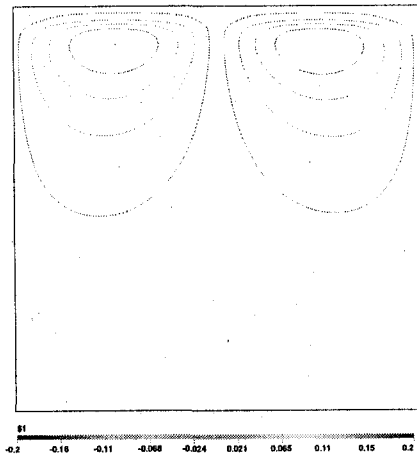


(c) $y = 0.5$

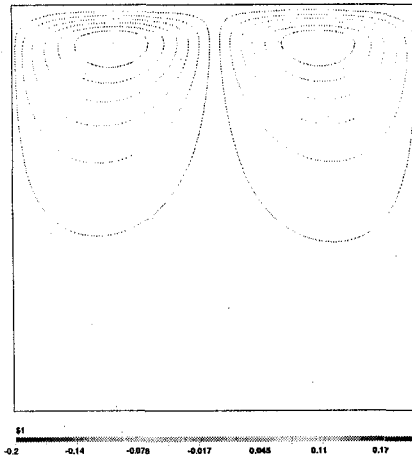


(d) diagonal

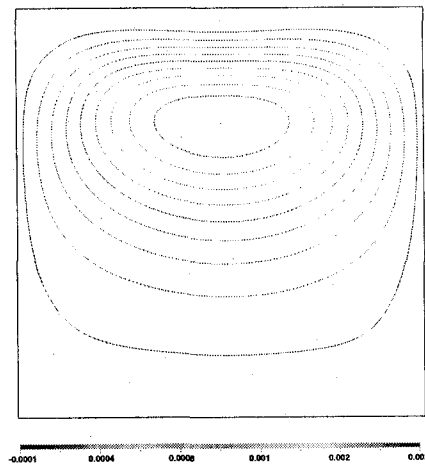
Figure 5-4: Horizontal velocity contour u for symmetric forcing, $Re = 2$.



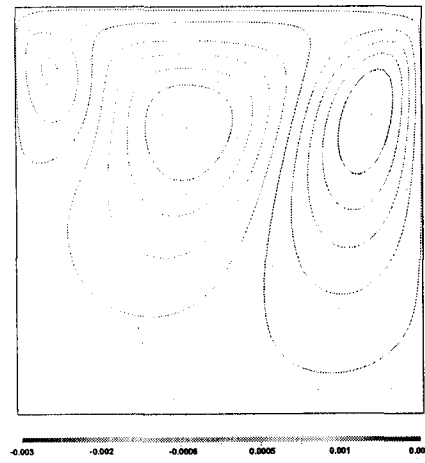
(a) $z = 0.1$



(b) $z = 0.9$

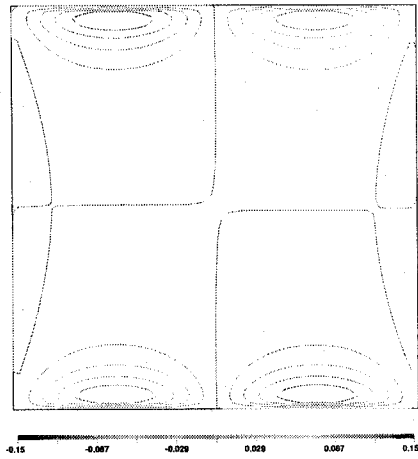


(c) $z = 0.5$

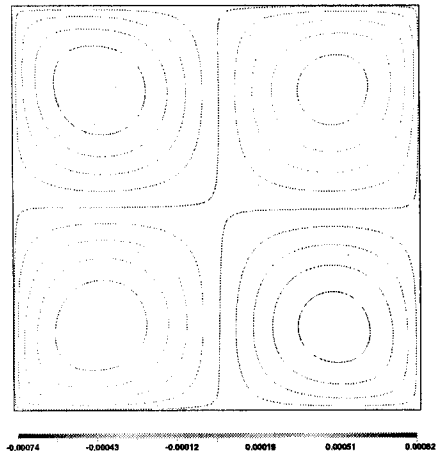


(d) $x = 0.5$

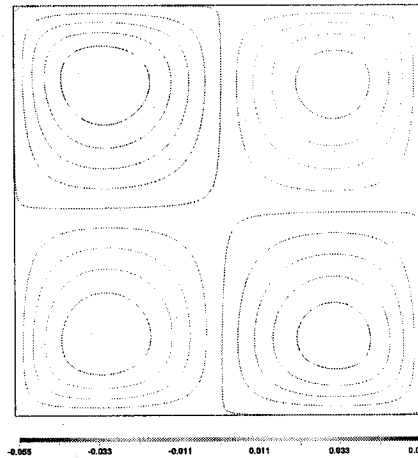
Figure 5-5: Vertical velocity contour v for symmetric forcing, $Re = 2$.



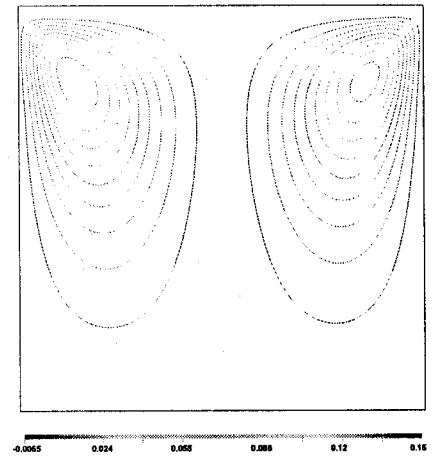
(a) $y = 0.1$



(b) $y = 0.9$

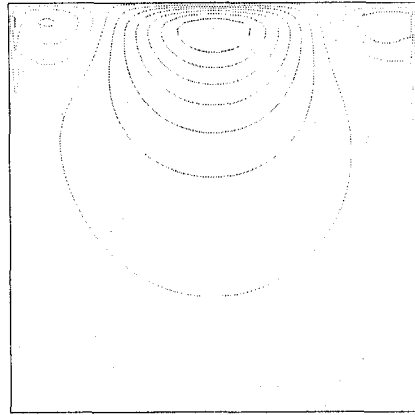


(c) $y = 0.5$

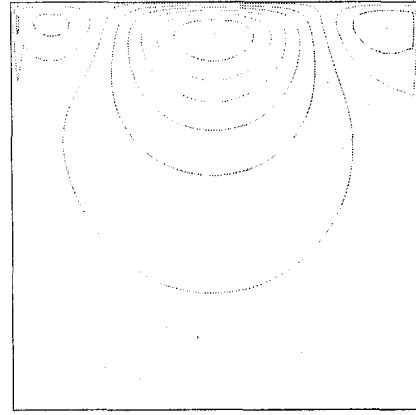


(d) diagonal

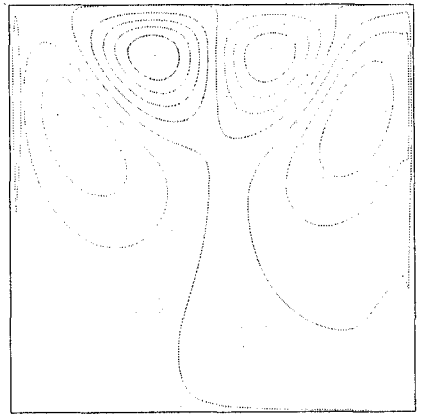
Figure 5-6: Vertical velocity contour v for symmetric forcing, $Re = 2$.



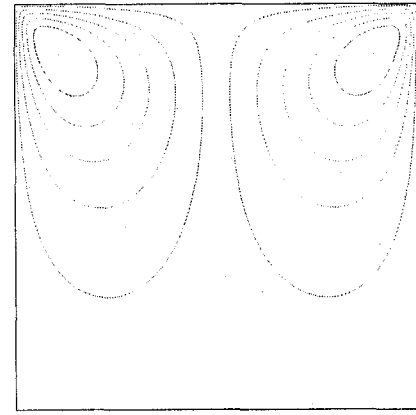
(a) $z = 0.1$



(b) $z = 0.9$

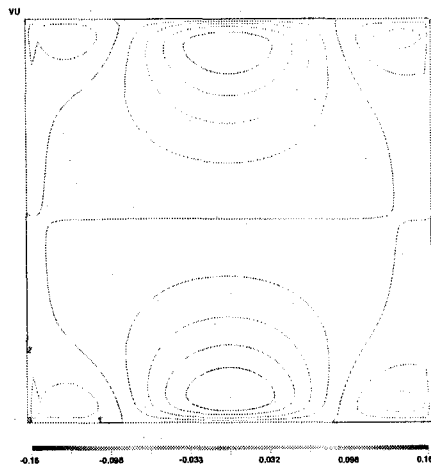


(c) $z = 0.5$

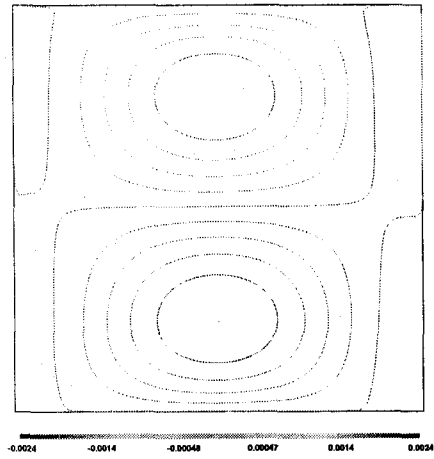


(d) $x = 0.5$

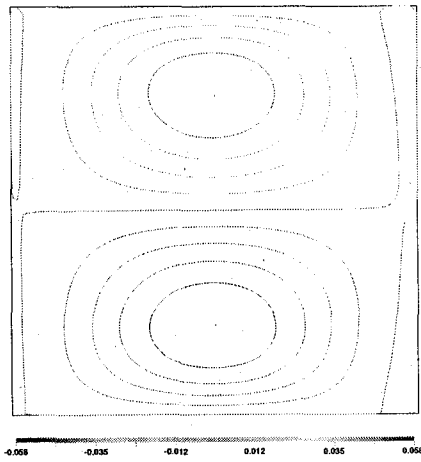
Figure 5-7: Transverse velocity contour w for symmetric forcing, $Re = 2$.



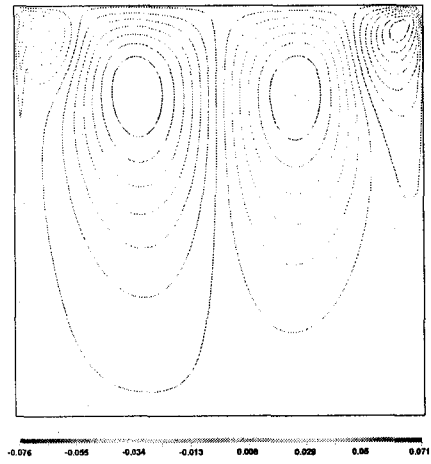
(a) $y = 0.1$



(b) $y = 0.9$

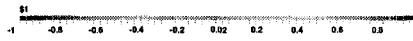
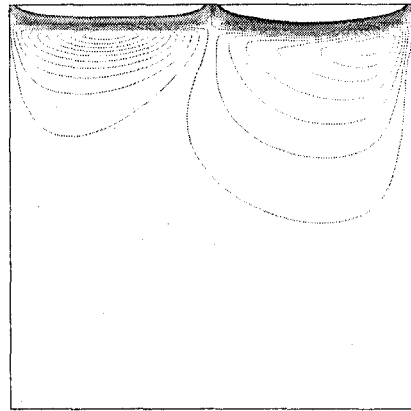


(c) $y = 0.5$

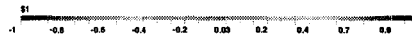
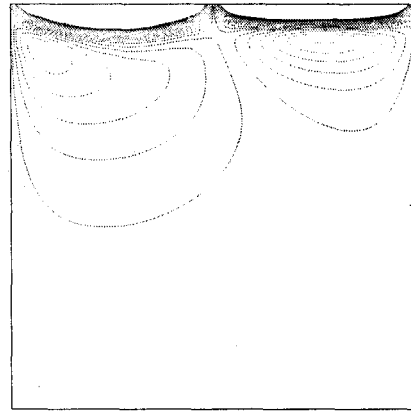


(d) diagonal

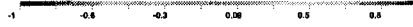
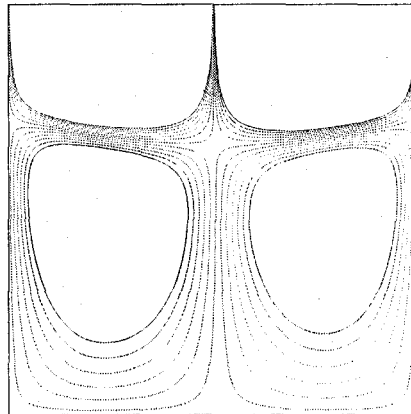
Figure 5-8: Transverse velocity contour w for symmetric forcing, $Re = 2$.



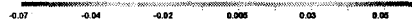
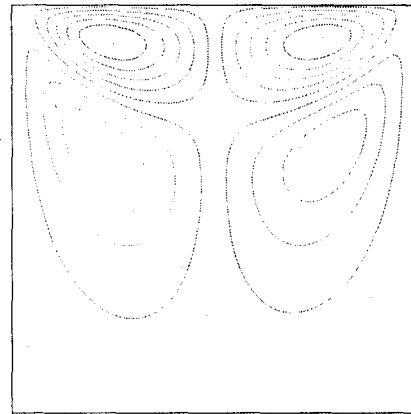
(a) $z = 0.1$



(b) $z = 0.9$

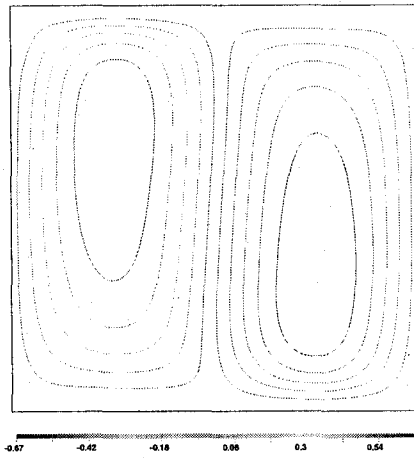


(c) $z = 0.5$

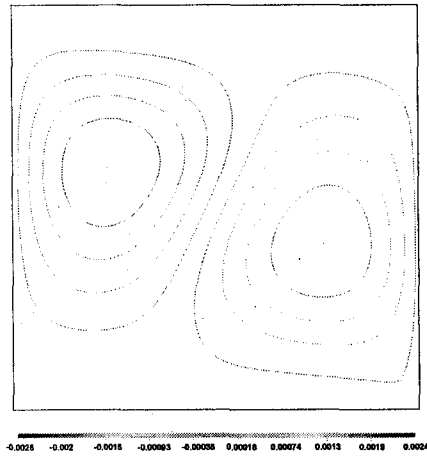


(d) $x = 0.5$

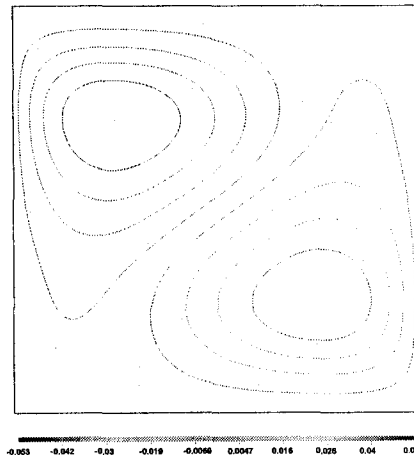
Figure 5-9: Horizontal velocity contour u for symmetric forcing, $Re = 100$.



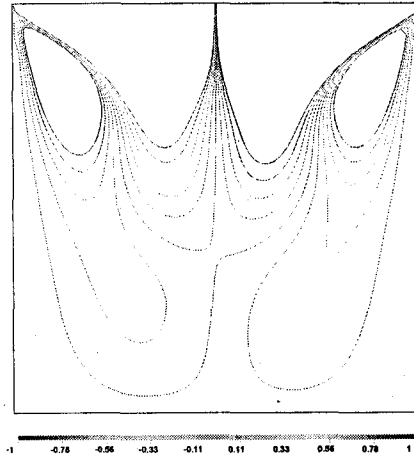
(a) $y = 0.1$



(b) $y = 0.9$

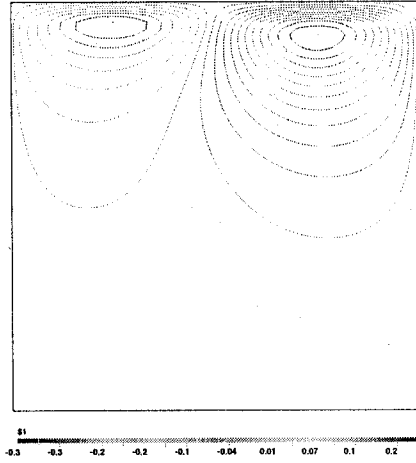


(c) $y = 0.5$

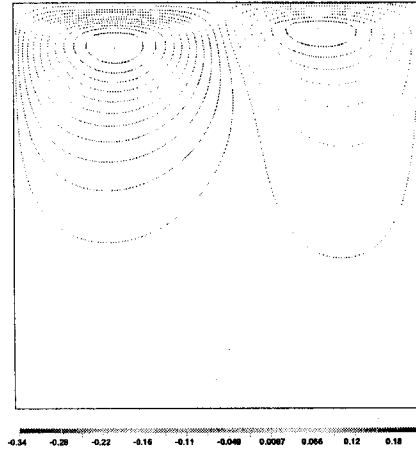


(d) diagonal

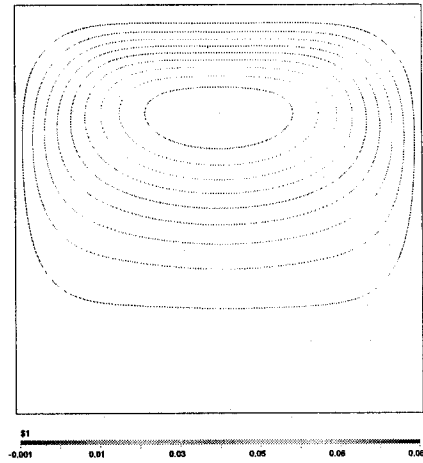
Figure 5-10: Horizontal velocity contour u for symmetric forcing, $Re = 100$.



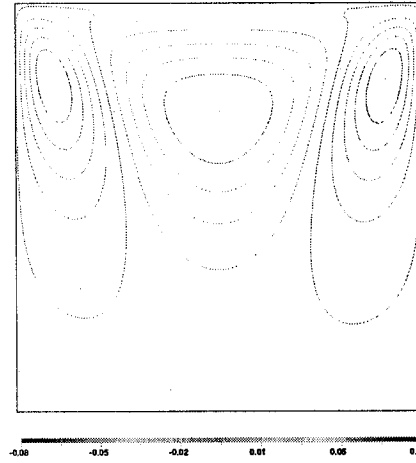
(a) $z = 0.1$



(b) $z = 0.9$

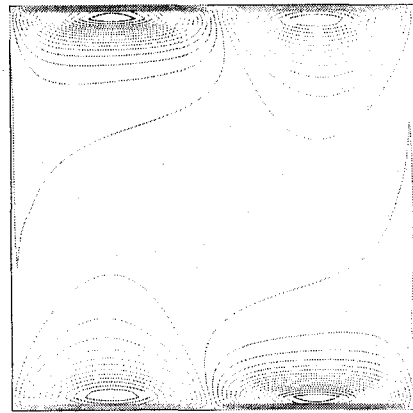


(c) $z = 0.5$

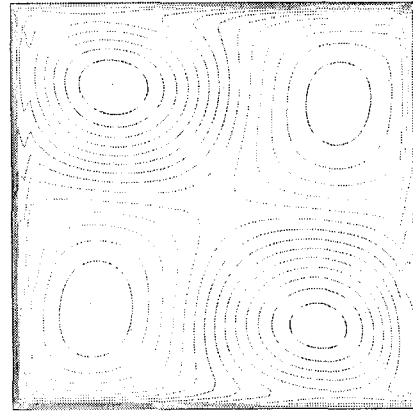


(d) $x = 0.5$

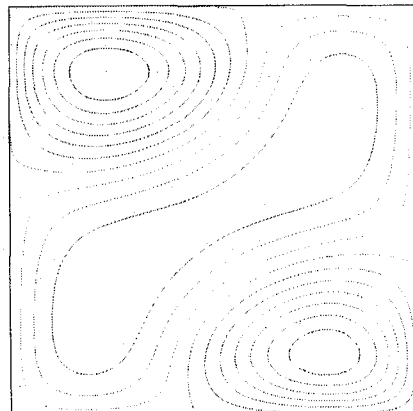
Figure 5-11: Vertical velocity contour v for symmetric forcing, $Re = 100$.



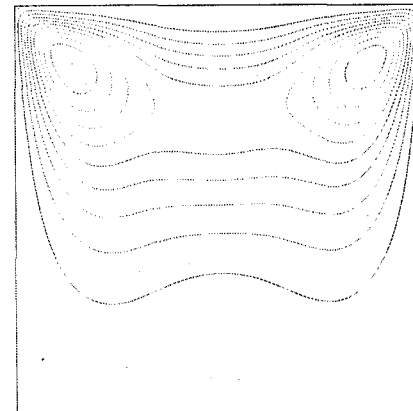
(a) $y = 0.1$



(b) $y = 0.9$

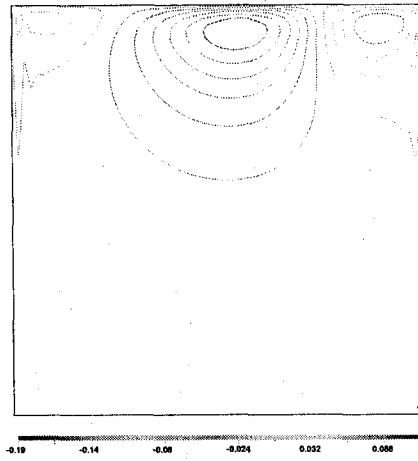


(c) $y = 0.5$

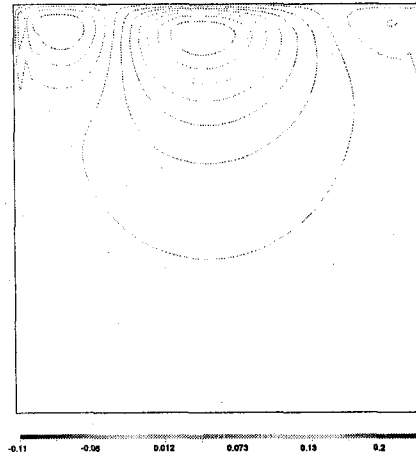


(d) diagonal

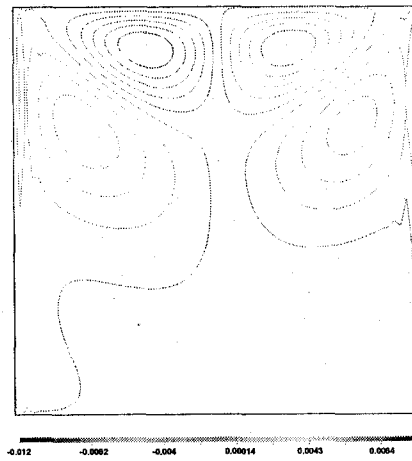
Figure 5-12: Vertical velocity contour v for symmetric forcing, $Re = 100$.



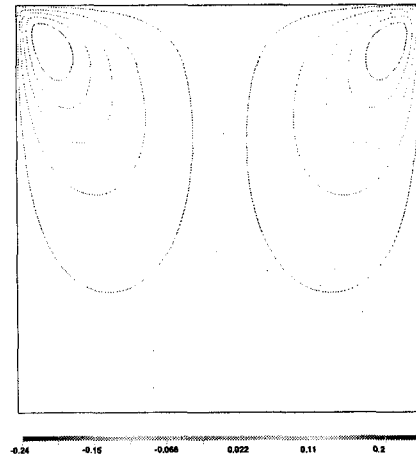
(a) $z = 0.1$



(b) $z = 0.9$

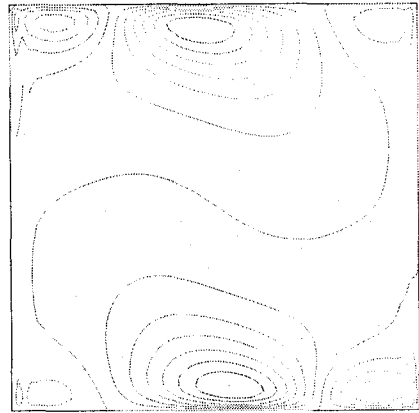


(c) $z = 0.5$



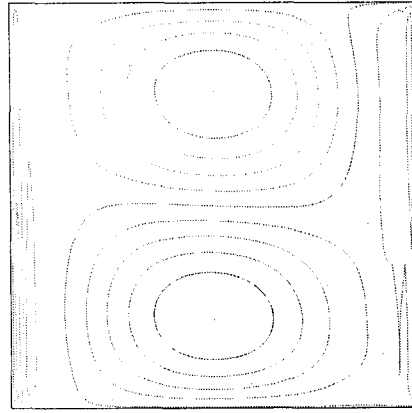
(d) $x = 0.5$

Figure 5-13: Transverse velocity contour w for symmetric forcing, $Re = 100$.



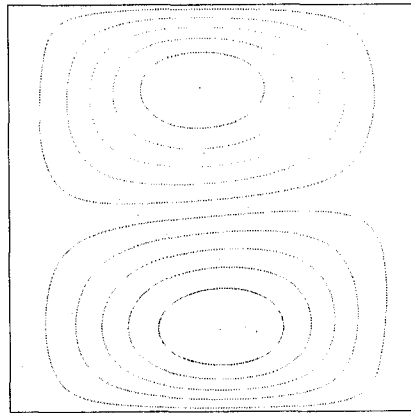
-0.212 -0.151 -0.0907 -0.0303 0.0301 0.0905 0.151 0.211

(a) $y = 0.1$



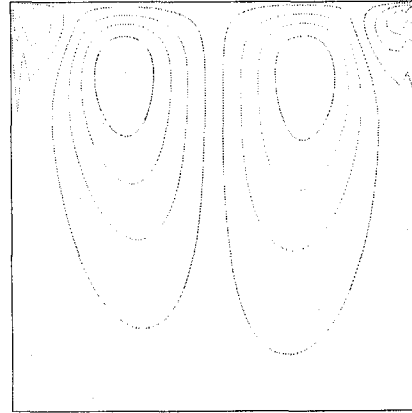
-0.0027 -0.0016 -0.0005 0.0005 0.0015 0.0025

(b) $y = 0.9$



-0.068 -0.037 -0.016 0.003 0.025 0.047

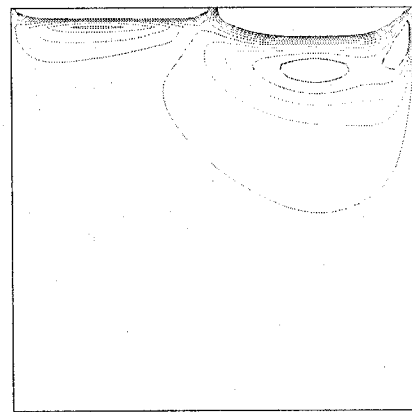
(c) $y = 0.5$



-0.060 -0.030 -0.024 -0.009 0.0056 0.02 0.035 0.05 0.064

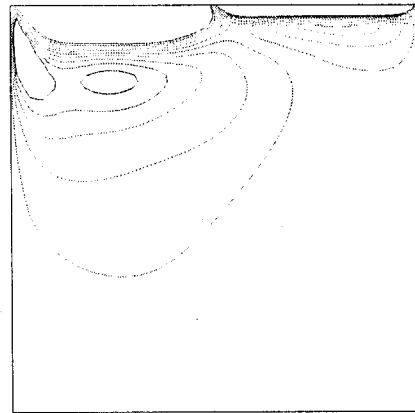
(d) diagonal

Figure 5-14: Transverse velocity contour w for symmetric forcing, $Re = 100$.



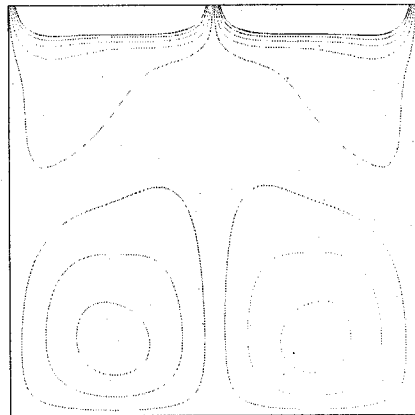
-1 -0.78 -0.56 -0.33 -0.11 0.11 0.33 0.56 0.78 1

(a) $z = 0.1$



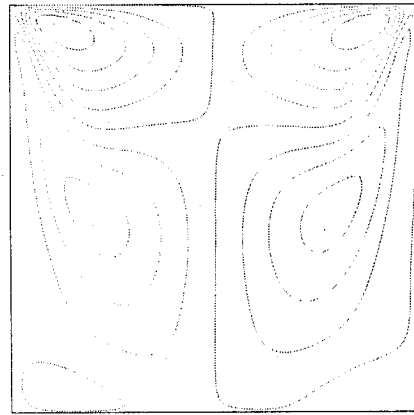
-1 -0.78 -0.56 -0.33 -0.11 0.11 0.33 0.56 0.78 1

(b) $z = 0.9$



-1 -0.78 -0.56 -0.33 -0.11 0.11 0.33 0.56 0.78 1

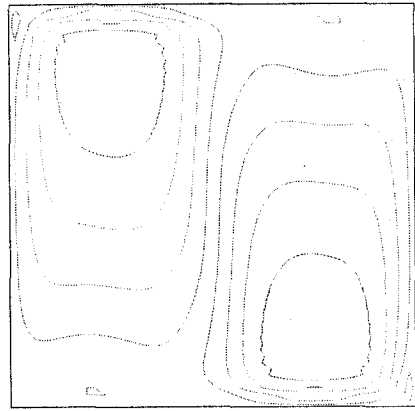
(c) $z = 0.5$



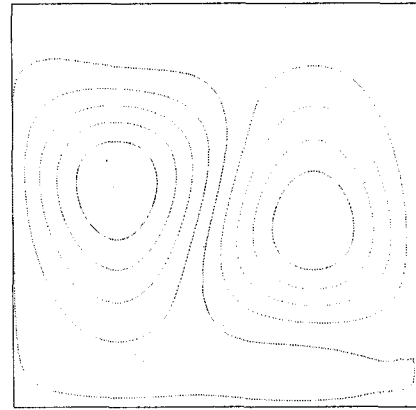
-0.0771 -0.0464 -0.0157 0.015 0.0457 0.0764

(d) $x = 0.5$

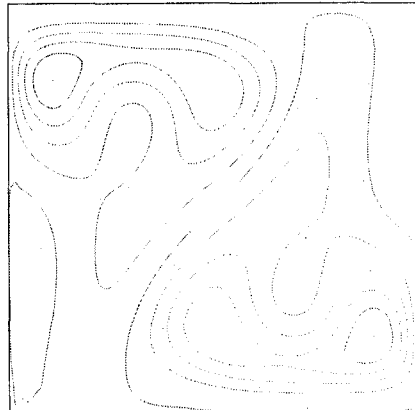
Figure 5-15: Horizontal velocity contour u for symmetric forcing, $Re = 1000$.



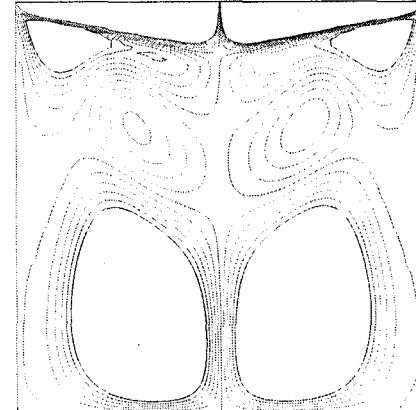
(a) $y = 0.1$



(b) $y = 0.9$

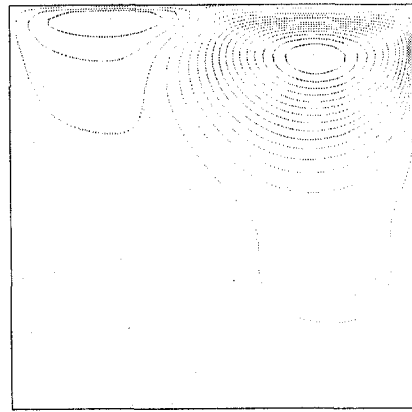


(c) $y = 0.5$



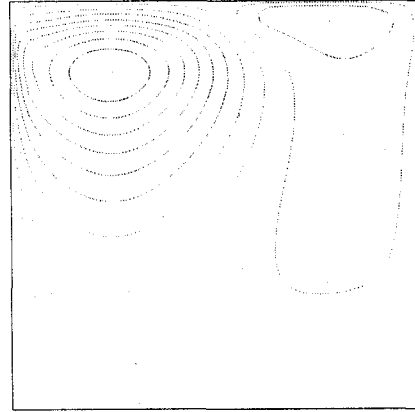
(d) diagonal

Figure 5-16: Horizontal velocity contour u for symmetric forcing, $Re = 1000$.



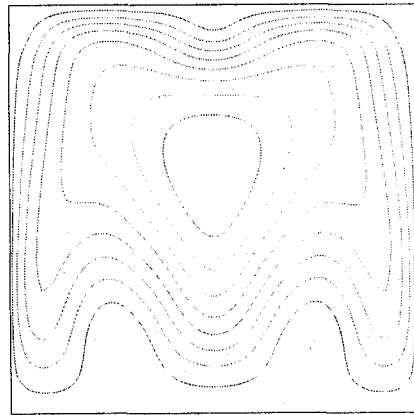
-0.4 -0.3 -0.2 -0.1 -0.05 -0.02 0.02 0.06

(a) $z = 0.1$



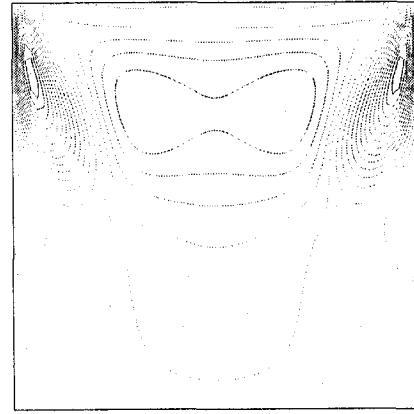
-0.35 -0.27 -0.19 -0.11 -0.02 0.06

(b) $z = 0.9$



-0.0045 0.0038 0.012 0.02 0.029 0.037 0.045 0.054 0.062 0.07

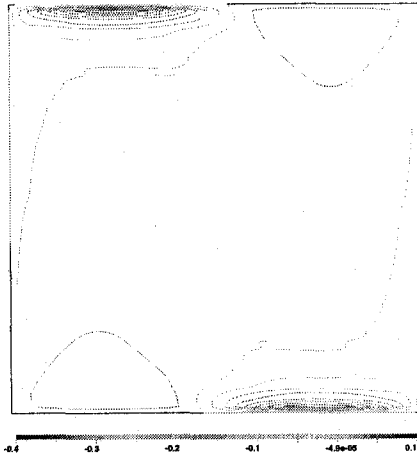
(c) $z = 0.5$



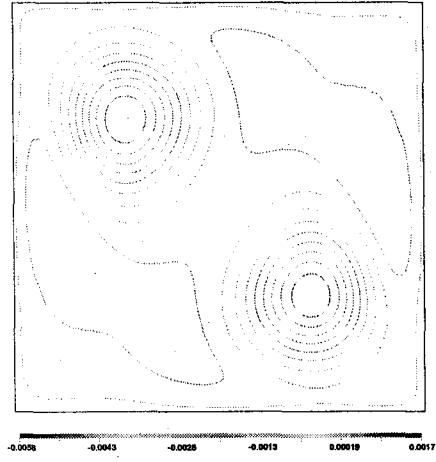
0.1 -0.1 -0.1 -0.08 -0.06 -0.04 -0.02 0.0004 0.02 0.01

(d) $x = 0.5$

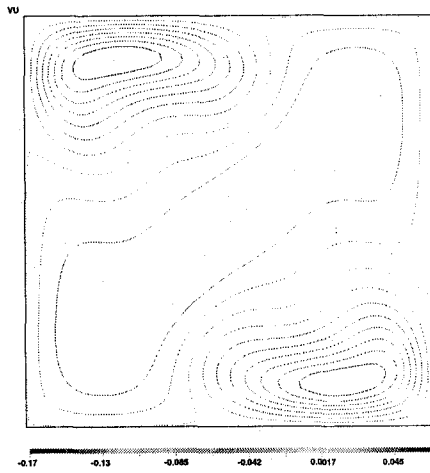
Figure 5-17: Vertical velocity contour v for symmetric forcing, $Re = 1000$.



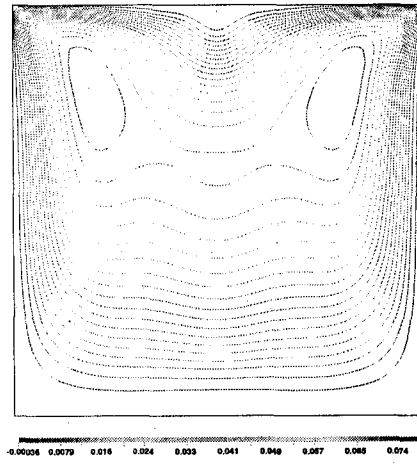
(a) $y = 0.1$



(b) $y = 0.9$

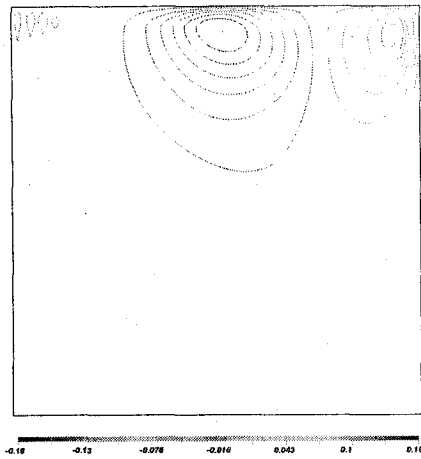


(c) $y = 0.5$

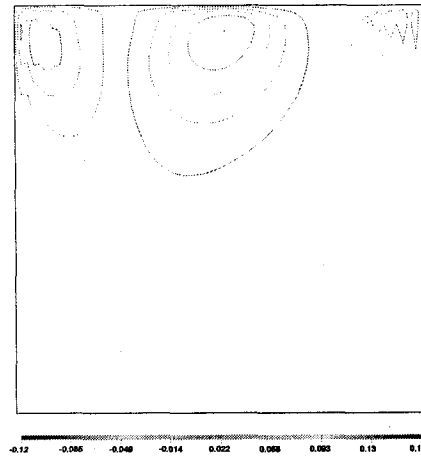


(d) diagonal

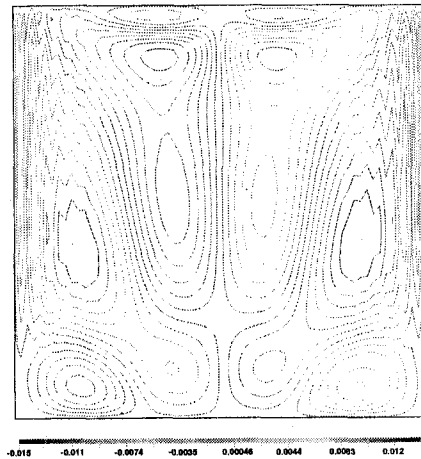
Figure 5-18: Vertical velocity contour v for symmetric forcing, $Re = 1000$.



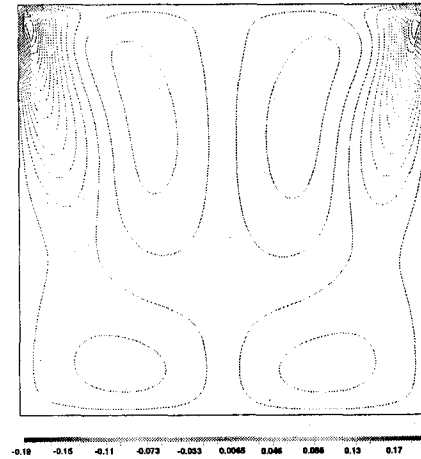
(a) $z = 0.1$



(b) $z = 0.9$

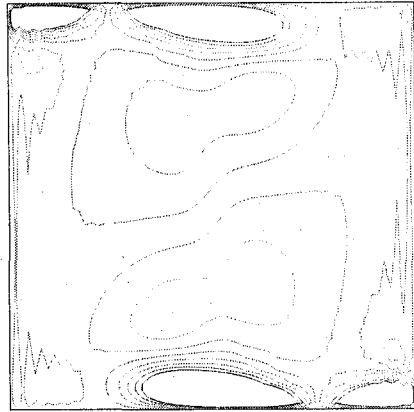


(c) $z = 0.5$

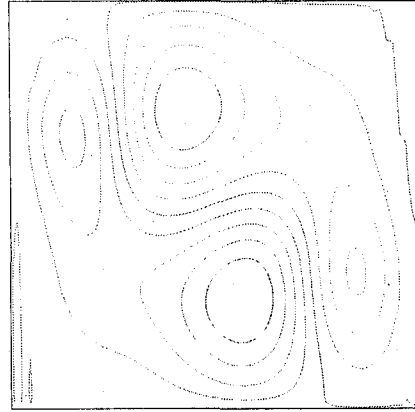


(d) $x = 0.5$

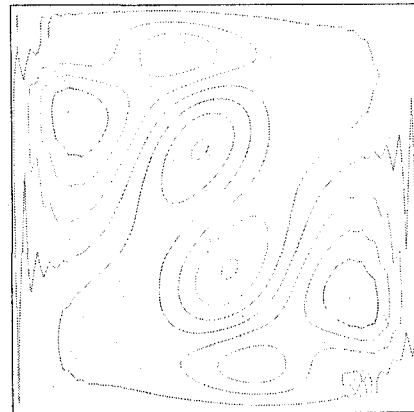
Figure 5-19: Transverse velocity contour w for symmetric forcing, $Re = 1000$.



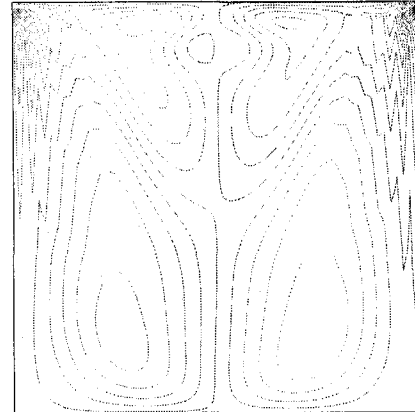
(a) $y = 0.1$



(b) $y = 0.9$

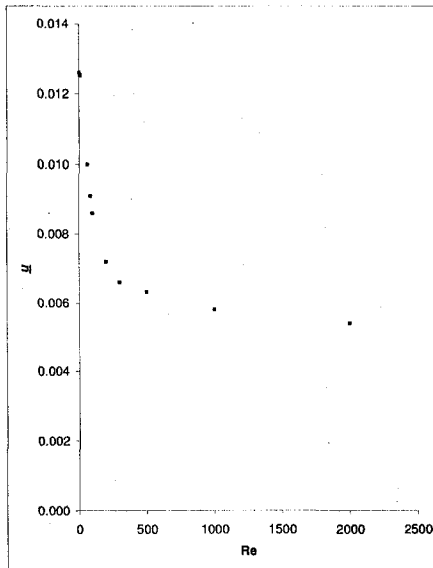


(c) $y = 0.5$

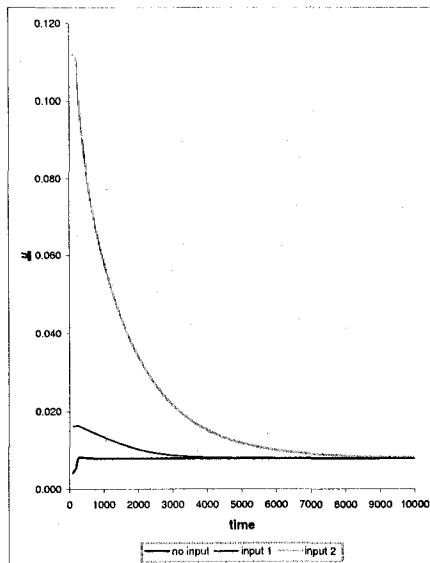


(d) diagonal

Figure 5-20: Transverse velocity contour w for symmetric forcing, $Re = 1000$.

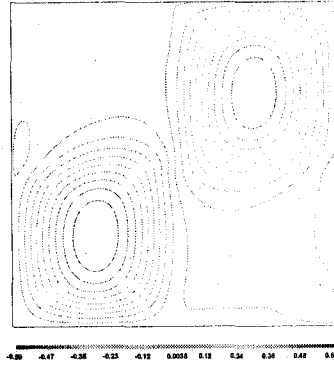


(a)

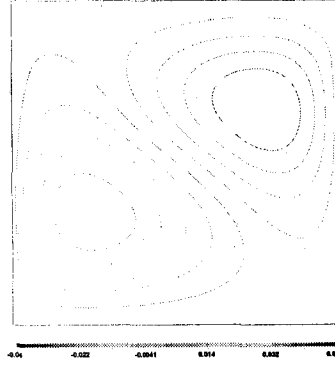


(b)

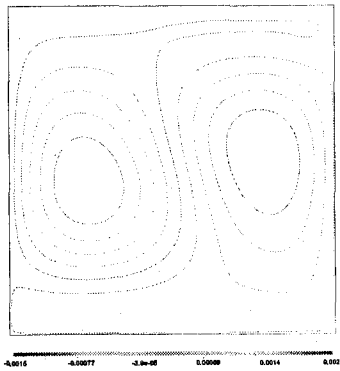
Figure 5-21: 3D symmetric forcing function (a) Steady state solution (b) Time history of \underline{u} for various initial conditions, $Re = 100$



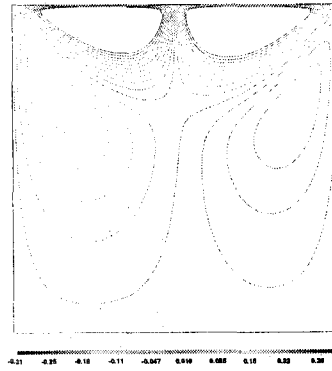
(a) $y = 0.1$



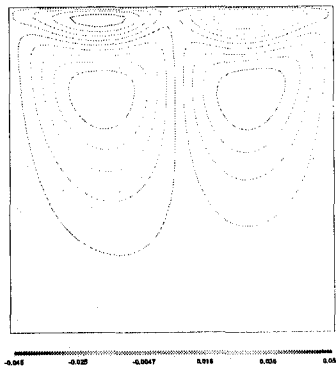
(b) $y = 0.5$



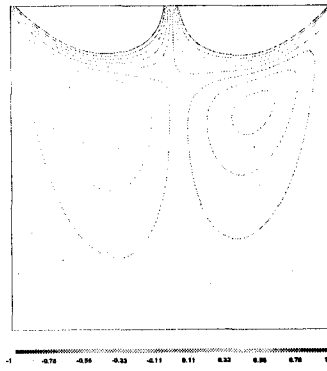
(c) $y = 0.9$



(d) $z = 0.5$

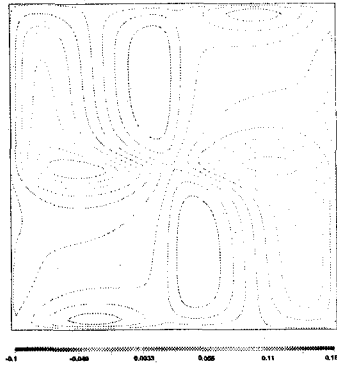


(e) $x = 0.5$

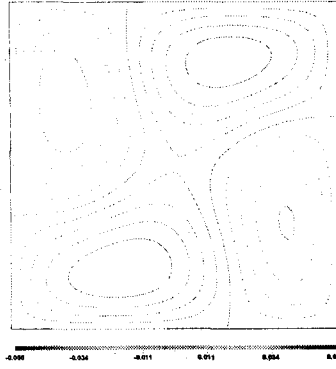


(f) diagonal

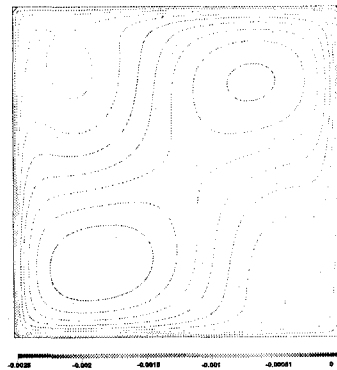
Figure 5-22: Horizontal velocity contour u for bi-directional forcing function, $Re = 10$.



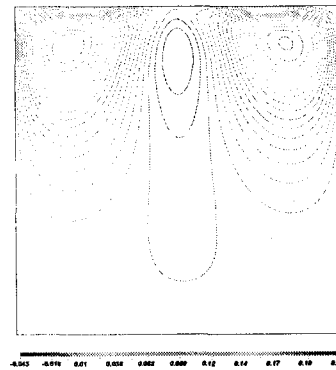
(a) $y = 0.1$



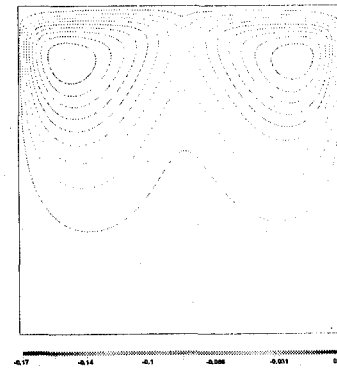
(b) $y = 0.5$



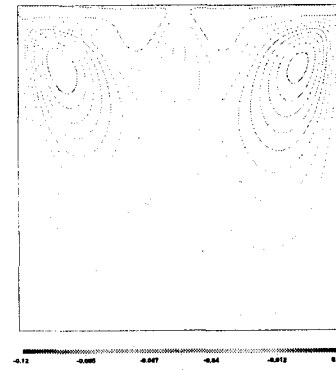
(c) $y = 0.9$



(d) $z = 0.5$

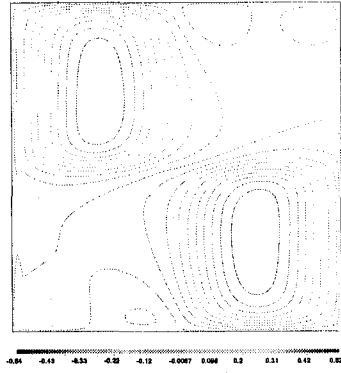


(e) $x = 0.5$

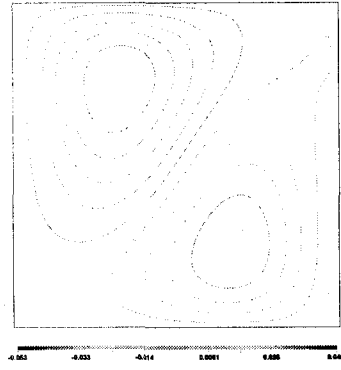


(f) diagonal

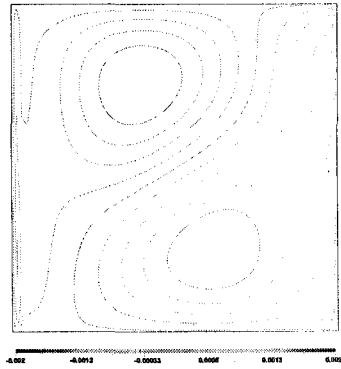
Figure 5-23: Vertical velocity contour v for bi-directional forcing function, $Re = 10$.



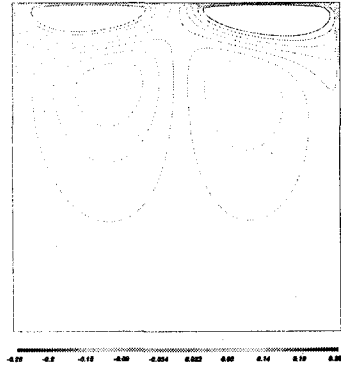
(a) $y = 0.1$



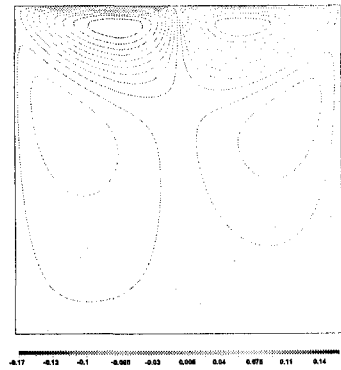
(b) $y = 0.5$



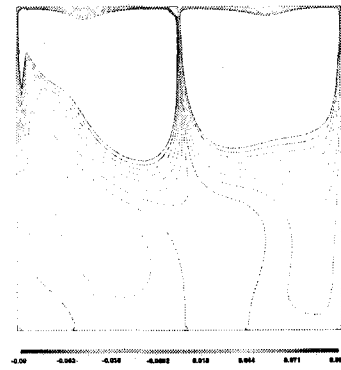
(c) $y = 0.9$



(d) $z = 0.5$

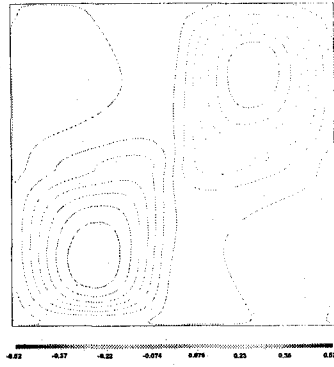


(e) $x = 0.5$

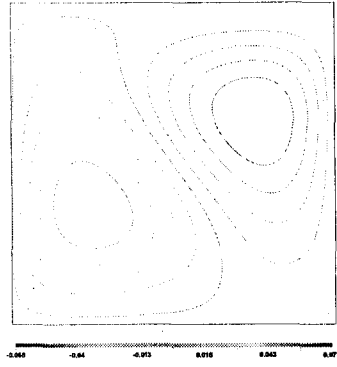


(f) diagonal

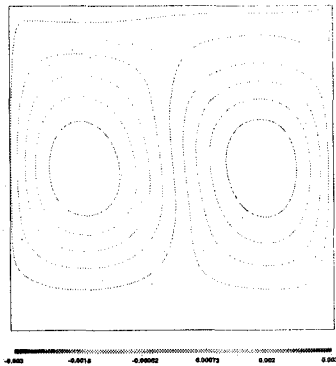
Figure 5-24: Transverse velocity contour w for bi-directional forcing function, $Re = 10$.



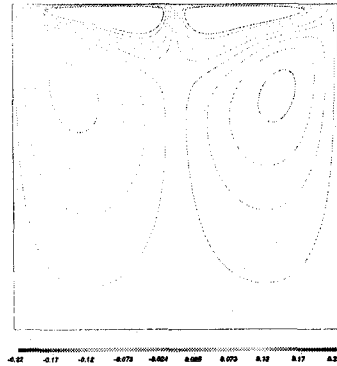
(a) $y = 0.1$



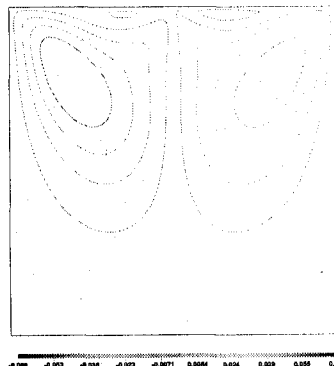
(b) $y = 0.5$



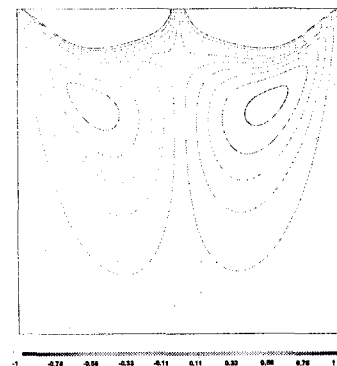
(c) $y = 0.9$



(d) $z = 0.5$

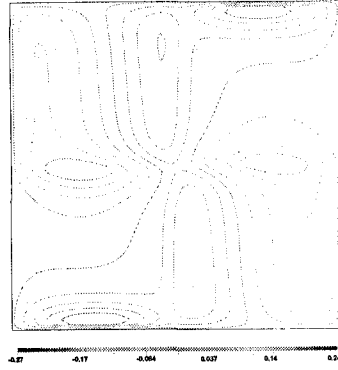


(e) $x = 0.5$

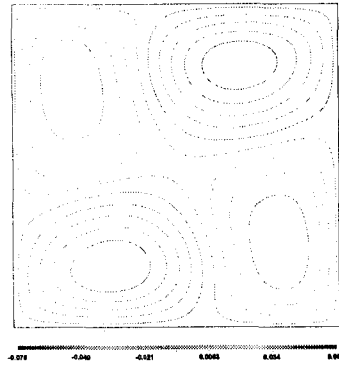


(f) diagonal

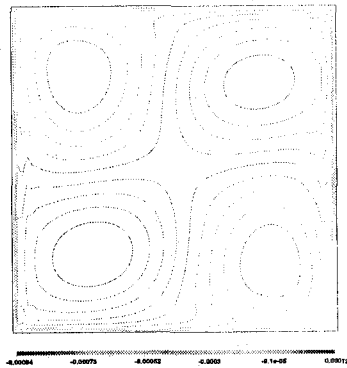
Figure 5-25: Horizontal velocity contour u for bi-directional forcing function, $Re = 100$.



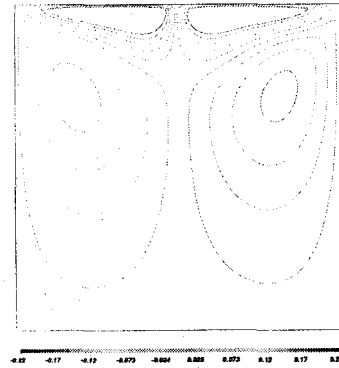
(a) $y = 0.1$



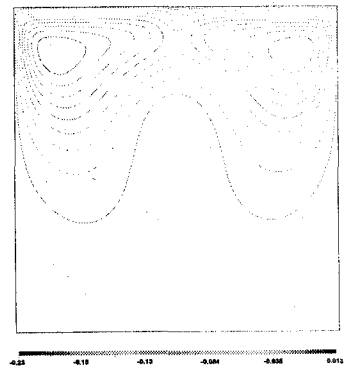
(b) $y = 0.5$



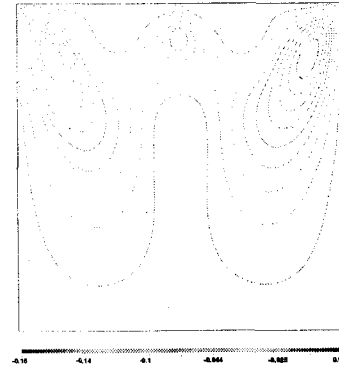
(c) $y = 0.9$



(d) $z = 0.5$

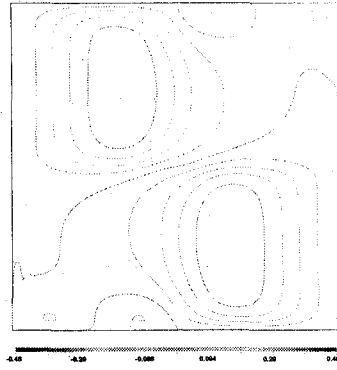


(e) $x = 0.5$

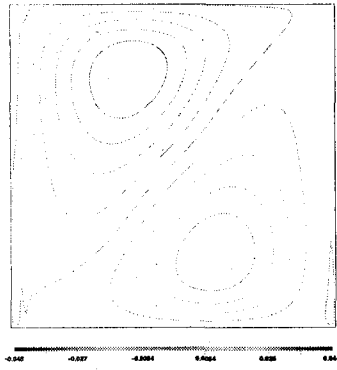


(f) diagonal

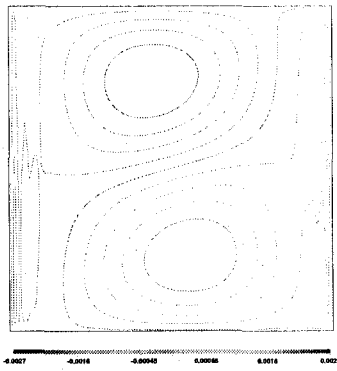
Figure 5-26: Vertical velocity contour v for bi-directional forcing function, $Re = 100$.



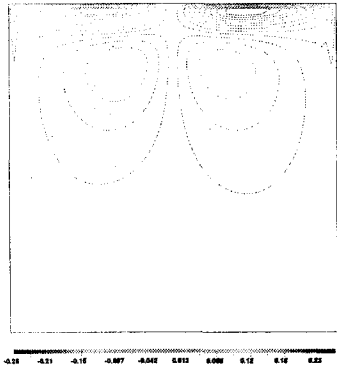
(a) $y = 0.1$



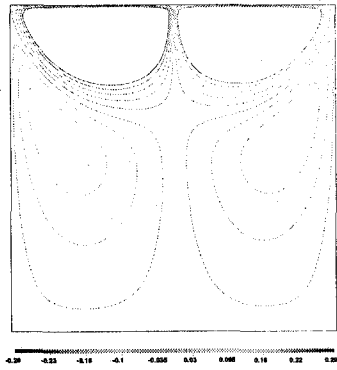
(b) $y = 0.5$



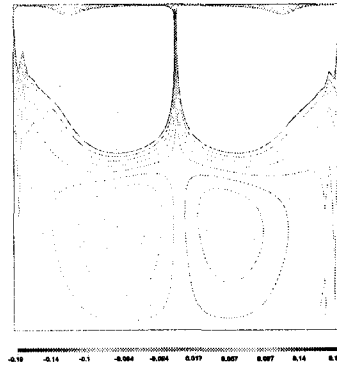
(c) $y = 0.9$



(d) $z = 0.5$

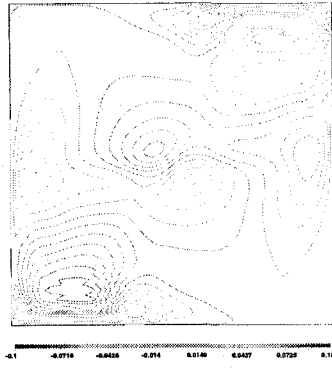


(e) $x = 0.5$

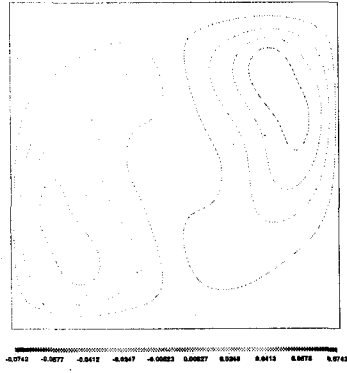


(f) diagonal

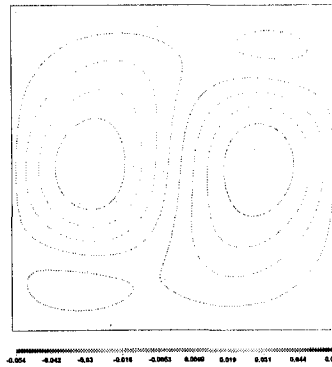
Figure 5-27: Transverse velocity contour w for bi-directional forcing function, $Re = 100$.



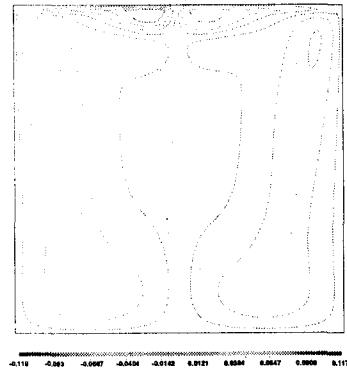
(a) $y = 0.1$



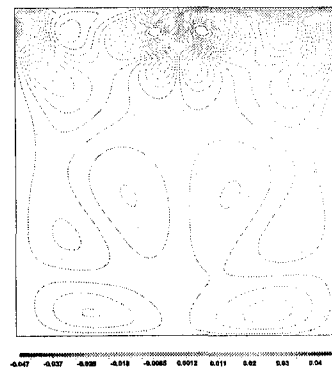
(b) $y = 0.5$



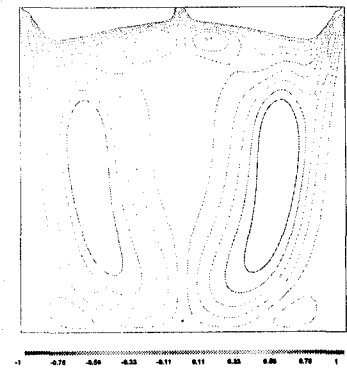
(c) $y = 0.9$



(d) $z = 0.5$

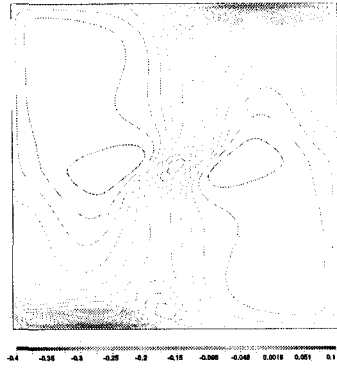


(e) $x = 0.5$



(f) diagonal

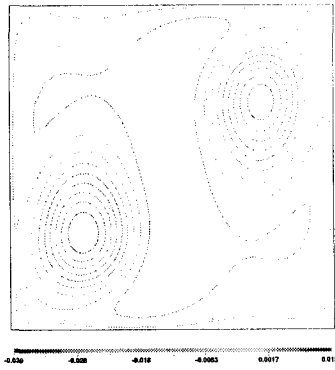
Figure 5-28: Horizontal velocity contour u for bi-directional forcing function, $Re = 1000$.



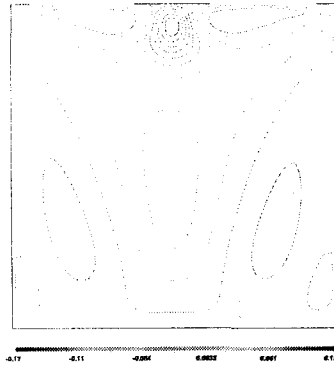
(a) $y = 0.1$



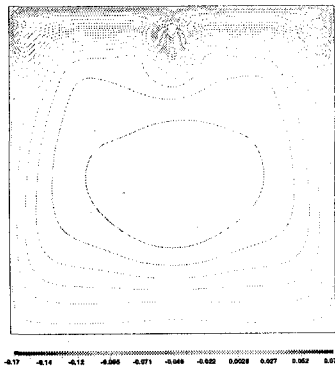
(b) $y = 0.5$



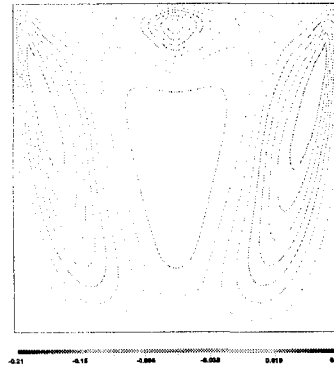
(c) $y = 0.9$



(d) $z = 0.5$

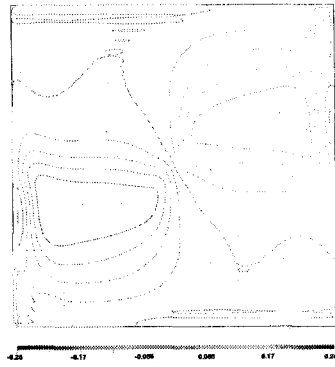


(e) $x = 0.5$



(f) diagonal

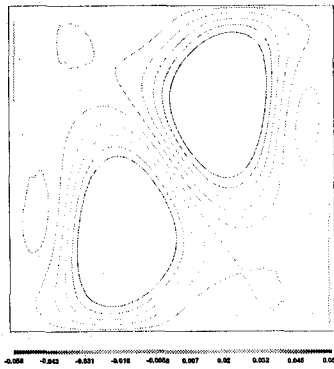
Figure 5-29: Vertical velocity contour v for bi-directional forcing function, $Re = 1000$.



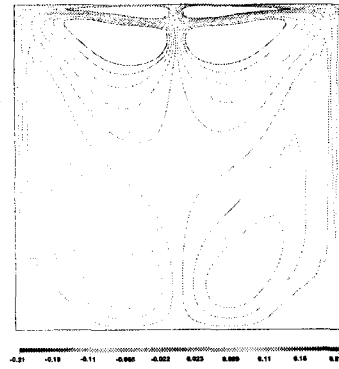
(a) $y = 0.1$



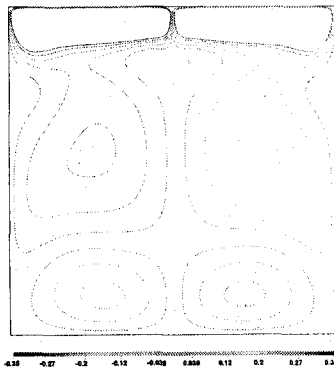
(b) $y = 0.5$



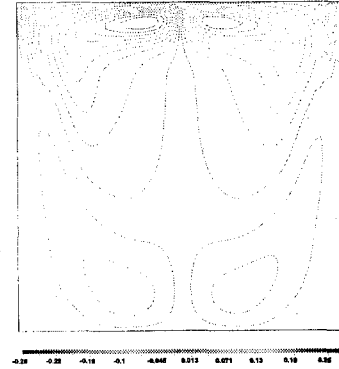
(c) $y = 0.9$



(d) $z = 0.5$



(e) $x = 0.5$



(f) diagonal

Figure 5-30: Transverse velocity contour w for bi-directional forcing function, $Re = 1000$.

Chapter 6

Conclusions

6.1 Discussion

It is readily apparent in chapter 4 that as the forcing mode number, n , increases, the forcing becomes more local to the top. The resulting flow has a strong component near the top, resulting in a boundary layer flow that is different from the flow in the bottom part of the cavity. The boundary layer flow has a horizontal length scale that matches the horizontal length scale of the forcing. However, the length scale of the flow in the bottom of the chamber is different. The bottom flow behavior seems to be unrelated to the length scale of the forcing. This is most readily apparent by comparing the streamlines pattern $n = 1$ and $n = 16$, cases for $\gamma = \frac{1}{2}$ (see figure 4-3 and 4-22(b)). The flow in the bottom of the chamber for these two cases is nearly the same, while the top forcing is dramatically different. The scale of this bottom flow appears to be related only to the size, and presumably the shape, of the chamber. All cases consistently point to this conclusion.

Despite the simple geometry of the driven cavity, this conclusion provides insight into the behavior of flow in the surface driven lakes, discussed in the introduction. Based on the results of the simulations, the global flow in the bottom region of a lake may be independent of the complicated forcing on the surface. The presence of a topographical feature near the edge of the lake may not have any significant influence on the global lake flow. Drastic changes in the surrounding topography are not guaranteed to change the overall flow pattern significantly. Furthermore, the flow lake patterns in the bottom region do not reflect the flow at the surface.

Another feature of the simulations is that the magnitude of the forcing is important, and can be chosen to be weak, leading to steady symmetric behaviour, or strong, leading to unsteady behavior. This fact is true for any pattern of vortices. In the papermaking application, this result implies that a complicated pattern of vortices may not be necessary to induce mixing, but the magnitude of the vortices must be large to avoid a steady vortex in the draining process, leading to streaks in the final product.

The Reynolds numbers considered in the simulations are quite small. Strictly speaking, these Reynolds numbers only apply to very slow experiments, very small experiments, or very viscous fluids. For example, a Reynolds number of 1000 would correspond to a square cavity of 10 centimeters with an imposed velocity of only 1 cm per second. Such an experiment is easily achieved in a laboratory experiment, but Reynolds numbers in geophysical flow and many industrial flows are many orders of magnitude larger. For these large Reynolds number flows, the direct effect of viscosity becomes unimportant. However, damping is still present due to the creation of turbulence. The results here suggest that similar results exist for these large Reynolds number flows, where the effect of viscosity has been replaced with the effect of turbulence. However, the precise behavior of higher Reynolds number flow remains to be determined.

6.2 Specific conclusions

The following general conclusions may be drawn:

1. The traditional driven cavity with $\gamma = 1$ and $\gamma = \frac{1}{2}$, for all initial conditions, yield only one steady flow patterns.
2. Steady symmetric flow patterns are present in all two dimensional cases with symmetric forcing.
3. Steady asymmetric flow patterns are also present in all two-dimensional cases except for the case of $u(x) = \sin(8\pi x)$ for $\gamma = \frac{1}{2}$.

4. Steady asymmetric flow patterns exhibit a large scale flow in the bottom of the domain.
5. In general, higher Reynolds numbers yield unsteady solutions. Although for most cases, this phenomenon is observed at very high Reynolds numbers, unsteady behavior can be observed at Reynolds numbers as low as 900.
6. Three dimensional symmetric flow forcing yields no asymmetric flow pattern for Reynolds number up to 1000 in a cube. Flow begins with weak asymmetry and slowly evolves to more symmetric flow behavior.
7. Bidirectional forcing function show symmetric flow behavior for Reynolds number up to 1000 in a cube.

Bibliography

- [1] G. Karniadakis, M. Israeli, and S. Orszag, "High-order splitting methods for the incompressible Navier-Stokes equations," *Journal of Computational Physics*, **97**, pp. 414-443, 1991.
- [2] J. C. Tannehill, D. A. Anderson, R. H. Pletcher, "Computational fluid mechanics and heat transfer," Taylor and Francis Publishers, 1997.
- [3] U. Ghia, K.N. Ghia and C.T. Shin, "High-Re Solutions for Incompressible Flow Using the Navier-Stokes Equations and a Multigrid Method" *Journal of Computational Physics*, **48**, pp. 387-411, 1982
- [4] Jason E. Farias and John P. McHugh, "The symmetric driven cavity," *Physics of fluids*, **Vol 14(9)**, pp. 3179-3188, September 2002.
- [5] Ramiro H. Bravo, "Development of the Three-Dimensional Finite Analytic Method for Simulation of Fluid Flow and Conjugate Heat Transfer," Ph.D. thesis, The University Iowa, August 1991.
- [6] R. Iwatsu, J.M. Hyun, and K. Kuwahara, "Analysis of Three-Dimensional Flow Calculations in a Driven Cavity," *Fluid Dynamics Research*, **Vol 6**, pp. 91-102, 1990.
- [7] Charles-Henri Bruneau and Claude Jouron, "An Efficient Scheme for Solving Steady Incompressible Navier-Stokes Equations," *Journal of Computational Physics*, **89**, pp. 389-413, 1990.